Subpicosecond-resolved emittance measurements of high-brightness electron beams with space charge effects at PITZ

Dissertation
zur Erlangung des Doktorgrades
an der Fakultät für Mathematik, Informatik und Naturwissenschaften
Fachbereich Physik
der Universität Hamburg

vorgelegt von
Raffael Niemczyk

Hamburg
2021

Gutachter der Dissertation:	Prof. Dr. Wolfgang Hillert Dr. Houjun Qian
Zusammensetzung der Prüfungskommission:	Prof. Dr. Wolfgang Hillert Dr. Houjun Qian Prof. Dr. Florian Grüner Prof. Dr. Gudrid Moortgat-Pick Dr. Winfried Decking
Vorsitzender der Prüfungskommission:	Prof. Dr. Florian Grüner
Datum der Disputation:	05.11.2021
Vorsitzender Fach-Promotionsausschuss Physik:	Prof. Dr. Wolfgang Hansen
Leiter des Fachbereichs Physik:	Prof. Dr. Günter H. W. Sigl
Dekan der Fakultät MIN:	Prof. Dr. Heinrich Graener

Abstract

In this thesis a scheme to measure the slice emittance of a high-brightness electron beam which undergoes space charge effects is developed and employed. For this, a transverse deflecting structure (TDS) is added to the single-slit scan technique, which is used at the Photo Injector Test Facility at DESY in Zeuthen (PITZ) to measure projected emittance. The beam is focused with quadrupole magnets behind the slit mask to ensure sufficient signal-to-noise ratio for a reliable slice phase space reconstruction, and hence, slice emittance calculation. The quadrupole magnets also allow time resolution below one picosecond. The beam optics is probed before the slice emittance measurements to ensure precise knowledge of the transport which is needed for the phase space reconstruction when using focusing magnets.
Numerical simulation of the slice emittance measurement was performed to estimate the systematic error arising from various factors, including space charge forces, drift distance, and focusing strength. Additionally intensity cuts were implemented to also consider errors arising from finite signal-to-noise ratio in experiment. For the parameters achieved at PITZ the net systematic error in the slice emittance reconstruction in the centre stays well below 10 %. The slice emittance measurement scheme is also analysed in methodology studies observing the measured emittance values varying the quadrupole focusing and TDS shearing strength proving reliable slice emittance measurements.
The slice emittance setup is used to characterise beam properties from electron bunches emitted with laser pulses of different shape. The main achievement is, that using a temporal and transverse flattop laser pulse shape reduces the slice emittance compared to a temporal Gaussian laser pulse with a transverse flattop distribution. The slice emittance is further improved when using a transversely-truncated Gaussian laser pulse with a temporal Gaussian profile, increasing the beam brightness additionally when employed e.g. in an free-electron laser (FEL) facility. The projected emittance is decomposed in measurement and simulation to identify slice emittance and mismatch emittance contributions to the projected emittance.

Kurzfassung

In dieser Dissertation wird ein Aufbau zur Messung der Strahlemittanz entlang eines Elektronenteilchenpakets (sog. Scheibenemittanz) entwickelt und eingesetzt. Hierzu wird eine seitlich ablenkende Kavität (engl. *transverse deflecting structure*, TDS) mit der Einzelschlitzabtastung, der Standardmethode zur Messung projizierter Emittanz am Photo Injektor Teststand bei DESY in Zeuthen (PITZ), kombiniert. Hinter der Schlitzmaske wird der Strahl mit Quadrupolmagneten fokusiert, um ein akzeptables Signal-Rausch-Verhältnis für eine zuverlässige Phasenraumrekonstruktion, und damit zur akkuraten Scheibenemittanzberechnung, sicherzustellen. Die Verwendung der Quadrupolmagnete erlaubt es, eine zeitliche Auflösung unterhalb einer Pikosekunde zu erreichen. Die Strahloptik wird vor jeder Scheibenemittanzmessung ermittelt, da die Optik mit hoher Präzision zur korrekten Phasenraumrekonstruktion gekannt werden muss.
Um die Auswirkung verschiedener systematischer Fehler auf die Scheibenemittanzmessung zu untersuchen wird die Strahldynamik, die der Aufbau zur Messung der Scheibenemittanz herbeiführt, numerisch simuliert. Zu den untersuchten Ursachen zählen unter anderem die Raumladungskräfte während des Strahltranports, die Distanz des Strahltransports, und die Fokusierstärke der Quadrupolmagnete. Zusätzlich werden auftretende Fehler durch das Signal-Rausch-Verhältnis, das im Experiment auftritt, mit Hilfe von Intensitätsschnitten in den Simulationsergebnissen analysiert. In der Mitte des Elektronenpakets bleiben systematische Fehler unterhalb von 10 % für die Parameter, die bei Messungen bei PITZ auftreten. Außerdem wird der Aufbau zur Messung der Scheibenemittanz experimentellen Methodikuntersuchungen unterzogen, indem die gemessene Emittanz beobachtet wird, während die Fokusierstärke und Ablenkstärke der abelnkenden Kavität variiert wird.
Der Messaufbau wird dazu verwendet, Elektronenstrahlen, die von Laserpulsen mit unterschiedlichen Pulsformen erzeugt werden, zu charakterisieren. Die Messungen zeigen, dass der Elektronenstrahl, der von einem Laserpuls mit zeitlich Rechteckprofil, im Vergleich zum Elektronenstrahlen, die von Laserpulsen mit zeitlich gaußförmigen Profil, eine reduzierte Scheibenemittanz hat. Die radiale Laserpulsform ist konstant innerhalb des Laserpulses, und endet abrupt beim Radius des Laserpulses. Die Scheibenemittanz reduziert sich weiter, wenn der Elektronenstrahl mit Hilfe eines Laserpulses emittiert wird, der in radialer Richtung ein Gauß'sches Intensitätsprofil hat, das an den Enden abgeschnitten ist. Die zeitliche Laserpulsform folgt hier dem Profil einer Normalverteilung. Wenn dieser Elektronenstrahl in einem Freie-Elektronenlaser verwendet wird, kann er die Brillanz der Strahlung steigern. Die simulierte und gemessene projizierte Emittanz wird in Scheibenemittanz und Optikversatzemittanz zergliedert, um die einzelnen Beiträge zur projizierten Emittanz zu identifizieren.

Contents

1 Introduction

Shortly after the first observation of synchrotron radiation in an electron synchrotron [1] the scientific use of this radiation started, leading to the development of dedicated synchrotron light sources for this purpose [2]. The high brilliance of the synchrotron light and its picoseconds-long pulse length made it a powerful tool in the fields of medicine, biology, physics, chemistry [3] and for industrial applications.
The pulse length of the synchrotron radiation can be further decreased when using special schemes, e.g. low-alpha operation [4], seeding of electron bunches with a short-pulse laser [5], use of harmonic rf resonators to create a high-frequent beating frequency for longitudinal compression [6], or the use of transverse deflecting structures in storage rings [7]. However, when researching the electron, atomic, or molecule dynamics, e.g. femtosecond-resolved crystallography [8], high repetition rate X-ray microscopy [9], ultrafast responses of matter [10], or observation of molecular dynamics and fastest chemical processes [11, 12], the use of hard X-ray radiation with shortest pulse length and highest brilliance is necessary [3]. The shortest and brightest X-ray pulses cannot be created in a synchrotron or storage ring, as the bunch particle can only radiate incoherently in the X-ray regime due to the long bunch length. Alternatively, coherent emission of radiation can be triggered with a seeding mechanism in a storage ring. However, storage rings lack seeding options for coherent radiation at hard X-ray wavelengths.
In a linear accelerator however, the bunch length can be much shorter than in a storage ring. In a photoinjector the bunch length can be as short as several tens to few hundred femtoseconds. But even with a longer bunch length from the injector the beam can be shortened in a linear accelerator by using magnetic chicanes, reaching bunch lengths down to few femtosecond. In an X-ray free-electron laser (FEL) the compressed electron bunches from a linear accelerator emit X-ray radiation coherently, leading to a high brilliance with short pulses, fulfilling the needed X-ray beam properties.
Free-electron lasers have been proposed in 1971 by John Madey [13] and experimentally proven at infrared wavelengths in 1977 [14]. The first FEL in the ultraviolet (UV) has been realised in 2000 at the TESLA Test Facility (TTF), now free-electron laser in Hamburg (FLASH) [15]. Ångström wavelengths were reached in 2009 at the Linac Coherent Light Source (LCLS) at SLAC [16]. In 2017, the European XFEL (Eu-XFEL) demonstrated first lasing [17]. It is currently the FEL with the world-wide highest peak brilliance [18, 19].
An FEL facility consists of three basic parts: an electron source, a linear accelerator with bunch compressors, and an undulator section. The electron source creates a bunched electron beam with high quality, a high bunch charge up to about 1 nC, pulse lengths of ~ 20 ps and below, peak currents of around 50 A and energies of a few MeV, while the linear accelerator increases the electron energy to GeV scales [19]. Finally, the electron bunches emit highly brilliant X-ray pulses in a periodic magnetic structure, the undulator. The power of the emitted radiation increases exponentially in the undulator section until it saturates at high radiation powers, see e.g. Ref. [19].
The beam quality is described by the emittance ϵ. The phase space emittance is given by the volume the bunch has in the six-dimensional phase space, given by the longitudinal and transverse positions and momenta. In the same way the trace space emittance is given by the volume the beam has in the transverse, four-dimensional trace space, spanned by the bunch particles positions and angles, i.e. transverse momenta over longitudinal momentum of the beam. As the angle of a particle depends on the longitudinal momentum the trace

space emittance shrinks during the acceleration process. This mechanism is referred to as adiabatic damping [20]. The phase space volume and the normalised emittance however do not decrease.
An important FEL parameter is the Pierce parameter ρ_{FEL}, which itself depends on the emittance via $\rho_{\mathrm{FEL}} \propto \sqrt[3]{1/\epsilon}$, see Ref. [21]. In linear FEL theory, the FEL bandwidth, when the radiation field is close to its saturation is given by the Pierce parameter [19]. The saturation power of the radiation field is described by the product of the Pierce parameter and the electron beam power, while the length needed to achieve saturation of the radiation power is inversely proportional to the Pierce parameter [19]. Therefore, to reduce the length of the undulator section needed to achieve saturation of the radiation field and to maximise the saturation power the Pierce parameter has to be maximised. Moreover, the minimally achievable radiation wavelength λ_{r} depends on the transverse emittance according to the emittance criterion $\epsilon \leq \lambda_{\mathrm{r}}/(4\pi)$, see Ref. [19]. Consequently, the emittance of an electron beam has to be minimised to improve the FEL performance. As the phase space emittance cannot decrease during the acceleration process, it forms an upper limit for the beam at the undulator entrance and has to be optimised right at the electron source. The electron guns used at FLASH and the Eu-XFEL are conditioned and optimised for high beam brightness at the Photoinjector Test Facility at DESY in Zeuthen (PITZ) [22]. For a correct characterisation of the electron source a robust procedure for transverse emittance measurements is crucial. Over the years a lot of effort was put into the experimental minimisation of the projected emittance and the analysis of the emittance measurement procedure at PITZ [23, 24, 25, 26, 27, 28, 29].
The lasing process in an X-ray FEL occurs only on small parts of the electron bunch. Therefore, not only the transverse emittance of the whole electron bunch is of interest, but also the transverse emittance of highly charged parts of the bunch which contribute to lasing, i.e. the slice emittance along the bunch [19]. As simulations show the optimum projected and slice emittance is achieved with different photoinjector settings, measurement and optimisation of both the projected and slice emittance is of interest [30].
The linear accelerators of FEL facilities measure the slice emittance by combining the quadrupole scan for the projected emittance measurement with a transversely deflecting cavity, introducing correlation of temporal position along the bunch and transverse position offset [31, 32, 33, 34, 35, 36, 37]. This is usually done at electron energies around 100 MeV. At PITZ, where only electron energies of ~20 MeV are reached, quadrupole magnet scans are more complicated due to the strong space charge effect of the beam [29]. Hence the transverse emittance is routinely measured by scanning a single-slit mask through the electron beam and observing the local beam divergence on a downstream screen [27]. The slice emittance can be measured by operating an accelerating cavity off-crest, introducing an energy-time correlation to the electron beam. When using either slit scan or quadrupole magnet scan the slice emittance is then measured in a dipole spectrometer [38]. This approach suffers from the time resolution limited to ~2 ps and by the necessity of the off-crest operation of the accelerating structure, which increases the energy spread of the bunch [38].
Installation of a transverse deflecting structure (TDS) at PITZ in 2015 enabled its use for time-resolved measurements, while the accelerating structure runs under nominal conditions [30, 38, 39, 40]. This work shows a scheme to measure the slice emittance of a space-charge-dominated, high-brightness electron beam with subpicosecond resolution using a single-slit scan and the TDS. Space-charge-dominated electron beams are also found at low-energy beam test facilities for next-generation continuous wave photoinjectors for FELs and energy-recovery linear accelerators. The slit mask has the disadvantage of a low signal strength, as most of the bunch charge is scattered by the slit mask. The deflection by the TDS leads to larger beam sizes and a further reduction of signal strength.

Both make the measurement prone to emittance underestimation. Application of focusing quadrupole fields improves both the signal strength and the time resolution, but complicates the phase space reconstruction compared to a reconstruction of a measurement without focusing optics. Probing the accelerator optics response with a corrector magnet allows beam-based determination of the beam transport matrix elements needed for the phase space reconstruction. This makes the emittance diagnostics robust despite the complicated beam transport.
This thesis is organised as follows. First, the basic concepts for transverse emittance measurements at linear accelerators are presented in Chapter 2. Additionally, the differences between projected and slice emittance are highlighted, before the special aspects of the beam dynamics in photoinjectors are described. In Chapter 3 the electron beamline PITZ for the experiment is introduced. The details of the photocathode lasers, the TDS at PITZ, and the slit and screen stations are explained, before showing the slice emittance diagnostics in Chapter 4. Here, an example of orbit response measurement as calibration for the slice emittance measurement is shown. The noise cut used in this thesis is explained before emittance underestimation due to finite signal-to-noise ratio is analysed. Chapter 5 shows studies on the resolution and the uncertainty of the slice emittance diagnostics. For this, simulations of the experiment are done to analyse systematic errors arising from the detection scheme. The simulations are carried out with ASTRA [41]. Additionally, slice emittance measurements with different beam optics in the diagnostics and TDS deflection strength are illustrated. Next to this, the calculation of the statistical uncertainty is explained. Chapter 6 shows measurements of the slice emittance at PITZ for different photocathode laser pulse shapes and corresponding start-to-end beam dynamics simulations. Chapter 7 gives a conclusion and discussion.

2 Theoretical Basis

The motion of particles in accelerators is most commonly described by linear beam dynamics. Although non-linear effects, i.e. beam dynamics in accelerating structures, space charge effects, wake fields or passage through sextupole or higher-order magnetic fields are not covered with this approach, it is still a powerful tool to describe the beam transport. This chapter gives an introduction into linear beam dynamics. Later rms beam properties are introduced, before the differences between slice and projected emittance are discussed. An insight into the beam dynamics of photoinjectors and the lasing process is given, before different emittance measurement methods are explained.

2.1 Linear Beam Dynamics

The acceleration and manipulation of charged particles is done by electric and magnetic fields, $\boldsymbol{E}$ and $\boldsymbol{B}$, respectively. The force a particle with charge q and velocity $\boldsymbol{v}$ experiences is given by the Lorentz force

$$\dot{\boldsymbol{p}} = \boldsymbol{F} = q\left(\boldsymbol{E} + \boldsymbol{v} \times \boldsymbol{B}\right), \tag{2.1.1}$$

where $\dot{\boldsymbol{p}}$ is the time derivative of the momentum [2]. Since the acceleration by the magnetic field force is only perpendicular to the particle velocity it cannot be used to increase the particle's energy. Therefore the electric fields are used to accelerate particles to high energies. Nevertheless, the magnetic fields are beneficial for deflection and focusing of charged particle beams.
The position and angle of a particle in the accelerator is given with respect to the position and angle of the so-called *reference particle*, travelling on the reference orbit. It is usually given by the design trajectory through the accelerator lattice. Figure 2.1 shows the definition of a particle position w.r.t. to the reference particle. A particle's position and state of motion are fully described by its three real space coordinates, as well as the transverse and longitudinal momenta p_x, p_y, and p_z, respectively. Nonetheless, it is common to use the particle's angles $x' = \mathrm{d}x/\,\mathrm{d}s$ and $y' = \mathrm{d}y/\,\mathrm{d}s$ in the transverse plane and the total momentum deviation $\Delta p/p$ in the longitudinal plane to describe the particle's motion.
If it can be assumed that every particle coordinate at a point s_1 in the particle accelerator contributes linearly to the coordinates at another point s_2, the beam transport can be written by means of the $\boldsymbol{R}$ matrix as

$$\begin{pmatrix} x \\ x' \\ y \\ y' \\ z \\ \Delta p/p \end{pmatrix}_{s_2} = \begin{pmatrix} R_{11} & R_{12} & R_{13} & R_{14} & R_{15} & R_{16} \\ R_{21} & R_{22} & R_{23} & R_{24} & R_{25} & R_{26} \\ R_{31} & R_{32} & R_{33} & R_{34} & R_{35} & R_{36} \\ R_{41} & R_{42} & R_{43} & R_{44} & R_{45} & R_{46} \\ R_{51} & R_{52} & R_{53} & R_{54} & R_{55} & R_{56} \\ R_{61} & R_{62} & R_{63} & R_{64} & R_{65} & R_{66} \end{pmatrix} \cdot \begin{pmatrix} x \\ x' \\ y \\ y' \\ z \\ \Delta p/p \end{pmatrix}_{s_1} . \tag{2.1.2}$$

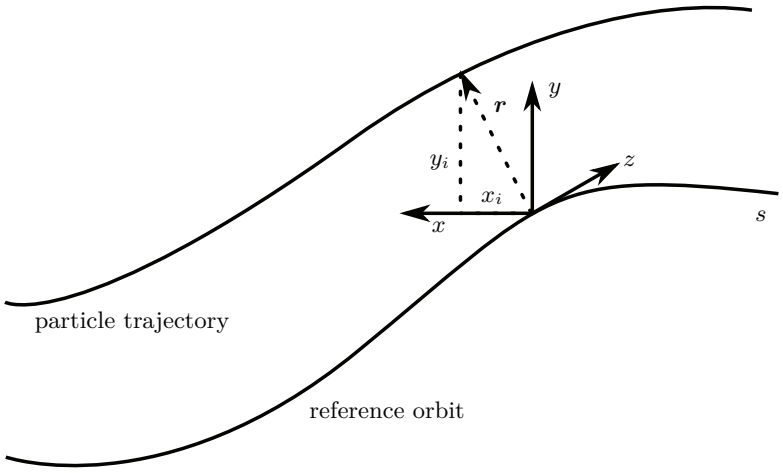

Figure 2.1: The co-propagating coordinate system moves along the reference orbit. All particle coordinates are given with respect to this system.

If all three planes are decoupled, Eq. 2.1.2 simplifies to

$$\begin{pmatrix} x \\ x' \\ y \\ y' \\ z \\ \Delta p/p \end{pmatrix}_{s_2} = \begin{pmatrix} R_{11} & R_{12} & 0 & 0 & 0 & 0 \\ R_{21} & R_{22} & 0 & 0 & 0 & 0 \\ 0 & 0 & R_{33} & R_{34} & 0 & 0 \\ 0 & 0 & R_{43} & R_{44} & 0 & 0 \\ 0 & 0 & 0 & 0 & R_{55} & R_{56} \\ 0 & 0 & 0 & 0 & R_{65} & R_{66} \end{pmatrix} \cdot \begin{pmatrix} x \\ x' \\ y \\ y' \\ z \\ \Delta p/p \end{pmatrix}_{s_1} . \tag{2.1.3}$$

To determine the matrix describing the beam transport through an arbitrary series of beamline elements, the corresponding beam transport matrices have to be multiplied. The accelerator optic consists mainly out of drift spaces, dipole magnets and quadrupole magnets. Since the drift space does not change the particle's angle, the sub-matrix coupling the transverse properties has the form

$$\boldsymbol{R} = \begin{pmatrix} 1 & l_\mathrm{d} \\ 0 & 1 \end{pmatrix}, \tag{2.1.4}$$

where l_d is the length of the drift space [2].
Quadrupole magnets are used to focus the beam. Their focusing strength onto a charged particle beam is given by k, while their effective length is depicted by l_q. The transport matrix of a quadrupole magnet is given by

$$\boldsymbol{R} = \begin{pmatrix} \cos\Omega & \frac{1}{\sqrt{|k|}}\sin\Omega \\ -\sqrt{|k|}\sin\Omega & \cos\Omega \end{pmatrix}, \tag{2.1.5}$$

where $\Omega = \sqrt{|k|}l_\mathrm{q}$ and k is the focusing gradient [2]. When the quadrupole magnet is approximated with a thin lens

$$\boldsymbol{R} = \begin{pmatrix} 1 & 0 \\ -kl_\mathrm{q} & 1 \end{pmatrix} \tag{2.1.6}$$

is used to describe the beam transport.
However, the quadrupole fields are only focusing in one transverse plane, while acting defocusing in the other plane. Therefore, the transport matrix in the defocusing plane has the form

$$\boldsymbol{R} = \begin{pmatrix} \cosh\Omega & \frac{1}{\sqrt{|k|}}\sinh\Omega \\ \sqrt{|k|}\sinh\Omega & \cosh\Omega \end{pmatrix}. \tag{2.1.7}$$

In order to have a net focusing in both planes, several quadrupole magnets of alternating gradients have to be combined.

2.2 Twiss Parameters and Transverse Emittance

In the section before the beam transport matrices for different lattice elements were introduced. The general equations of motion of a particle in an accelerator are given by the differential equations [2]

$$x''(s) + \left(\frac{1}{R^2(s)} - k(s)\right) x(s) = \frac{1}{R(s)} \frac{\Delta p}{p} \text{ and} \tag{2.2.1}$$

$$y''(s) + k(s)y(s) = 0, \tag{2.2.2}$$

where $x''(s)$ is the second derivative of the transverse position w.r.t. the longitudinal coordinate. The trajectory radius caused by the deflection in a dipole field is denoted as $R(s)$. It is assumed that dipole fields act only in the horizontal plane. The focusing terms differ in sign in both planes, as quadrupole fields, which are typically used for beam focusing, act focusing in one plane and simultaneously defocusing in the other plane. The solution of this equation for the particle i in one plane is given by

$$x_i(s) = \sqrt{\epsilon}\sqrt{\beta(s)} \cos\left(\mu(s) + \Psi_i\right), \tag{2.2.3}$$

when no dispersion is present. Here ϵ is an integration coefficient, $\beta(s)$ the beta function or amplitude function, $\mu(s)$ the phase advance and Ψ_i the starting phase [42]. The beta function $\beta(s)$ gives the lattice-depended contribution to the beam size along the accelerator. While the beta function and phase advance are the same for all particles and only depend on the longitudinal position within the accelerator lattice, Ψ_i is arbitrary for each individual particle [2, 42]. The cosine term reveals that the particles undergo an oscillating motion in the transverse planes.
The phase advance from a starting point s_1 to another point s is calculated via

$$\mu(s) = \int_{s_1}^{s} \frac{\mathrm{d}s'}{\beta(s')}, \tag{2.2.4}$$

i.e. a smaller beta function leads to a faster oscillation of the particles [2].
Now the general transport matrix between a point s_1 and s_2

$$\boldsymbol{R} = \begin{pmatrix} \sqrt{\frac{\beta_2}{\beta_1}} \left(\cos\mu + \alpha_1 \sin\mu\right) & \sqrt{\beta_1\beta_2} \sin\mu \\ \frac{(\alpha_1 - \alpha_2)\cos\mu - (1+\alpha_1\alpha_2)\sin\mu}{\sqrt{\beta_1\beta_2}} & \sqrt{\frac{\beta_1}{\beta_2}} \left(\cos\mu - \alpha_2 \sin\mu\right) \end{pmatrix} \tag{2.2.5}$$

can be formulated, with the phase advance μ between the two points s_1 and s_2 and the alpha function

$$\alpha(s) = -\frac{\beta'(s)}{2}. \tag{2.2.6}$$

When Eq. 2.2.3 is inserted into Eq. 2.2.1 and the definitions

$$\gamma(s) = \frac{1 + \alpha^2(s)}{\beta(s)}. \tag{2.2.7}$$

is introduced, the equation

$$\epsilon = \gamma(s)x^2 + 2\alpha(s)xx' + \beta(s)x'^2 \tag{2.2.8}$$

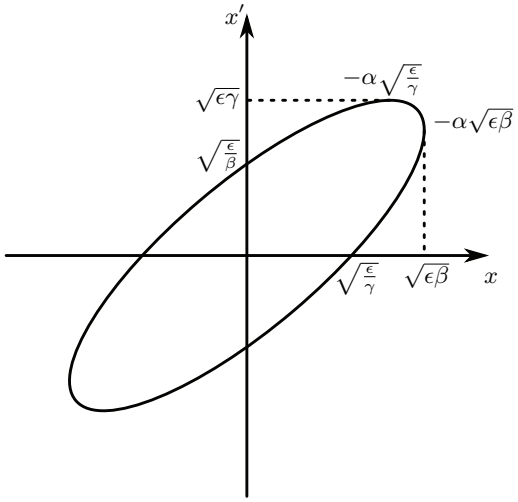

Figure 2.2: The particle distribution usually forms an ellipse in the transverse trace space. The area of the rms ellipse is given by $\pi\epsilon$.

is obtained, see Ref. [2]. The factors $\alpha(s)$, $\beta(s)$, and $\gamma(s)$ are known as Twiss parameters. Equation 2.2.8 describes an ellipse in the trace space. Usually an elliptical shape is a good approximation for the particle distribution in the x-x'-plane, i.e. the trace space, see Fig. 2.2. For an ensemble of particles

$$\epsilon = \gamma(s)\langle x^2\rangle + 2\alpha(s)\langle xx'\rangle + \beta(s)\langle x'^2\rangle \tag{2.2.9}$$

applies.
While the assumption of a 2d-Gaussian particle distribution, which has an elliptical equipotential line, is true for circular machines, it is in general not the case for linear accelerators, in particular not for photoinjectors. Nevertheless, all particle distributions in the phase space can be represented by an equivalent ellipse [43].
The volume the particle density distribution occupies in the phase space is given by $\pi\epsilon$, where ϵ is the transverse, geometric rms emittance [2]. It is calculated via

$$\epsilon_x = \sqrt{\langle x^2\rangle\langle x'^2\rangle - \langle xx'\rangle^2}, \tag{2.2.10}$$

from the second-order beam momenta $\langle x^2\rangle$, $\langle x'^2\rangle$ and $\langle xx'\rangle$ of the particle distribution. Here the statistical (rms) definitions are used. The Twiss parameters are calculated from the beam moments via

$$\alpha_x = -\frac{\langle xx'\rangle}{\epsilon_x}, \tag{2.2.11}$$

$$\beta_x = \frac{\langle x^2\rangle}{\epsilon_x} \text{ and} \tag{2.2.12}$$

$$\gamma_x = \frac{\langle x'^2\rangle}{\epsilon_x}. \tag{2.2.13}$$

The geometric emittance reduces during an acceleration process, since the angular rms spread $\langle x'^2\rangle$ depends on the mean momentum. In order to be able to compare the transverse emittance at different energies the normalised emittance

$$\epsilon_{\mathrm{n},x} = \beta\gamma\epsilon_x \tag{2.2.14}$$

is introduced. Here γ is the Lorentz factor and β the relative particle velocity, i.e. $\beta = v/c$. For the normalisation factor $\beta\gamma = \sqrt{\gamma^2 - 1}$ applies [25].

2.3 Space Charge Forces

Besides external electromagnetic forces, applied by magnets and rf cavities, the internal space charge effect gives another contribution to the particle beam dynamics. No general parametrisation of space charge effect can be derived as the space charge forces depend on the charge distribution. However, for a few special cases an example can be given. Here a cylindrically-symmetric charge distribution with a Gaussian shape in all dimensions is assumed. The total charge content is Q, while the distribution has the radial size σ_r and the length σ_z. The radial electric space charge field is derived in Ref. [44] and given by

$$E_r(r,z) = \frac{1}{(2\pi)^{(3/2)}\epsilon_0}\frac{Q}{\sigma_z}\mathrm{e}^{-\frac{z^2}{2\sigma_z^2}}\left(\frac{1-\mathrm{e}^{-\frac{r^2}{2\sigma_r^2}}}{r}\right), \tag{2.3.1}$$

where ϵ_0 describes the vacuum permittivity. When the bunch moves with the velocity $v = \beta c$ along z an azimuthal magnetic field $B_\Phi = (\beta/c)E_r$ is observed in the laboratory frame [44]. The total space charge force applying onto a particle with charge q is then given by

$$F_r(r,z) = q(E_r - vB_\phi). \tag{2.3.2}$$

This corresponds to a focusing effect of the magnetic field, which acts against the defocusing electric field. With the expression $(1-\beta^2)^{-1} = \gamma^2$ the radial force becomes

$$F_r(r,z) = q(1-\beta^2)E_r(r,z) = \frac{q}{(2\pi)^{(3/2)}\gamma^2\epsilon_0}\frac{Q}{\sigma_z}\mathrm{e}^{-\frac{z^2}{2\sigma_z^2}}\left(\frac{1-\mathrm{e}^{-\frac{r^2}{2\sigma_r^2}}}{r}\right). \tag{2.3.3}$$

Equation 2.3.3 shows that the radially defocusing space charge force F_r of such a charge distribution is non-linear in r, while also changing along the longitudinal position z. Non-linearities in space charge force yield to an increase in rms (slice) emittance, while variations of radial space charge forces along the longitudinal coordinate lead to development of a fan structure in the transverse phase space.

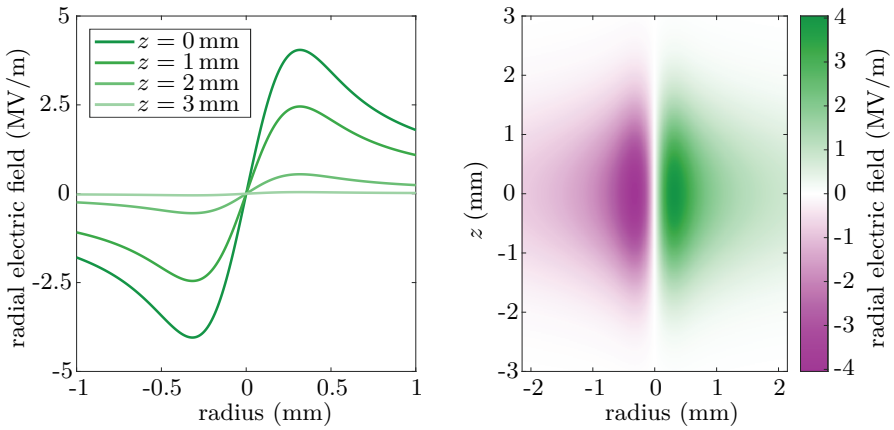

Figure 2.3: Radial electric space charge field of a bunch with 3d-Gaussian charge distribution. The bunch charge is $Q = 250\,\mathrm{pC}$, and the beam size is $\sigma_r = 0.2\,\mathrm{mm}$ and $\sigma_z = 1\,\mathrm{mm}$. Within $\pm\sigma_r$ the radial space charge forces are fairly linear, while showing strong non-linearities beyond this range. The strength of the radial electric field is changing along different z positions. Adapted from [45].

Besides this, Eq. 2.3.3 describes that the amplitude of the space charge forces is suppressed for increasing beam energy with $\propto \gamma^{-2}$. Therefore, space charge effects degrade the beam stronger at lower energies and are of less concern at high energies. The space charge forces for a uniformly filled cylindrical charge distribution are described in Ref. [46].

2.4 Beam Envelope Equation

The evolution of the transverse beam size of a particle beam is described by the beam envelope equation. When the acceleration, i.e. $\mathrm{d}\gamma/\,\mathrm{d}s = 0$, and focusing of the particle beam is neglected, the second-order derivative of the beam envelope $\mathrm{d}\sigma_{x,y}^2/\mathrm{d}^2 s = \sigma''_{x,y}$ is described by

$$\sigma''_x = \frac{I}{I_\mathrm{A}(\sigma_x+\sigma_y)\gamma^3} + \frac{\epsilon_{\mathrm{n},x}^2}{\sigma_x^3\gamma^2} \text{ and} \tag{2.4.1}$$

$$\sigma''_y = \frac{I}{I_\mathrm{A}(\sigma_x+\sigma_y)\gamma^3} + \frac{\epsilon_{\mathrm{n},y}^2}{\sigma_y^3\gamma^2}, \tag{2.4.2}$$

when the beams are asymmetric, i.e. have different beam size in both transverse planes, see Ref. [47]. The transverse normalised rms emittance is given by ϵ_n, the peak current by I, while $I_\mathrm{A} = 4\pi\epsilon_0 m_e c^3/e \approx 17\,\mathrm{kA}$ describes the Alfvén current, where e is the elementary charge and m_e the electron mass [19].
The beam envelope equation is given by a sum of two fractions, which express the influence of space charge forces onto the change in beam envelope, as well as the influence arising from the angular spread, given by the finite emittance. The beams can henceforth be divided into space-charge-dominated beams and emittance-dominated beams depending on which contribution is significant to the transverse beam dynamics.
Particle beams at lower energy are rather dominated by space charge effects, as the space charge term reduces with $\propto \gamma^{-3}$, while the emittance term scales down with γ^{-2}. Additionally the beam size affects the strength of space charge effects: A larger horizontal and vertical beam size lead to a lower charge density, so that the amplitude of space charge forces is smaller. This allows to turn a space-charge-dominated beam into an emittance-dominated beam: reduction of e.g. the horizontal beam size σ_x while keeping the vertical beam size the same increases the charge density, which leads to a larger space charge term. However, the reduction in horizontal beam size leads also to an increase of the emittance term, which in total can lead to a shift to emittance domination in the horizontal plane.

2.5 Transverse Emittance Decomposition

The second-order beam moments of a particle beam can be different along the longitudinal position within a single particle bunch, leading to a changing emittance along the bunch. The transverse emittance of the whole particle bunch is denoted as projected emittance, while the transverse emittance of a short, longitudinal disc of the bunch is referred to as slice emittance.
The projected phase space ellipse is the overlap of all slice phase space ellipses, weighted with the charge in each slice. Therefore, if all slice phase space ellipses are aligned, i.e. they have identical mean position $\mu_x(z)$, mean angle $\mu_{x'}(z)$, as well as the same ellipse orientation, the projected emittance is the charge-weighted average of the slice emittance along all slices. However, different mean positions or angles among different slice ellipses or different slice ellipse orientations lead to a bigger projected emittance than the average slice emittance. Thus, knowledge of the slice emittance is of interest to describe beam

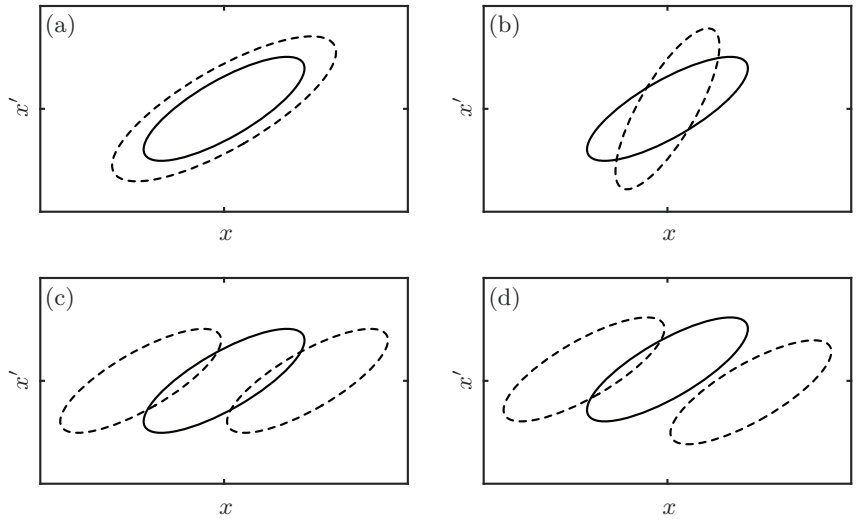

Figure 2.4: Different orientations of the slice phase space ellipses. Image (a) shows a phase space in which the ellipse of two different slices (e.g. head and centre slice) have different size, i.e. slice emittance. In (b), both slices have the same slice emittance but different orientations, i.e. different α function. Figure (c) depicts three slices, which have the same slice emittance and orientation, but have a linear shift w.r.t. each other, contributing to a linear misalignment emittance. This can be in x as well as in x'. The ellipses can also be shifted non-linearly w.r.t. each other, yielding non-linear misalignment emittance, as shown in (d).

dynamics acting only on a temporal slice of the particle bunch.
Reference [48] shows that the projected rms emittance ϵ_x can be decomposed as

$$\epsilon_x^2 = \epsilon_\perp^2 + \epsilon_\mathrm{R}^2 + \epsilon_\mathrm{int}^2 + \epsilon_\parallel^2, \tag{2.5.1}$$

where $\epsilon_\perp$, ϵ_R, ϵ_int and $\epsilon_\parallel$ are contributions based on properties of the slice phase space. The first contribution is the mean slice emittance $\epsilon_\perp$, which is calculated via

$$\epsilon_\perp^2 = \mathrm{E}\big[\epsilon_x(z)\big]^2, \tag{2.5.2}$$

with the slice emittance $\epsilon_x(z)$ and the charge-weighted average of a property $\Phi(z)$ among all slices

$$\mathrm{E}[\Phi] = \int \Phi(z)\lambda(z)\,\mathrm{d}z \tag{2.5.3}$$

with

$$\int \lambda(z)\,\mathrm{d}z = 1. \tag{2.5.4}$$

Here $\lambda(z)$ describes the longitudinal charge density profile, i.e. the bunch profile. This contribution gives the lower limit to the projected emittance. This case is depicted in Fig. 2.4. Subfigure (a) shows two overlapping ellipses with the same mean position in trace space but different areas, i.e. different slice emittance.
The term ϵ_R is denoted as mismatch emittance, since it contains the contribution arising from different orientations of the slice phase space ellipses w.r.t. each other, i.e.

$$\epsilon_\mathrm{R}^2 = \mathrm{Var}\big[\epsilon_x(z)\big] - \mathrm{Cov}\Big[\sigma_x^2(z), \sigma_{x'}^2(z)\Big] + \mathrm{Var}\Big[\langle \Delta x \Delta x' \rangle_z\Big], \tag{2.5.5}$$

with the covariance

$$\mathrm{Cov}[\Phi_\mathrm{a}, \Phi_\mathrm{b}] = \mathrm{E}\Big[\big(\Phi_\mathrm{a} - \mathrm{E}[\Phi_\mathrm{a}]\big)\,\big(\Phi_\mathrm{b} - \mathrm{E}[\Phi_\mathrm{b}]\big)\Big] \tag{2.5.6}$$

and the variance $\mathrm{Var}[\Phi] = \mathrm{Cov}[\Phi, \Phi]$. Figure 2.4 (b) shows an example of differently orientated ellipses, leading to a contributing mismatch emittance ϵ_R. The variation in space charge forces along the longitudinal bunch coordinate can lead to the mismatch in slice phase space ellipses.
The remaining two terms describe the linear misalignment emittance

$$\epsilon_\mathrm{int}^2 = \mathrm{E}\Big[\sigma_x^2(z)\Big]\,\mathrm{Var}\big[\mu_{x'}(z)\big] + \mathrm{E}\Big[\sigma_{x'}^2(z)\Big]\,\mathrm{Var}\big[\mu_x(z)\big] - 2\mathrm{E}\Big[\langle \Delta x \Delta x' \rangle_z\Big]\,\mathrm{Cov}\big[\mu_x(z), \mu_{x'}(z)\big] \tag{2.5.7}$$

and the non-linear misalignment emittance

$$\epsilon_\parallel^2 = \mathrm{Var}\big[\mu_x(z)\big]\,\mathrm{Var}\big[\mu_{x'}(z)\big] - \mathrm{Cov}\big[\mu_x(z), \mu_{x'}(z)\big]^2\,, \tag{2.5.8}$$

where $\sigma_x^2(z)$, $\sigma_{x'}^2(z)$ and $\langle \Delta x \Delta x' \rangle_z$ describe the second-order beam moments of each slice. These two equations contribute to the projected emittance, if the mean position and angle of each phase space ellipse differ along the slices. An example of two ellipses with linear spatial offsets is given in Fig. 2.4 (c), while (d) depicts non-linear offsets between the slice centroids along z. A change in average position or angle among different slices can be caused by either an off-centre trajectory through an accelerating cavity or by an off-centre path through a quadrupole magnet of a beam with different particle energies at different slices, e.g. a time-energy correlation. These can be reduced by an optimisation of the beam transport. More details on how the slice phase space ellipses contribute to the projected emittance are found in [48] and in references therein.

2.6 Mismatch Parameter

The Twiss parameter of a particle beam in an accelerator can differ from the Twiss parameter expected from the accelerator design optics. This variation is characterised with the dimensionless mismatch parameter M. Since no design optics are used for slice emittance measurements at PITZ [22] a comparison with design values is not possible. Instead, the slice Twiss parameter are compared with the projected Twiss parameter. It is derived via the equation

$$M = \frac{1}{2}\left[\beta_\mathrm{s}\gamma_\mathrm{p} - 2\alpha_\mathrm{s}\alpha_\mathrm{p} + \gamma_\mathrm{s}\beta_\mathrm{p}\right], \tag{2.6.1}$$

where α, β and γ stand for the Twiss parameter, while the indices s and p indicate slice and projected properties. The mismatch parameter is exactly 1.0 when the slice Twiss parameter equal the projected ones. Otherwise, the mismatch parameter is larger than one. In order to reduce the projected emittance all slice phase spaces have to have the same orientation, i.e. ideally a mismatch parameter of 1 along the bunch.

2.7 Beam Dynamics in Photoinjectors

Split photoinjectors with a booster linac, located after a drift behind the gun cavity, are used to create ps-long electron beams with a low transverse emittance and high bunch charge. Here, electrons are created at the photocathode after a laser shined light onto it. Right after emission the electron energies are on the eV level. At this point, the transverse beam emittance is given by the thermal emittance

$$\epsilon_\mathrm{thermal} = \sigma_x \frac{\sqrt{\langle p_x^2 \rangle}}{m_0 c}. \tag{2.7.1}$$

The horizontal beam size, which corresponds to the size of the laser beam, is denoted as σ_x, the transverse rms momentum spread is given by $\sqrt{\langle p_x^2 \rangle}$, the electrons mass is given by

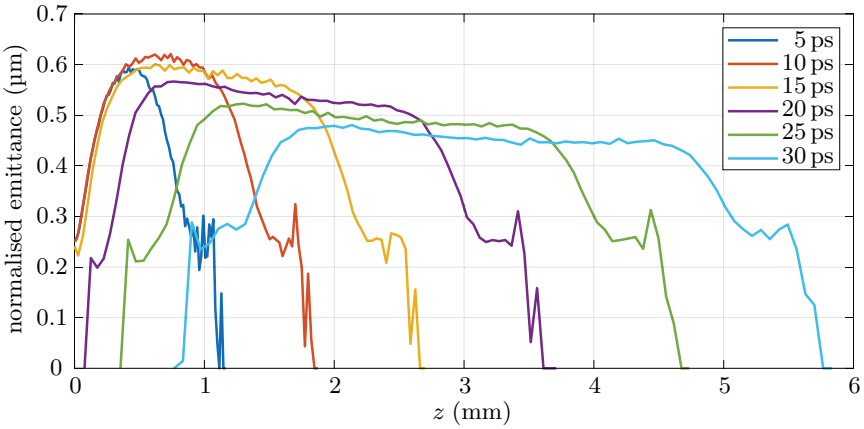

Figure 2.5: Formation of the slice emittance of an electron bunch during its emission. This simulation shows the emission of a cylindrical, 500 pC beam with a radially uniform distribution with $\sigma_r = 0.3$ mm, a longitudinal flattop length of 22 ps and a thermal emittance of 0.25 µm. Adapted from [49].

m_0 while c is the speed of light.
The electrons experience repulsive space charge forces due to the high extracted charge at pC to nC level. The non-linearities of the space charge forces lead to degradation of the beam quality, i.e. the emittance.
To suppress this, the photocathode is located inside an accelerating cavity, the electron gun, which allows rapid acceleration of electrons to relativistic energies of a few MeV. The reduction of defocusing space charge forces is achieved at higher beam energies according to Eq. 2.3.3, which motivates the development of high-gradient electron guns. The evolution of the slice emittance during the emission of the electrons is depicted in Fig. 2.5. Despite the rapid acceleration to relativistic energies in the gun, the space charge forces still defocus the electron beam, as the bunch length is very short right after emission. As the charge, thus the space charge forces, are higher in the centre of the bunch than in the head and tail slices, the centre slices experience stronger defocusing, leading to a misalignment of the slice phase space ellipse, which increases the projected emittance according to Eq. 2.5.2 and Eq. 2.5.5. However, the emittance growth is compensated by employing a focusing element around or close after the gun. The beam dynamics are sketched in Fig. 2.6. In the first frame the phase space right after emission is shown. No correlation between angle and position exists, the width of the ellipse is given by the laser size, while the area is defined by the thermal emittance, see Eq. 2.7.1. In Fig. 2.6 (b) the phase space after the emission is presented. The orange-coloured slices experienced a stronger defocusing force, while the red slices were defocused less strongly. A focusing magnet flips the fan-like phase space ellipses, so that the beam is converging, see (c). As the emittance growth happens on both transverse planes, an element which acts focusing on both transverse planes is used, i.e. a solenoid magnet. In the following drift the slice phase space ellipses start to overlap again until they reach the focus point, as shown in Fig. 2.6 (d).
The low projected emittance, which is obtained at the point where the slice ellipses are realigned, is preserved by further accelerating the electron beam. This means, that the lowest projected emittance is achieved when the electron beam has its focus in or close to the entrance of the first accelerating structure after the gun, which motivates the use of the split photoinjectors as sources for high-brightness electron beams [50].
However, despite its advantages, the emittance growth compensation scheme only allows to compensate emittance growth based on linear defocusing forces, while all non-linear (space

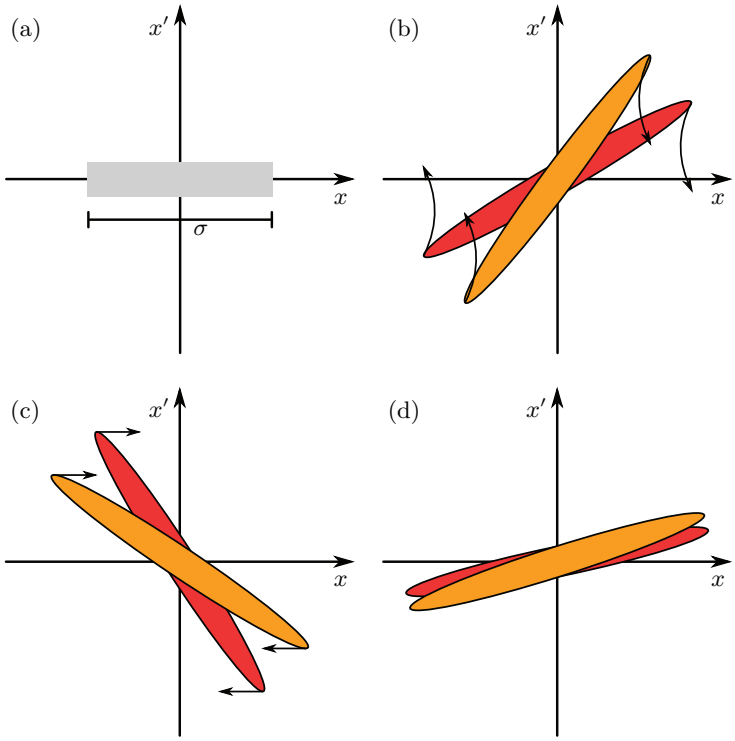

Figure 2.6: Phase space during emittance growth compensation. The phase space from the cathode (a) grows due to the space charge forces inside the bunch (b). The bunch centre slice (orange) experiences a stronger defocusing force than the head and tail (red). A solenoid magnet is used to focus the beam again (c). In the following drift the slices start to overlap again (d), minimising the projected emittance.

charge) forces lead to an emittance growth which cannot be compensated. This encourages the minimisation of non-linear space charge forces, i.e. shaping the photocathode laser pulse shape to a profile, yielding small non-linear space charge forces.

2.8 Free-Electron Laser

The radiation from free-electron lasers (FELs) is an important research instrument in several fields, including medicine, chemistry and biology [3, 5]. Electrons are emitting this radiation in undulators. The base is given by spontaneous undulator radiation. The resonant wavelength λ_r of the radiation emitted in an undulator is given by

$$\lambda_\mathrm{r} = \frac{\lambda_\mathrm{u}}{2\gamma^2}\left(1 + \frac{K^2}{2} + \gamma^2\varphi^2\right), \tag{2.8.1}$$

where λ_u is the period length of the undulator magnet, γ the relativistic Lorentz factor, φ the observation angle w.r.t. the beam axis, and

$$K = \frac{e}{2\pi mc} B_\mathrm{u}\lambda_\mathrm{u} \tag{2.8.2}$$

the undulator strength parameter [21], with the amplitude of the magnetic flux density B_u. The elementary charge is described by e, while the electron mass is given by m.
The emitted radiation co-propagates with the electron beam and couples to the electron due to their transverse motion inside the undulator. This creates an energy modulation

of the electron beam with the same periodicity as the emitted undulator radiation. The longitudinal dispersion R_{56} inside the magnet transforms the energy modulation into a density modulation. This density modulation is referred to as micro bunching. The micro bunching gives rise to coherent emission of radiation, which means that the power of the emitted radiation field is proportional to the number of coherently emitting electrons squared, N^2, while the power of incoherently emitting electrons is only linearly growing with the number of electrons.
The increased coherence of the emission leads to a higher radiation field strength than given in the spontaneous undulator radiation. The process repeats itself with the radiation with higher amplitude, which leads to an exponential growth of radiation power along the undulator of a single-pass FEL, until it saturates. This process in called self-amplified spontaneous emission (SASE) [21].
Many properties of the radiation and the FEL depend on the Pierce parameter ρ_{FEL} [21]. It is given by

$$\rho_{\mathrm{FEL}} = \left(\frac{1}{16} \frac{I}{I_{\mathrm{A}}} \frac{K^2 [\mathrm{JJ}]^2}{\gamma^3 \sigma_x^2 k_{\mathrm{u}}^2} \right)^{1/3}. \tag{2.8.3}$$

The peak current is given by I, the undulator wave number by $k_{\mathrm{u}} = 2\pi/\lambda_{\mathrm{u}}$, and the Bessel function factor $[\mathrm{JJ}] = \left[J_0(\xi) - J_1(\xi) \right]$, which in turn depends on whether the undulator is planar or helical [21].
As the beam size depends onto the transverse emittance via $\sigma_x^2 = \beta_x \epsilon_x$, the Pierce parameter depends on the transverse emittance via the relation $\rho_{\mathrm{FEL}} \propto \epsilon^{-1/3}$.
In one-dimensional FEL theory the gain length L_{g} depends onto the Pierce parameter via

$$L_{\mathrm{g}} = \frac{1}{4\pi\sqrt{3}} \frac{\lambda_{\mathrm{u}}}{\rho_{\mathrm{FEL}}}. \tag{2.8.4}$$

The power of the radiation field at saturation depends on the beam power P_{beam} via

$$P_{\mathrm{sat}} \approx \rho_{\mathrm{FEL}} P_{\mathrm{beam}}, \tag{2.8.5}$$

while the relative FEL radiation bandwidth at saturation is

$$\frac{\Delta\omega}{\omega} \approx \rho_{\mathrm{FEL}}. \tag{2.8.6}$$

Equation 2.8.4, 2.8.5, and 2.8.6 point out, that a larger Pierce parameter ρ_{FEL} leads to a better FEL performance. A higher Pierce parameter can be achieved by increasing the peak current I or reducing the beam size σ. As the beam size depends on the emittance, a low emittance is beneficial for a high-performance FEL.

2.9 Emittance Measurement Schemes

The arrangements to measure the transverse projected emittance in a linear accelerator can be divided into four broad schemes. They can be divided into two classes: quadrupole magnet scan and multiscreen scan, which are employed when the beam is emittance dominated, and pepper pot and slit scans, which turn a space-charge-dominated beam into an emittance-dominated beam by cutting out small parts of the beam. They all have in common that they require beam size measurements. In combination with an rf deflector cavity these setups allow measurement of the slice emittance, but only in the plane perpendicular to the deflection.

2.9.1 Pepper Pot

The so-called *pepper pot* scheme employs a mask with small holes, followed by an observation screen. The setup is sketched in Fig. 2.7. The resemblance with a pepper pot gives it its name. While some particles can pass through the holes, the majority of particles is strongly scattered by the slit mask. Hence only the particles at the hole positions contribute to the beam image downstream.
To reconstruct the transverse phase space at the pepper pot, the position, distribution, and intensity of the cut-out sub-beams, the so-called *beamlets*, are measured. The size $x_{2,i,\mathrm{rms}}$ of the beamlet i after a distance l is given by

$$x_{2,i,\mathrm{rms}} = \sqrt{\sigma_i'^2 \cdot l^2 + \sigma_i^2}, \tag{2.9.1}$$

where σ_i' denotes the angular rms spread of the particles passing the ith hole. The beamlet size starts from the rms size of the holes σ_i. For circular holes with radii r, $\sigma_i = r/2$ can be assumed, as the beam is spatially uniform on the scale of the hole size.
If the initial beam size contribution can be neglected, i.e. the drift l and the angular spread are sufficiently high while the holes are small, the angular spread of the beam at the position i is calculated via

$$\sigma_i' = \frac{x_{2,i,\mathrm{rms}}}{l}. \tag{2.9.2}$$

Alternatively, if

$$\sigma_i' \cdot l \gg \sigma_i \tag{2.9.3}$$

does not hold, the beam size contribution of the holes can be extracted via deconvolution. Since the angular distribution x' at different hole positions x is known the transverse phase space can be reconstructed and the emittance is calculated.
The advantage of this method is its single-shot capability, and is therefore less demanding on the stability of the accelerator operation. Also, this method allows not only the simultaneous measurement of the horizontal and vertical emittance, but also the calculation of the correlation terms between horizontal and vertical plane, i.e. the calculation of the four-dimensional emittance. Drawbacks are the reduced signal strength due to the use of a hole mask which causes a very small fraction of undisturbed transmitted electrons. This makes the setup prone to underestimation of the beamlet size, which translates into an emittance underestimation.
Furthermore, the beamlets are not allowed to overlap for a correct calculation of the beam moments. Hence the beam must be divergent at the slit mask, i.e. $\langle xx' \rangle \geq 0$, while the uncorrelated divergence $\langle x^2 \rangle$ must be sufficiently small. Moreover, for a correct calculation of the beam momenta the number of holes covering the beam has to be sufficient. Since beams with low emittance have a small beam size and small angular spread, the holes must be close to one another, which is contradicting the argument of sufficient hole spacing to prevent the beamlets from overlapping. The production of masks with small holes for beams with smallest emittance also imposes difficulties in manufacturing.

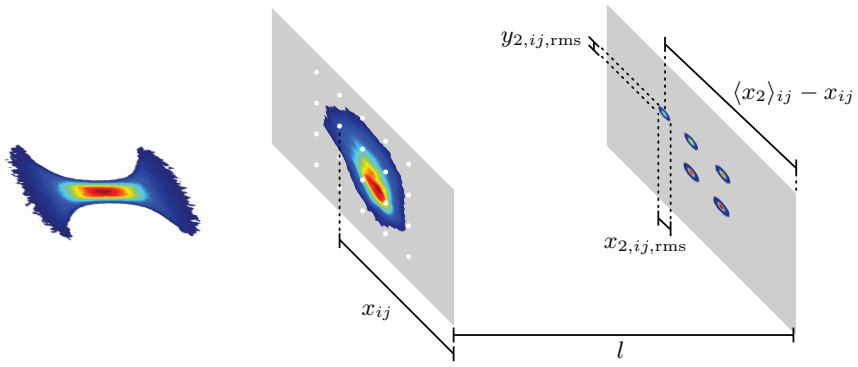

Figure 2.7: Scheme of the pepper pot emittance measurement. The pepper-pot-like mask creates beamlets in the horizontal and vertical plane. Their beam size in x and y, as well as their position with respect to each other are measured to reconstruct the 4D phase space. Advantage is the single-shot capability.

2.9.2 Slit Scan

The single-slit scan technique is a variation of the pepper pot scheme. They differ in the fact, that instead of having several holes in the slit mask, it only has a single slit. In order to measure the emittance, the slit mask is moved through the beam, while the beamlet images are recorded for different positions of the slit mask, see Fig. 2.8. For the phase space reconstruction the angular spread is calculated analogue to Eq. 2.9.2, whereas the initial beamlet size in case of a rectangular slit profile is given by $\sigma = \mathrm{width}/\sqrt{12}$.
As the slit positions are scanned this method requires several shots, namely the number of different slit positions which are being probed. Therefore a certain machine pointing stability is required. Also, the scan of a single slit mask just yields the phase space in one transverse plane. A scan of the other plane with a second slit mask is needed to determine the transverse emittance in both planes and reconstruct the four-dimensional phase space [51].

Since the slit mask has only one opening, several constrains of the pepper pot scheme do not apply: the full beam can be scanned by the mask opening, whereas at the pepper pot scheme the beam is only probed in steps of the hole separation, unless the beam is moved w.r.t. the pepper pot mask with e.g. corrector magnets. The slit scan scheme is also more flexible with regard to the beam divergence: as there is only one beamlet at each time they cannot overlap on the observation screen. However, this method is still prone to emittance

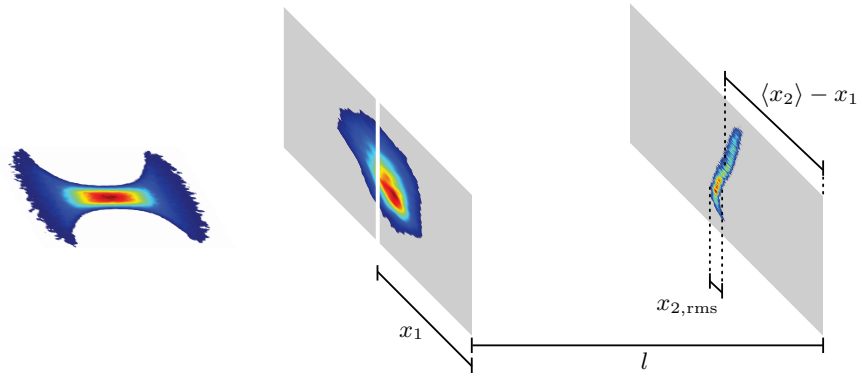

Figure 2.8: Scheme of the slit scan emittance measurement. A slit is moved through the beam, cutting out beamlets. Their intensity, size $x_{2,\mathrm{rms}}$ and offset with respect to the slit position $\langle x_2 \rangle - x_1$ is measured for each slit position x_1.

underestimation due to the low charge density on the observation screen, but less than in case of the pepper pot.
Next to the pepper pot and slit scan scheme also the multi-slit scheme exist, which is a mix of both. It allows measurement of the emittance in one plane in a single shot, while increasing the signal strength compared to the pepper pot scheme. Drawback of this scheme is that the slit spacing cannot be chosen freely.

2.9.3 Quadrupole Scan

An emittance measurement scheme without charge reduction by masks is the so-called *quadrupole scan*. In the most simple case the setup consists of a quadrupole magnet with strength k and effective length l_q, followed by an observation screen after a drift space of length l_d. If the thin-lens model of the quadrupole is assumed the transfer matrix for the setup is given by

$$\begin{pmatrix} x \\ x' \end{pmatrix}_{s_2} = \begin{pmatrix} 1 & l_d \\ 0 & 1 \end{pmatrix} \cdot \begin{pmatrix} 1 & 0 \\ -kl_q & 1 \end{pmatrix} \begin{pmatrix} x \\ x' \end{pmatrix}_{s_1} = \begin{pmatrix} 1 - kl_q l_d & l_d \\ -kl_q & 1 \end{pmatrix} \begin{pmatrix} x \\ x' \end{pmatrix}_{s_1} . \tag{2.9.4}$$

By squaring the expression for the final beam position x_2 the expression

$$\sigma_{x_2} = x_2^2 = (1 - kl_q l_d)^2 \langle x^2 \rangle_1 + 2l_d(1 - kl_q l_d)\langle xx' \rangle_1 + l_d^2 \langle x'^2 \rangle_1 \tag{2.9.5}$$

for the beam size after the drift length is obtained. It is a quadratic polynomial in k which contains all three second-order beam momenta at the starting point as coefficients. Measurement of the beam size for different quadrupole strengths allows to fit the beam momenta. Via Eq. 2.2.10 the transverse emittance is calculated.
As the whole particle beam reaches the observation screen a higher signal strength is given. Many variations of the quadrupole scan exist, like doublet scan, triplet scan, and multi-quadrupole scan. A more detailed explanation is given in Refs. [23, 52, 53].

2.9.4 Multiscreen Scan

The multiscreen scan is a special case of the quadrupole scan. Here, instead of changing the quadrupole magnet strength, it is kept constant. In order to obtain different accelerator optics needed for the calculation of the beam momenta the beam distribution is measured at different locations along the accelerator. An example of the multiscreen scan is given in Fig. 2.9. While the particle beam travels through the accelerator optics the phase space is permanently sheared. The alternating shearing in drift spaces and quadrupole magnets in a so-called *FODO* lattice has in total the effect of a rotation of the phase space ellipse, see Fig. 2.9 (top). The beam profiles allow to calculate the width of the projection of the phase space ellipse onto the spatial axis. As the rotation of the ellipse can be retraced from the accelerator optics a constrain for the shape of the phase space ellipse is given. With at least three non-equivalent rotations the phase space ellipse can be calculated via tomographic reconstruction. Ideally, the samples of the phase space are spread out evenly over the phase advance of π.
The advantage of this setup is the fact that the optics for the emittance measurement can be fully embedded into the standard accelerator optics. This makes the change of the quadrupole strength needless, which saves the time needed for the degaussing procedure. This is in particular beneficial for particle accelerators in user operation, and was therefore chosen for the Eu-XFEL [37]. A drawback is given by the need of an optics matching section upstream, to match the Twiss parameters into the diagnostics optics [37].

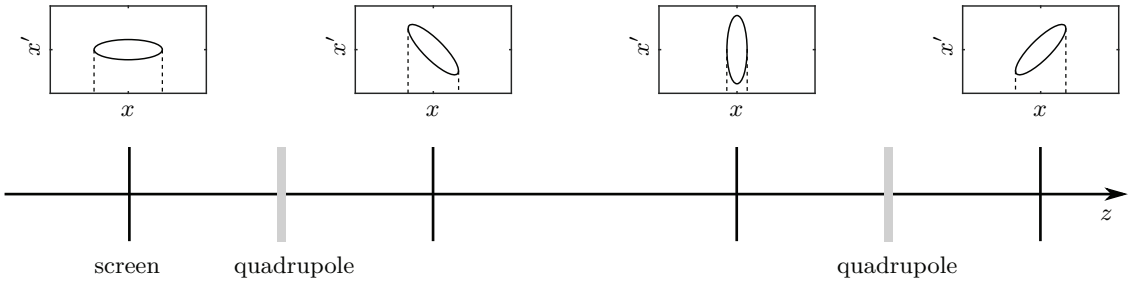

Figure 2.9: Scheme of the multiscreen scan. The beam profile from the beam image equals the beam profile from the phase space. During propagation through the accelerator lattice the phase space undergoes different shearing, which result in a rotation of the phase space. When measuring the beam profile for at least three different rotation angles the phase space can be reconstructed.

3 Photoinjector Test Facility at DESY in Zeuthen

The Deutsches Elektronen-Synchrotron (DESY) operates a photoinjector at its Zeuthen location. The Photoinjector Test Facility at DESY in Zeuthen (PITZ) had originally the task to develop, optimise and condition rf guns for the use as electron sources in high-gain free-electron lasers, such as FLASH at DESY and the European XFEL in Hamburg [22]. In 2021, the research activities at PITZ include experimental benchmarking of injector simulations, the development of laser pulse shaping methods and their application as photoinjector lasers for emittance minimisation [54], modelling of the photoemission process in high-gradient rf guns [55], next-generation long-pulsed electron gun development [56], and applications of high-brightness electron photoinjectors, such as the investigation of plasma wakefield acceleration and electron beam dynamics in plasma [57, 58], electron diffraction experiments [59] and accelerator-based generation of THz radiation [60].
This chapter will outline the facility and describe all subsystems which are used for slice emittance measurements.

3.1 Overview

A sketch of the whole beamline is given in Fig. 3.1. The electrons are created inside the rf gun by photoemission and accelerated to an energy up to 6.5 MeV and further accelerated in the booster cavity. Several diagnostics devices are installed in the low (energy) section, including

- Faraday cups for charge and dark current measurements,
- integrated current transformers for non-destructive charge measurements,
- three screen stations for measurement of the transverse beam size, distribution and position and
- a dipole magnet spectrometer for the measurement of the longitudinal beam momentum distribution.

The low energy section ends at the entrance to the cut-disk structure (CDS), the second accelerating cavity, serving as booster. There, the high energy section starts, which accelerates the beam to up to ~24.5 MeV. It is equipped with

- nineteen quadrupole magnets,
- three slit stations, which serve as emittance measurement system (EMSY),
- ten screen stations,
- a spectrometer dipole magnet,
- a transverse deflecting structure (TDS) and
- a plasma chamber.

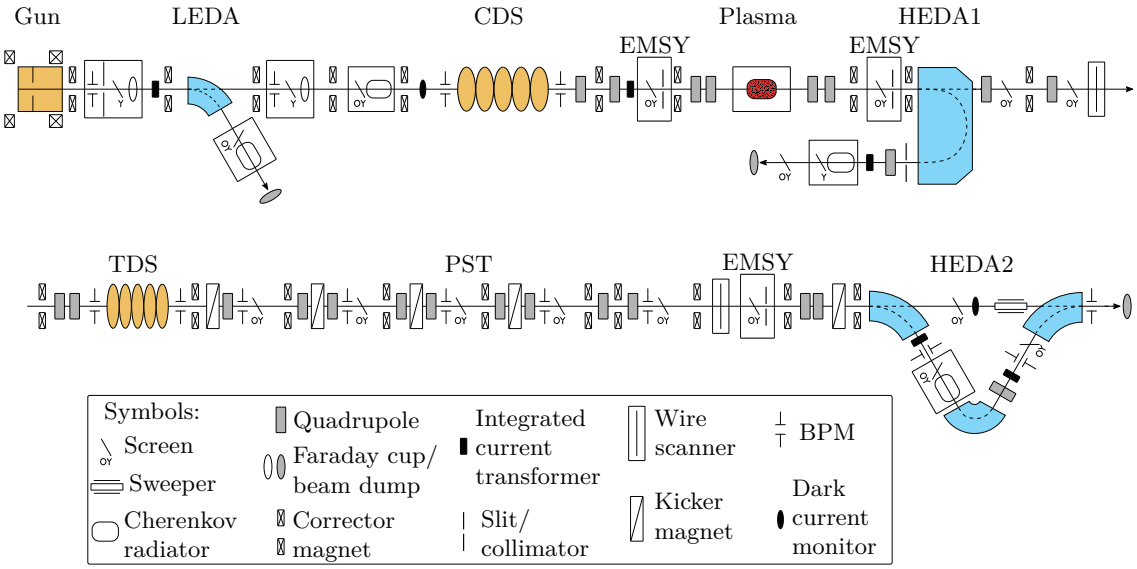

Figure 3.1: PITZ layout [61]. The beam is generated in the gun (top left) and travels then from left to right.

The plasma chambers however is only installed during plasma wakefield experiments, in which it replaces one of the screen stations.
The quadrupole magnets are used to focus and transport the beam. The three slit stations allow for emittance measurements with the slit scan method. The spectrometer dipole in the high section is used to determine the longitudinal electron beam momentum distribution after the booster cavity. The screen stations in the high section are used to measure the beam position and beam size. A transverse deflecting structure (TDS) is located in the high energy section. The TDS is a cavity which can provide a time-dependent vertical kick. This allows to imprint a correlation between vertical momentum and longitudinal position along an electron bunch, which after further beam transport translates to a y-z-correlation, allowing for time-resolved measurements with subpicosecond resolution.
Behind the rf deflector the phase space tomography module is located. After a section with matching quadrupole magnets a FODO section of quadrupole magnets and screen stations is located. The purpose of this section is to reconstruct the transverse phase space as described in Sec. 2.9. Behind the FODO section for tomography the third EMSY station is located. At the end of the beamline an energy spectrometer with horizontal deflection exists. In combination with the vertical deflection of the TDS this allows to measure the longitudinal phase space of the beam in a single shot. Besides the listed devices, several horizontal and vertical dipole corrector magnets are mounted along the beamline. These correctors are used to steer the beam through the beamline. The beamline is additionally equipped with beam position monitors (BPM) which allow non-destructive bunch charge and beam position measurement along the accelerator.
The electron beam is eventually terminated in the beam dump at the end of the beamline.

3.2 Photocathode Lasers

At PITZ, two photocathode laser systems are available to generate the electrons at the cathode. They both are located in the same laser room and share a ~25 m-long laser beamline from the laser room to the photocathode, allowing to switch between both lasers by moving in a mirror into the laser beamline.

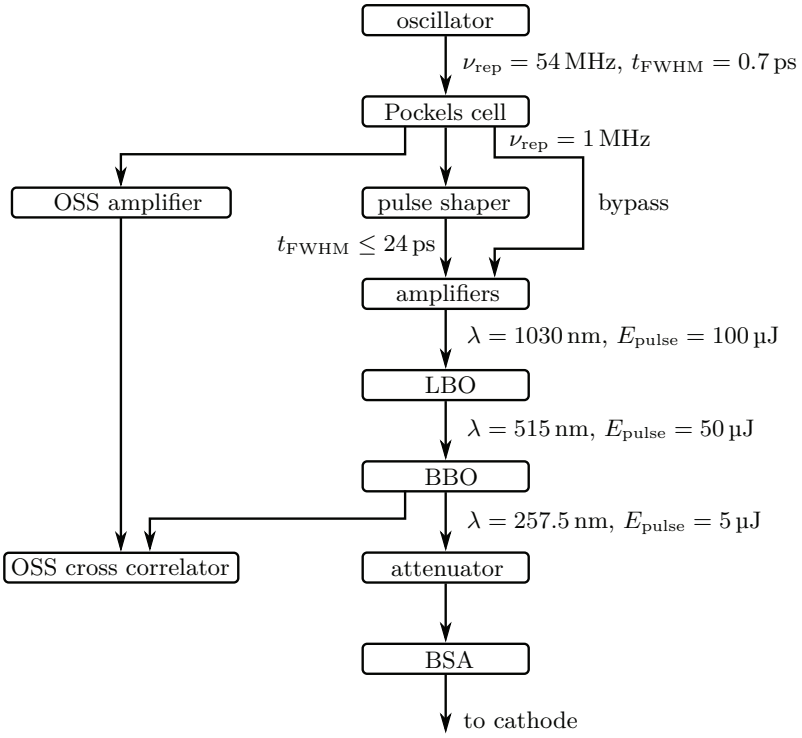

Figure 3.2: Flowchart about the different MBI laser stages. The oscillator generates pulses with a repetition rate of $\nu_{\mathrm{rep}} = 54\,\mathrm{MHz}$, a FWHM pulse length of 0.7 ps and a centre wavelength $\lambda = 1028\,\mathrm{nm}$. The pulses are then amplified, shaped and imaged onto the cathode.

3.2.1 MBI Laser

The first laser system at PITZ was developed and built by the Max-Born-Institute in Berlin, hence the name MBI laser [62]. An overview of the different stages of the MBI laser system is given in Fig. 3.2. It consist of a diode-pumped, mode-locked, infrared laser oscillator with a repetition rate of up to 54 MHz. A Pockels cell is used to couple out the laser pulses with a repetition rate of up to 1 MHz, which defines the repetition rate of the electron bunches. The laser pulses have a Gaussian temporal shape with a FWHM duration of 0.7 ps. In order to achieve a variety of laser pulse shapes and lengths the laser system is equipped with a pulse shaper, based on the pulse stacking method [63]. It consists of a series of 13 birefringent crystals. Each of the crystals splits the incoming laser pulse into two pulses, which are slightly shifted temporally due to the birefringence. This setup allows to create, for example, laser pulses with a flattop distribution with FWHM pulse length up to 24 ps [25], or triangular pulse profiles [58]. Alternatively, the pulse shaper can be bypassed to keep the short Gaussian temporal distribution of down to 1.5 ps, or the laser pulses can be spectrally filtered, reducing their spectral bandwidth, creating a ~ 7 ps-long Gaussian temporal distribution.

After this stage the laser pulse power is increased in two amplifier stages. Behind the second power amplifier the laser pulses are converted from a wavelength of 1030 nm to 515 nm in a LBO crystal, before conversion to 257.5 nm in a BBO crystal. The second non-linear crystal is succeeded by a $\lambda/2$ plate with a birefringent crystal, which separates the polarisations spatially, which is used as an attenuator. The laser is then imaged from the exit of the laser system via the laser beamline to an iris with variable size, the beam shaping aperture (BSA) [64, 65]. The BSA is imaged onto the photocathode and allows for a remote adjustment of the laser size on the cathode. The magnification of the imaging

optics from the exit of the MBI laser to the BSA is chosen such, that the laser beam size is larger than the BSA. Thus, when the BSA is largely over shone only the central part of the transverse laser pulse distribution is imaged onto the photocathode. This results in round laser profiles with transverse flattop distribution. However, the magnification of the laser beamline can also be changed, so that a larger part of the transverse Gaussian laser profiles is transmitted at the BSA. This allows to image laser pulses with a transverse Gaussian profile onto the photocathode, which are clipped at different radii. These truncated Gaussian distribution can lead to a reduced transverse emittance.
The laser system is also equipped with several diagnostic devices: The optical sampling system (OSS) cross-correlates the short IR laser pulses from the oscillator with the shaped UV pulses, allowing measurements of the temporal laser profile. A UV energy meter is used to measure the laser pulse energy, and a photodiode is used to monitor the laser pulse energy along the train of laser profiles. Finally, a UV camera at the virtual cathode position allows to measure the transverse laser profile [24, 66, 67].

3.2.2 PHAROS Laser

The PITZ facility has a second photocathode laser system based on a commercial 20 W front-end laser (PHAROS) [68]. The important feature of this system is its three-dimensional laser pulse shaping capability, based on spatial light modulators (SLMs) [69]. Here, the chirped laser pulse is dispersed with a grating onto the SLM, see Fig. 3.3. On the SLM mask the laser pulse has a correlation between frequency and transverse position. The mask modulates the polarisation of the laser pulses. The laser pulse is rearranged afterwards. At the polarising beam splitter only parts with a particular polarisation are coupled out, so that by changing the modulation of the SLM the shape of the output pulse is changed. Since the SLM is programmable, arbitrary pulse shapes in one of the space-frequency-planes can be achieved. By rotating the beam by 90 deg the second plane is modulated with another SLM mask setup. However, since both transverse planes are shaped individually the cylindrical symmetry is lost [54]. The beam transport from the laser table to the photocathode is the same as for the MBI laser system.

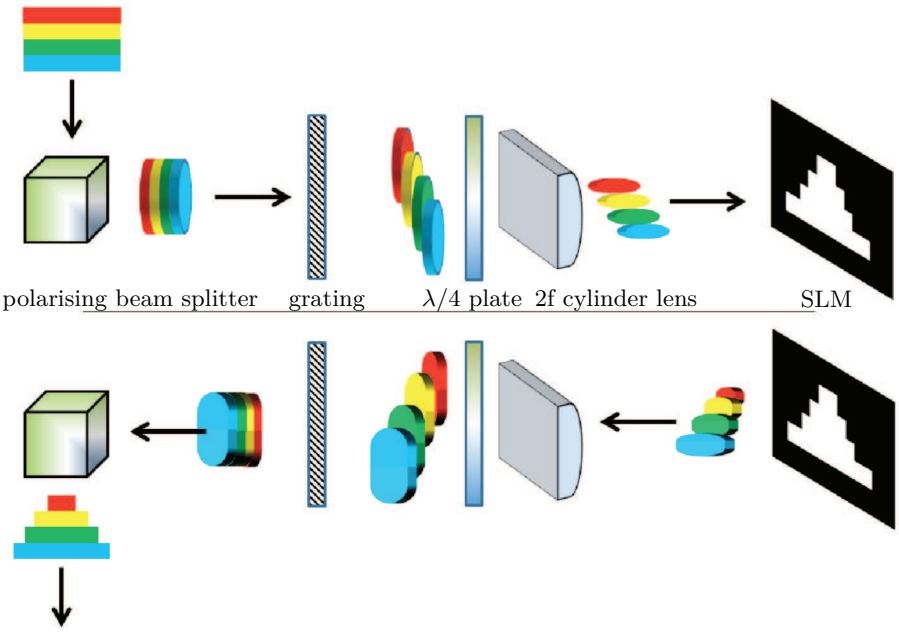

Figure 3.3: Scheme of the SLM mask-based pulse shaping technique. The beam is dispersed onto the SLM. The phase advance is shifted in one plane, leading to a modulation of the polarisation before the beam is rearranged again. At the polarising beam splitter only the parts of the laser with the correct polarisation are transmitted, allowing flexible pulse shapes. Adapted from [70].

3.3 Gun Cavity

In order to achieve a high-brightness electron beam a large amount of electrons has to be emitted from the cathode. To suppress the degradation of the beam quality due to strong space charge forces the beam has to be accelerated rapidly to relativistic energies. Thus, the photocathode is located inside an accelerating structure, the electron gun.
At PITZ, a normal conducting 1.6-cell standing-wave gun cavity operating at 1.3 GHz (L-band) is used. The cathode is located in the back wall of the half cell, where the axial peak electric field is located. A high quantum efficiency (QE) Cs_2Te semiconductor cathode is used to extract a high bunch charge at MHz repetition rate after illumination with a UV laser pulse.
In order to focus the beam for the emittance growth compensation as described in Sec. 2.7 the gun is surrounded by two solenoid magnets, see Fig. 3.4. The bigger magnet is the main solenoid magnet which is used to focus the beam, while the bucking solenoid is used to compensate the magnetic field of the main solenoid on the cathode surface, as a magnetic field on the cathode would spoil the beam quality.
The gun can operate at 10 Hz with a 650 µs rf pulse length [25, 71]. Within each rf pulse a peak rf power of 6 MW is supplied to the cavity, achieving an electric field strength of 60 MV/m. The bunch pattern of the PITZ facility is shown in Fig. 3.5. This bunch pattern is referred to as burst mode.

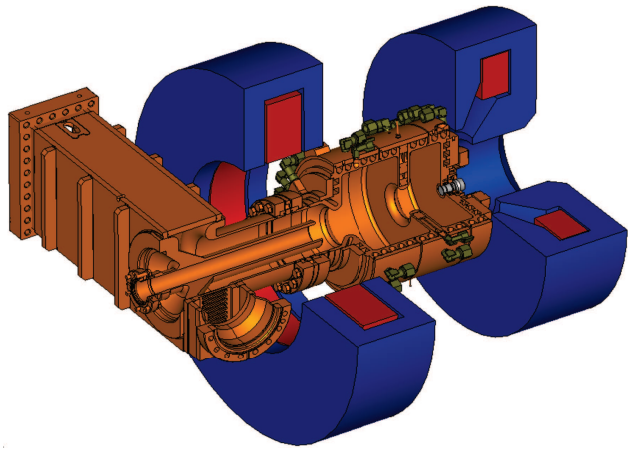

Figure 3.4: Normal-conducting 1.6-cell 1.3 GHz photoelectron gun, as used at PITZ, FLASH and European XFEL. The electrons are emitted from the photocathode (grey), which is located at the back wall of the half cell. The electromagnetic power is coupled into the gun cavity through the doorknob-type coaxial coupler. The cavity is surrounded by two solenoid magnets, in order to allow for emittance compensation, while keeping the magnetic field on the cathode surface at zero. Courtesy of I. Isaev.

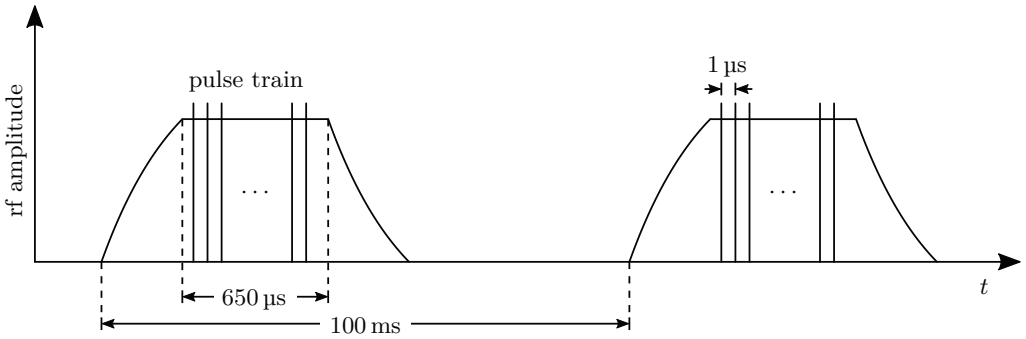

Figure 3.5: Time structure of the electron bunches at PITZ. The rf pulses and the bunch trains have a repetition rate of 10 Hz, the rf pulses a duration of up to 650 µs. Inside the rf pulses the electron bunches are spaced with 1 µs, i.e. a repetition rate of 1 MHz. Adapted from [37].

3.4 CDS Booster Cavity

The second accelerating cavity at PITZ is a cut-disk structure (CDS), build by the Institute for Nuclear Research in Troitsk, Russia [72, 73]. The CDS booster cavity is used to further increase the electron energy to suppress space charge forces and to reduce emittance oscillations. The cavity operates at a frequency of 1.3 GHz and has a nominal gradient of 12.5 MV/m, allowing to accelerate the electron beam to 24.5 MeV/c [25, 72, 73]. More information on the CDS booster cavity can be found in Ref. [72, 73] and references therein.

3.5 Quadrupole Magnets

The PITZ beamline downstream the CDS booster cavity is equipped with several Danfysik quadrupole magnets [27, 29, 74]. They have an effective length of almost 40 mm and

reach a magnetic field gradient of up to 8.4 T/m. The longitudinal gradient profile of a quadrupole magnet is shown in Fig. 3.6.

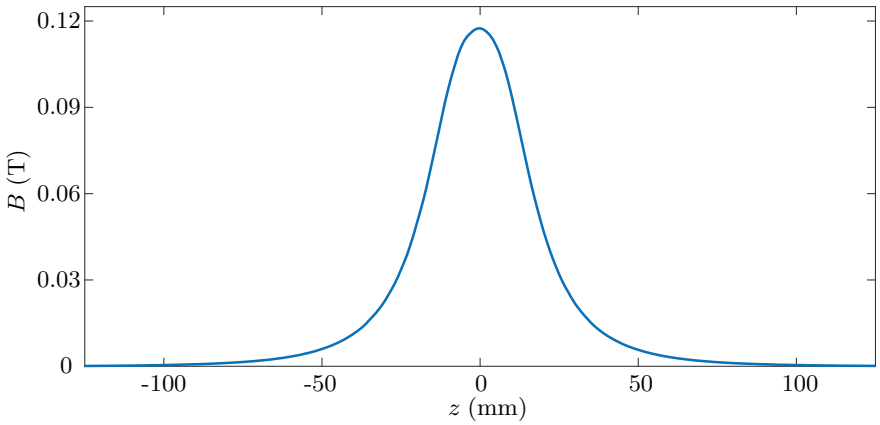

Figure 3.6: Longitudinal field map of one of the quadrupole magnets used at PITZ, measured at a radius of 16 mm.

3.6 Slit Stations

Three emittance measurement system (EMSY) stations are build into the PITZ beamline. They were designed in a collaboration of DESY and the Institute for Nuclear Research and Nuclear Energy in Sofia [75]. These allow to measure the transverse emittance with the single-slit scan technique, see Sec. 2.9. The slit stations are equipped with both vertical and horizontal actuators, which are moved precisely with stepper motors. On the actuators the 1 mm-thick tungsten slit masks are mounted [28]. The thickness is not enough to stop the electron beam, but sufficient to scatter it strongly. After a short distance downstream of the slit mask the contribution of scattered electrons to the beam images at the observation screen is homogeneous. The thickness of the mask was optimised, as a thinner slit mask will reduce the scattering and cause more background at the observation screen, while a thicker slit mask reduces the angular acceptance of the slits and therefore further reduces the signal-to-noise ratio [28]. To maximise the number of electrons passing the slit mask, the yaw and pitch angle of the whole station can be tuned on a mrad-range [28].
The slit masks at PITZ have two slits, one with a width of 10 µm and one with a width of 50 µm. The thinner slit allows to measure the projected emittance with a higher resolution and lower charge, therefore lower space charge effects, thus a smaller systematic error. The wider slit however transmits more electrons, leading to a higher signal-to-noise ratio on the observation screen, reducing systematic errors due low signal strength, e.g. from low-charged beams.
Besides the slit masks, the slit stations are also equipped with scintillator screens and simultaneously serve as screen stations. By comparing the beam size from the phase space, measured with the slit scan, and the direct beam size measurement on the scintillator screen at the slit location, the systematic error in projected emittance measurement is estimated.

3.7 Screen Stations

The screen stations are used to measure transverse beam profiles and the beam position. The beam profile is translated to a light signal either by optical transition radiation (OTR)

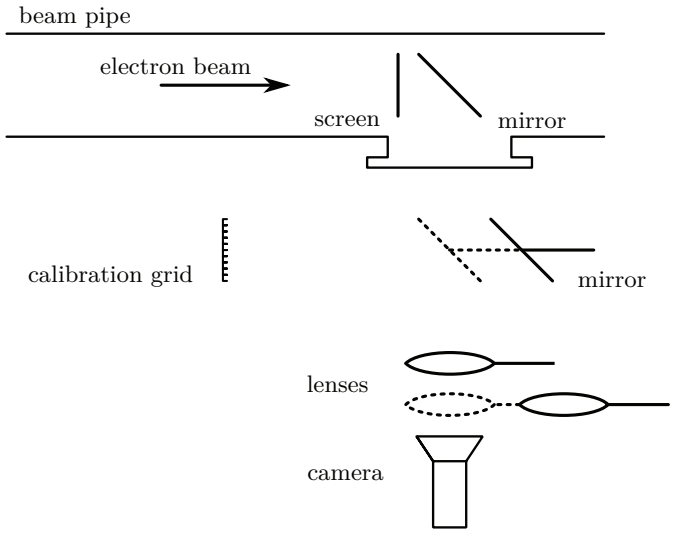

Figure 3.7: Schematic of the screen stations at PITZ. The screen and the first mirror are mounted on the same actuator. A single lens is used to image the screen onto the camera chip with few plane mirrors in between (not shown). A calibration grid, located at the virtual screen position is used to calibrate the magnification of the screen image to the camera. The stations are equipped with up to three lenses in order to change the magnification, or with a zoom lens with fixed magnification.

or by scintillation of the screen material. The light is imaged onto a CCD camera chip. In this thesis only measurements with scintillator screens have been used, as OTR screens only produce a relatively weak signal at low beam energies.
In scintillator screens the light generation mechanism works as follows: The particle beam loses energy when travelling through the scintillator due to inelastic scattering. The energy excites the scintillating molecules, which then emit light when relaxing. The distribution of the light intensity is the same as the local bunch charge density [76].
At PITZ, inorganic cerium-doped ytterbium aluminium garnet (YAG) powder screens and cerium-doped lutetium yttrium orthosilicate (LYSO) screens are used [77]. The light emission is around 550 nm for YAG and 428 nm for LYSO, while the decay constant is 70 ns and 50 ns, respectively [78, 79]. Since the YAG screens at PITZ consists of a layer of YAG powder with a thickness between 0.1 mm and 0.4 mm, which is sprayed onto a silicon substrate, the light output is moderate. For beam profile measurements with low charge density, i.e. low bunch charge or large beam profiles, LYSO screens are preferred over YAG screens, as these consist of a 500 µm-thick LYSO crystal, whose light yield is a factor ~ 70 higher w.r.t. the YAG screen [77]. The screens are mounted on actuators, which can be moved into and out of the beamline. The screens are installed perpendicularly to the beam direction, see Fig. 3.7. The scintillator light is coupled out of the beamline through a vacuum viewport via a 45 deg-mirror.
Most of the screen stations at PITZ are equipped with several movable lenses, from which only one is used at a time, to image the screen onto the chip of a CCD camera. This has the advantage, that different magnification factors, and thus, different spatial resolutions and different light yields, are achieved, which allows to measure beams with different sizes with high resolution. Few screen stations have a zoom lens to fulfil the imaging condition. The screen station PST.Scr1 has two screens and two imaging optics; one has two single lenses for imaging of the YAG screen, allowing measurements of beams with high charge density; the other one has a zoom lens for imaging of the LYSO screens to measure beams

with low charge density.
In order to determine the magnification between the screen image and the camera image accurately, a mirror can be inserted into the optical beam path, to image a calibration grid with known size onto the camera chip. The calibration grid has the same distance to the imaging optics as the screen. Some stations do not have the space for a movable mirror and a calibration grid. There, the screen holder on the actuator is used for calibration of the imaging optics. Both methods of optics calibration yield the same calibration factor within an uncertainty of 1 %.
In order to suppress the imaging distortions based on spherical aberration an iris is installed before the lens. This however reduces the sensitivity of the imaging optics, as part of the light is cut. Another source of imaging imperfections is chromatic aberration. Since the light emitted from scintillators has a narrow spectrum the setups chromatic aberrations are negligible.
A 12-bit CCD Prosilica GC 1350 from Allied Vision Technologies GmbH is used [80]. This camera has an array of 1360 × 1024 pixel, each with a size of 4.65 µm × 4.65 µm. Additionally, the camera can be operated in a 2 × 2-binned mode, in which four pixels are merged to a single macro pixel, reducing the spatial resolution. However, as the signal detected with each macro pixel is increased by a factor of four, the signal-to-noise ration is improved by a factor of two as the shot noise only increases with $\sqrt{\text{signal}}$. The camera is triggered and read out at 10 Hz with a minimal exposure time of 10 µs, thus supporting the bunch pattern at PITZ, see Fig. 3.5.

3.8 Transverse Deflecting Structure

In order to separate particles a transverse deflecting structure (TDS), based on the TM_{010} mode of a circular waveguide was fabricated and characterised at SLAC [81]. The deflection strength inside the LOLA-type cavity depends on both the TDS power and the rf phase a charged particle witnesses. Since the rf phase a particle experiences is related to its arrival time at the TDS cavity, particles at different longitudinal position of the beam will experience different transverse kicks. The TDS shearing principle is sketched in Fig. 3.8. Near the zero-crossing phase of the TDS, i.e. the phase with zero integrated transverse kick, the transverse deflection is linearly correlated to the TDS rf phase, i.e. the beam arrival time. The transverse kick translates into a spatial offset downstream the TDS cavity:

$$y = S \cdot z. \tag{3.8.1}$$

Here, y is the transverse particle offset, z is the longitudinal particle coordinate w.r.t. the

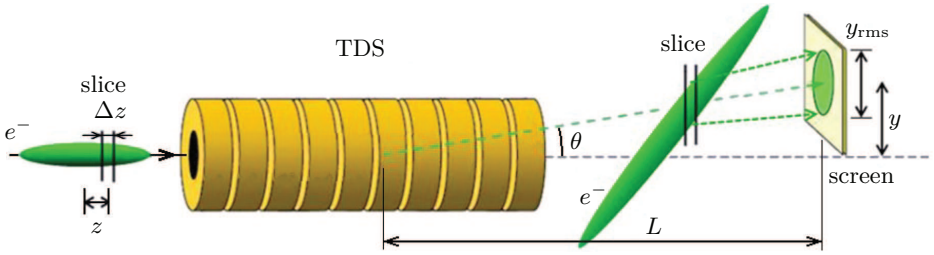

Figure 3.8: Operation principle of the TDS. The particles get a kick depending on their longitudinal position, which translates to a transverse offset on a downstream screen [40].

longitudinal beam centroid and S is the TDS shear parameter. The shear parameter can be written as

$$S = \frac{eV_0 k}{pc} R_{34}, \tag{3.8.2}$$

where R_{34} is the beam transport matrix element in the deflecting direction from the centre of the TDS to the observation point [40, 82]. It depends on the maximum TDS deflection voltage V_0, the electron charge e and the wave number $k = 2\pi f/c$ of the TDS, where f is the TDS frequency. Furthermore the shear parameter depends on the longitudinal momentum of the electrons p, as the kick $y' = p_y/p$ depends on both the longitudinal and the transverse momentum. For a simple drift of length L between the rf deflector and the observation point the shear parameter becomes

$$S = \frac{eV_0 k}{pc} L. \tag{3.8.3}$$

When more sophisticated accelerator optics are applied R_{34} from Eq. 2.2.5 has to be substituted in Eq. 3.8.2, yielding

$$S = \frac{eV_0 k}{pc} \sqrt{\beta_{y,1}\beta_{y,2}} \sin \mu. \tag{3.8.4}$$

Here, β_1 is the vertical beta function in the TDS centre, β_2 is the vertical beta function at the observation position and μ is the vertical phase advance between the TDS centre and the observation point.
Due to the correlation between transverse and longitudinal coordinate, several time-resolved beam properties can be extracted, i.e. the longitudinal bunch profile, the longitudinal phase space (if a dispersive element in the plane perpendicular to the TDS deflection plane is used) and the slice emittance. Besides being used as a diagnostics tool, rf deflectors are used in emittance exchange schemes and to increase the luminosity in circular colliders [83, 84, 85].
In 2015, a TDS, build in cooperation between DESY and the Institute for Nuclear Research in Troitsk, Russia, was installed at PITZ [39, 86]. It is a 3 GHz, travelling-wave S-band, LOLA-type structure, deflecting electrons vertically [39, 81]. An overview of the main parameters of the TDS installed at PITZ is presented in Tab. 3.1. An rf pulse length of 3 µs allows to deflect up to three bunches from the same train. Figure 3.9 shows the TDS as in 2017. It is surrounded by thermally insulating foam to improve the temperature stability. As the phase velocity is negative, the power is coupled into the cavity downstream, travels upstream inside the cavity and is dumped in a dummy load, which is located near the outcoupling cell at the upstream end. More technical details about the TDS installed at PITZ are given in Ref. [40].

Table 3.1: Specifications of the PITZ TDS [30].

RF Frequency	2997 MHz
Power	2.11 MW
Deflecting Voltage	1.7 MV
Pulse Length	3 µs
Length	0.533 m
Phase advance per cell	$2\pi/3$ mode
Number of cells	$14 + 2$

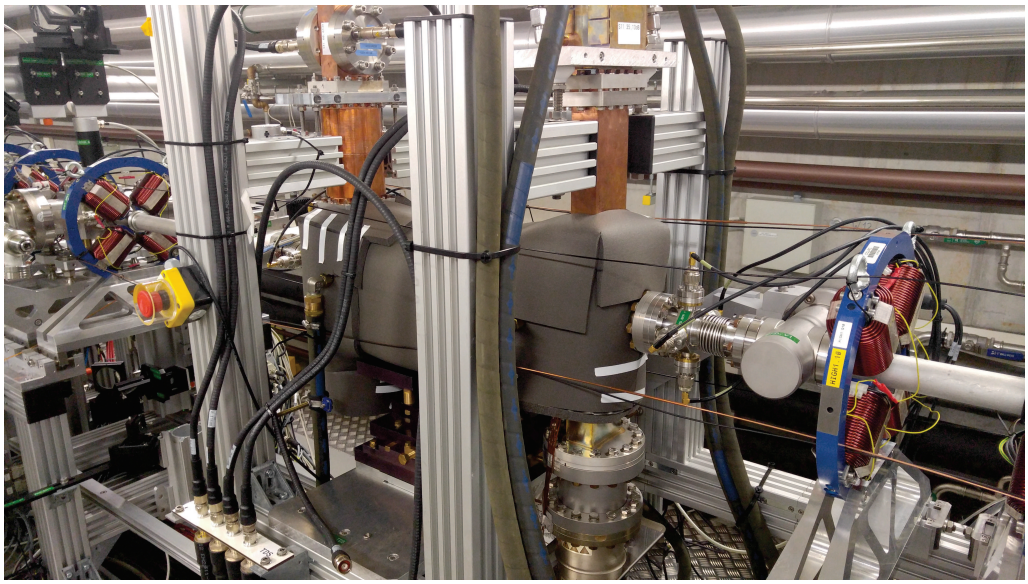

Figure 3.9: PITZ TDS. The rf is supplied at the downstream cell and travels upstream (left to right), i.e. in opposite beam direction. The power is dumped in a load located after the outcoupling cell. In order to improve temperature stability, the cavity was wrapped in thermally insulating foam. Courtesy of H. Huck.

3.8.1 Deflection Calibration

To determine the electron bunch length and temporal resolution the shear parameter S has to be calculated. Direct calculation of the shear parameter via. Eq. 3.8.2 might be complicated due to uncertainties in the effective TDS voltage V_0 and R_{34}. Therefore, the shear parameter is determined by beam-based calibration using the accuracy of the TDS rf phase.

The TDS shear parameter calibration is depicted schematically in Fig. 3.10. The TDS is operated at the zero-crossing phase, i.e. the electron beam experiences no net deflection from the TDS. Changing the TDS deflection phase by $\Delta\varphi$ leads to a change in net deflection. The beam centroid moves by Δy on the observation screen. The vertical centroid position in dependence of the TDS rf phase is measured. As the timing of the incoming particle beam

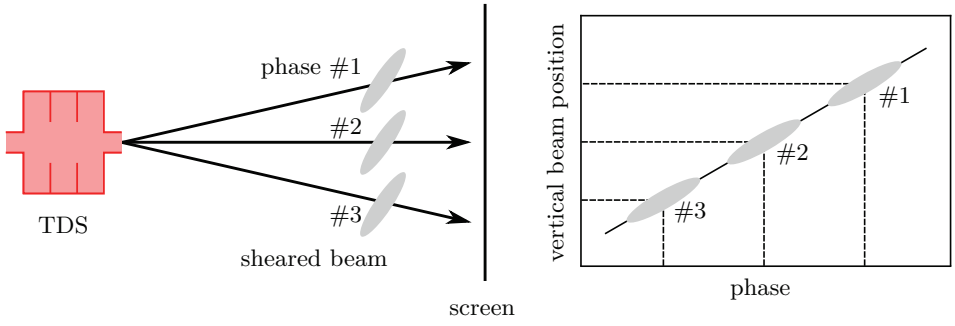

Figure 3.10: Scheme of the shear parameter calibration. The TDS rf phase is scanned in small steps around the zero-crossing phase. The change in rf phase is interpreted as change in arrival time of the bunch. The shear parameter S is given by the linear slope of the vertical mean position w.r.t. the TDS rf phase.

remains unchanged, the scan of the phase corresponds to a timing scan. Equation 3.8.1 can be modified to

$$\Delta y = S \cdot \Delta z = S\frac{\Delta\varphi}{k}, \tag{3.8.5}$$

where k is the cavity wave number $k = 2\pi/\lambda$ and λ the TDS rf wavelength. The slope of the linear fit of the vertical centroid position versus the TDS rf phase determines the TDS shear parameter.

3.8.2 Bunch Length Measurement

When the TDS shear parameter is calibrated and the zero-crossing phase is found the bunch length can be measured. A beam with an rms bunch length of z_{rms}, an initial shear parameter S_0, and a vertical emittance ϵ_y has a vertical beam size of

$$y_{\mathrm{rms}}^2 = \beta_y(s)\epsilon_y + (S + S_0)^2 z_{\mathrm{rms}}^2 \tag{3.8.6}$$

on the observation screen, after it is deflected with a TDS. It consists of contributions from the nominal vertical beam size $\sqrt{\beta_y(s)\epsilon_y} = y_{0,\mathrm{rms}}$, given by the vertical emittance and vertical beta function at the screen position; an initial y-z-correlation exists along the beam, characterised by S_0, where $S_0 = 0$ describes the case without initial correlation; and the TDS-induced y-z-correlation, displayed by the shear parameter S as defined in Eq. 3.8.2.
Equation 3.8.6 is a quadratic equation in S. Measuring the vertical beam size for different shear parameters S allows to determine the rms bunch length z_{rms}, the initial shearing S_0, as well as the contribution from the nominal vertical beam size $\beta_y(s)\epsilon_y$.
Measurements at three different shear parameters is sufficient to determine all parameters. For this, the TDS voltage might be varied. In practice however rather the shear parameter at both zero-crossing phase is used, where the shear parameters have a different sign; and the case with the TDS off, i.e. $S = 0$, is used.
When the TDS is off and no y-z-correlation exists along the beam, the vertical beam size is determined by the vertical emittance and vertical beta function at the screen position $\beta_y(s)\epsilon_y = y_{0,\mathrm{rms}}^2$. This term imposes a resolution limitation to Eq. 3.8.1, where the non-sheared beam size was neglected. When studying the sheared vertical bunch profile on the observation screen, any temporal feature smaller than the unsheared beam size cannot be studied. The unsheared vertical beam size determines the time resolution of the measurement. In this case

$$\beta_y(s)\epsilon_y = (S + S_0)^2 z_{\mathrm{res}}^2 \tag{3.8.7}$$

holds, where z_{res} is the longitudinal resolution. Therefore, when $S_0 = 0$ the longitudinal resolution is given by

$$z_{\mathrm{res}} = \frac{\sqrt{\beta_y(s)\epsilon_y}}{S} = \frac{\sqrt{\epsilon_y}}{\sqrt{\beta_1}\sin\mu}\frac{pc}{eV_0 k}, \tag{3.8.8}$$

when the shear parameter from Eq. 3.8.4 is used. Correspondingly, the time resolution is given by

$$t_{\mathrm{res}} = \frac{z_{\mathrm{res}}}{c}. \tag{3.8.9}$$

The left side of Eq. 3.8.8 shows, that for a reduction of the resolution, the unsheared vertical beam size has to be minimised on the observation screen, while the deflection strength must be maximised.

3.8.3 Beam Deterioration in RF Deflectors

According to the Panofsky-Wenzel theorem [87], transverse deflection due to the rf field is caused by the transverse gradient of longitudinal accelerating field. The induced rms energy spread is given by

$$\sigma_E = ekV_0\sigma_y \cos\varphi, \tag{3.8.10}$$

where σ_y is the vertical rms beam size inside the TDS and $\cos\varphi = 1$ for passage of the bunch through the deflector at zero-crossing phase [88]. Comparison with Eq. 3.8.4 shows, that a larger shear parameter leads to an increased TDS-induced rms energy spread. The beam dynamics of rf deflectors is discussed in more detail in Ref. [88].

4 Slice Emittance Diagnostics at PITZ

At PITZ, the single-slit scan technique is used to measure the projected emittance [23, 24, 25, 28]. Here, the slit station EMSY1 is used to cut-out beamlets, which are then observed at the screen station High1.Scr4, see Appendix A for details. For slice emittance measurements, High1.Scr4 cannot be used, as it is located upstream the TDS. Hence, the first screen station behind the transversely deflecting structure (TDS), i.e. PST.Scr1 is used as target screen for the measurements. In order to compare projected and slice emittance measurements the same slit station has to be used in the measurements. The resulting drift length of 7 m leads to big beamlet images, making the slice emittance measurements prone to emittance underestimation, as the signal strength is small. Additionally, a bigger vertical beam size σ_y on the observation screen leads to a worse time resolution. To overcome these issues, quadrupole magnets are used behind the slit mask to focus the beamlets for a higher signal strength and better time resolution.
First, a comparison of beam properties between PITZ and the Eu-XFEL injector are done to motivate the use of slit masks for emittance measurements over quadrupole-based methods. Then the slice emittance measurement scheme used at PITZ as well as its differences to a slit scan with a pure drift is outlined. Next to this, a way to determine the applied accelerator optics is explained, as well as the image analysis procedure applied to the slice emittance measurement data is shown. Finally, systematic emittance underestimation based on the finite signal-to-noise ratio in experiment are estimated using start-to-end simulations using ASTRA [41].

4.1 Emittance Measurements

High-energy electron linear accelerators make use of quadrupole scan and multiscreen scan for emittance and slice emittance measurements. These can be used, as the envelope dynamics is governed by the emittance. Whether this is the case, can be seen when comparing both terms from the beam envelope equation, see Eq. 2.4.1 and Eq. 2.4.2. This is done by calculating the ratio R [89] of the two terms:

$$R = \frac{I\sigma_x^2}{2I_\mathrm{A}\epsilon^2\gamma}. \tag{4.1.1}$$

It was assumed, that the beam size in the horizontal and vertical plane are same, i.e. $\sigma_x = \sigma_y$. The following beam properties are achieved for the electron beam at the injector at the Eu-XFEL:

$$\begin{aligned} E_\mathrm{beam} &= 130\,\mathrm{MeV}, \\ Q &= 250\,\mathrm{pC}, \\ \sigma_x &= 0.15\,\mathrm{mm}, \\ \epsilon_{\mathrm{n},x} &= 0.5\,\mu\mathrm{m}, \text{ and} \\ \sigma_z &= 4\,\mathrm{ps}. \end{aligned}$$

With the beam size $\sigma_x = \sqrt{\beta_x\epsilon_\mathrm{geom}}$ and the current $I = Q/\sigma_z$ the ratio can be calculated to be

$$R_\text{Eu-XFEL} = 0.16 < 1, \tag{4.1.2}$$

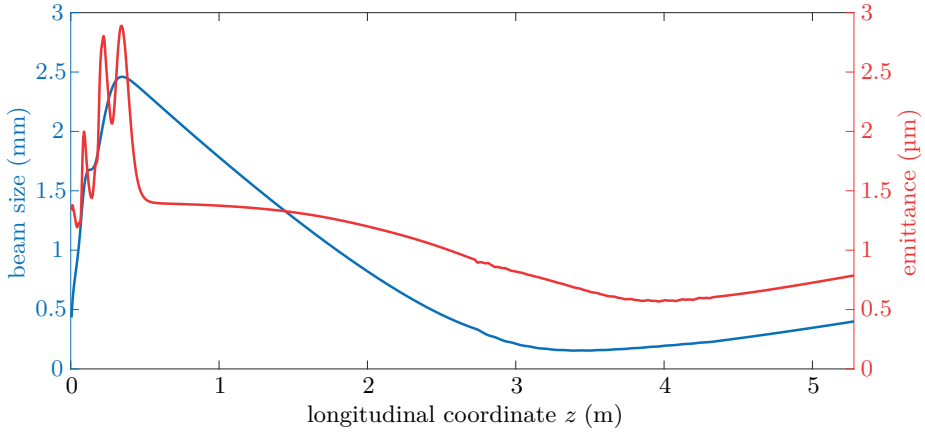

Figure 4.1: Evolution of the beam size (blue) and transverse projected rms emittance (red) from the cathode to the slit station EMSY1 in simulation. The bunch charge in the simulation was 250 pC, while the main solenoid current was set to 361 A to yield minimal projected emittance.

i.e. the beam is emittance-dominated according to the criterion based on the beam envelope equation. Typical beam parameters for a 250 pC operation at PITZ are

$$\begin{aligned} E_{\text{beam}} &= 20\,\text{MeV}, \\ I &= 20\,\text{A}, \\ \sigma_x &= 0.2\,\text{mm}, \text{ and} \\ \epsilon_{\text{n},x} &= 0.5\,\mu\text{m}. \end{aligned}$$

The evolution of the beam size and transverse projected emittance at PITZ from the cathode to the slit station EMSY1 is depicted in Fig. 4.1. These parameters lead to the fraction

$$R_{\text{PITZ}} = 2.40 > 1, \tag{4.1.3}$$

which demonstrates, that the electron beam at PITZ is space-charge-dominated. Therefore, quadrupole scan and multiscreen scan cannot be used easily. Therefore a slit mask is used to cut-out beamlets from the whole beam. An aperture of $\Delta x_{\text{slit}} = 50\,\mu\text{m}$ leads to a transverse beam size of

$$\sigma_{\text{after slit}} = \frac{\Delta x_{\text{slit}}}{2\sqrt{3}} = 14.4\,\mu\text{m} \tag{4.1.4}$$

right after the slit. When a Gaussian beam profile

$$f(x) = \frac{1}{\sqrt{2\pi}\sigma} \exp\left[-\frac{1}{2}\frac{x^2}{\sigma^2}\right] \tag{4.1.5}$$

is assumed in the transverse plane, the transverse beam intensity becomes

$$f(0) = \frac{1}{\sqrt{2\pi}\sigma} \tag{4.1.6}$$

in the centre, with

$$\int_{-\infty}^{\infty} f(x)\,\mathrm{d}x = 1. \tag{4.1.7}$$

When the slit is centred w.r.t. the beam, a charge fraction of

$$\text{charge fraction} = \frac{\sigma_{\text{after slit}}}{\sqrt{2\pi}\sigma_x} \approx 0.03 \tag{4.1.8}$$

of the total bunch is passing the slit. This leads to a reduced bunch current of

$$I_{\text{after slit}} = 0.6\,\text{A} \tag{4.1.9}$$

after the slit. The transverse emittance reduces similarly as the transverse beam size, leading to a fraction

$$R_{\text{after slit}} = 0.07 < 1 \tag{4.1.10}$$

after the slit in the plane, in which the slit is cutting. This value reduces further, when a smaller slit width is used, or a larger transverse beam size at the slit position is achieved. This result shows, that the electron beam at PITZ is emittance-dominated after passing the slit. Therefore, the slit scan is used to measure the emittance at PITZ.

4.2 Projected Emittance Measurements at PITZ

The projected emittance at PITZ is measured using the slit-scan technique [23, 24, 25, 26, 27, 28, 29]. Here, the slit station EMSY1 is used to cut-out emittance-dominated beamlets. When the slit position is scanned transversely the local divergence of the beam is determined on an observation screen downstream the slit mask. This allows to reconstruct the projected phase space, which in turn allows the projected emittance calculation. The control of the slit station, data taking, image analysis, phase space reconstruction and emittance calculation is done with a C code named *fastscan*. Usually the slit with 10 µm opening is selected for the measurement to reduce the space charge effect and improve the resolution. The slit mask actuator moves with a speed allowing to nominally take images when the slit moved 10 µm.
The beamlets are observed on a YAG screen at the screen station High1.Scr4, which is located 3.13 m downstream the slit mask. The number of electron bunches is adjusted to ensure a high signal-to-noise ratio. This is done by achieving 2000 counts for the peak signal, while a camera pixel can have maximally 4095 counts.
The second-order beam moments are calculated from the projected phase space, which allow to calculate the normalised emittance according to Eq. 2.2.10 and Eq. 2.2.14. However, the beam size is also measured on a YAG screen, installed at the slit station. This beam size σ_x is often slightly larger the the phase space beam size $\sqrt{\langle x^2 \rangle}$, as the low signal-to-noise ration at the outer slit positions lead to an underestimation of the phase space size. The fraction between both is used to calculate the *scaled* emittance according to

$$\epsilon_{\text{scaled}} = \frac{\sigma_x}{\sqrt{\langle x^2 \rangle}} \epsilon_{\text{norm}}, \tag{4.2.1}$$

where ϵ_{norm} is the normalised emittance from Eq. 2.2.14, see Ref. [25]. The scaling factor is then used to estimate the systematic error of the fastscan measurement: The unscaled emittance ϵ_{norm} is regarded as lower limit, the upper limit is given by

$$\epsilon_{\text{scaled}^2} = \left(\frac{\sigma_x}{\sqrt{\langle x^2 \rangle}} \right)^2 \epsilon_{\text{norm}}, \tag{4.2.2}$$

the squared-scaled emittance value. This generally leads to an asymmetric error. In order to estimate a statistical uncertainty, the measurement is repeated nine times, while the beam size measurement is done three times.
The projected emittance can be measured both in the horizontal plane x and vertical plane y. Then the x-y-emittance is calculated via

$$\epsilon_{xy} = \sqrt{\epsilon_x \epsilon_y}, \tag{4.2.3}$$

where ϵ_x and ϵ_x are the scaled emittance in the horizontal and vertical plane, respectively. Note, that this is not the same as the transverse 4d-emittance, as the correlation terms between the two transverse planes are not determined here. More insight in machine optimisation for operation with low emittance is given in Ch. 6.

4.3 Slice Emittance Measurements Scheme

The setup for slice emittance measurements, which includes a TDS, is sketched in Fig. 4.2. The rf deflector might also be placed before the slit mask. At PITZ, the vertical deflection allows to measure the slice emittance in the horizontal plane. An overview of the PITZ beamline between the booster exit and the PST.Scr1 is shown in Fig. 4.3. The PITZ TDS is far away from the booster cavity, which causes a long distance between the two existing slit stations (EMSY1 and EMSY2) and the first screen after the TDS: The drift distance from the routine emittance measurement station EMSY1 to PST.Scr1 is 7 m, which is a factor of ~ 2 larger than for the projected emittance measurements. Such a long drift not only leads to a moderate vertical beta function, which degrades the time resolution of measurements with the TDS according to Eq. 3.8.8, but more importantly, also reduces the charge density on the observation screen, leading to a lower signal-to-noise ratio (SNR). In addition, the TDS rf pulse length allows to deflect only up to three electron bunches (much less than can be used for projected emittance measurements), which makes the low SNR during beamlet size measurements a major problem during slice emittance measurements. Therefore, the slice emittance measurements are carried out with the use of focusing quadrupole magnets behind the slit station. After a pure drift the angular distribution at the slit mask is given by the spatial distribution divided by the drift length L. When using focusing magnets, the spatial distribution on the observation screen is narrower, leading to a higher charge density. The setup is depicted in Fig. 4.4.
With the quadrupole focusing, R_{12} from the slit mask to the observation screen is reduced, similar to a reduced drift length for a slit scan.
Conversely, the calculation of the angular distribution after the slit mask from the spatial distribution on the observation screen is complicated due to the use of focusing elements. According to the transfer matrix, the transverse position x_2 of a particle at the screen station PST.Scr1 is given by

$$x_2 = R_{11}x_1 + R_{12}x_1', \tag{4.3.1}$$

see Eq. 2.1.3. During the slit scan, the initial transverse position x_1 of the particles is well-known, as the slit position is known with high precision. The transfer matrix elements R_{11} and R_{12} can either be calculated based on magnetic models or measured with trajectory

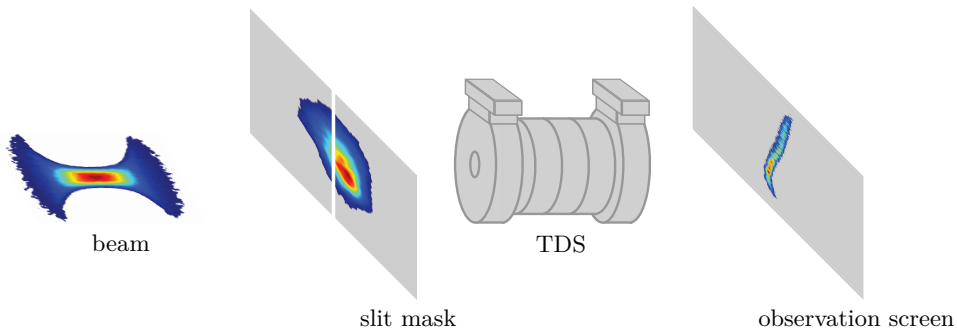

Figure 4.2: Combination of the slit scan method for projected emittance measurement with the TDS allows for slice emittance measurements. The deflection is vertical, the (slice) emittance measurement is in the horizontal plane.

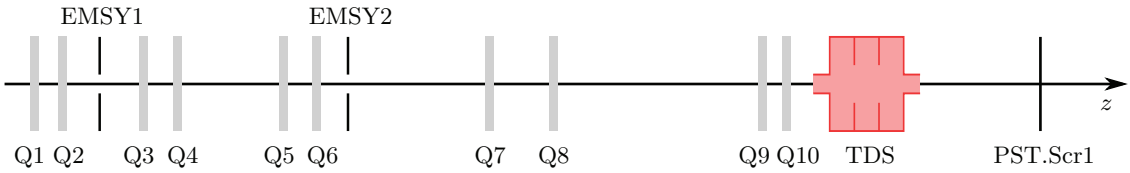

Figure 4.3: Schematic of the PITZ beamline after the booster. The beam travels from left to right. Only quadrupole magnets and EMSY stations between the booster exit and PST.Scr1 are shown. The longitudinal axis z is to scale. Coordinates and further elements can be found in Tab. A.1.

response techniques.
Then the angular distribution $f(x_1')$ is connected with the spatial distribution $f(x_2)$ via the relation

$$f(x_1') = f\left(\frac{x_2}{R_{12}} - x_1\frac{R_{11}}{R_{12}}\right). \tag{4.3.2}$$

Equation 4.3.2 proves that the angular distribution at the slit position can be calculated from the spatial intensity distribution at the screen position, when the beam optics elements R_{11}, R_{12} and the slit position x_1 are known. According to Eq. 2.2.10, the squared beam size $\langle x^2\rangle$, the squared angular spread $\langle x'^2\rangle$ and the beam divergence $\langle xx'\rangle$ have to be identified to calculate the (slice) emittance. These three properties are calculated from

- the local angular spread σ_m' a beamlet has at the mth slit position,
- the local beamlet divergence $x_{m,c}'$ a beamlet has the mth position, and
- the beamlet charge (intensity) I_m, usually described by the sum of pixel on the observation screen.

The local beam divergence is calculated by comparing the beamlet centroid position x_m on the screen with the slit position while considering the optics elements R_{11} and R_{12}:

$$x_{m,c}'|_{\text{ini}} = \langle x_m - mwR_{11}\rangle/R_{12}, \tag{4.3.3}$$

where the slit position is denoted with mw, where w is the spacing between neighbouring slit positions. The transfer matrix element R_{11} accounts for the magnitude of spatial offset the beamlet has on the screen based on the spatial offset of the slit position. The interpretation of spatial distribution on the observations screen in angular domain at the slit position is taken into account by R_{12}.
Calculation of the second-order rms beam moments requires the absolute beam angle $\langle x'\rangle$ and position $\langle x\rangle$ to vanish. As this correction is not yet carried out in Eq. 4.3.3 it only shows the initial local beam divergence $x_{m,c}'|_{\text{ini}}$, which is adjusted later.
The local beamlet angular spread σ_m' is derived from the rms beamlet size on the screen via

$$\sigma_m' = \sqrt{\langle x_m^2\rangle/R_{12} - x_{m,c}'^2}, \tag{4.3.4}$$

where $x_{m,c}'^2$ considers the beamlet centroid position. Equations 4.3.3 and 4.3.4 are equations for an arbitrary optic R_{11} and $R_{12} \neq 0$, while Ref. [89] shows it for a pure drift from slit to screen, i.e. $R_{11} = 1$ and $R_{12} = L$.
For the calculation of the second-order beam moments the beam position and angle have to be centred in phase space. This is done by subtracting the charge-weighted average values from the initial beamlet centroid and angle, i.e.

$$x_{m,c} = (x_{m,c}|_{\text{ini}} - x_c) = mw - \frac{w\sum_{m=1}^{N} I_m m}{\sum_{m=1}^{N} I_m} \tag{4.3.5}$$

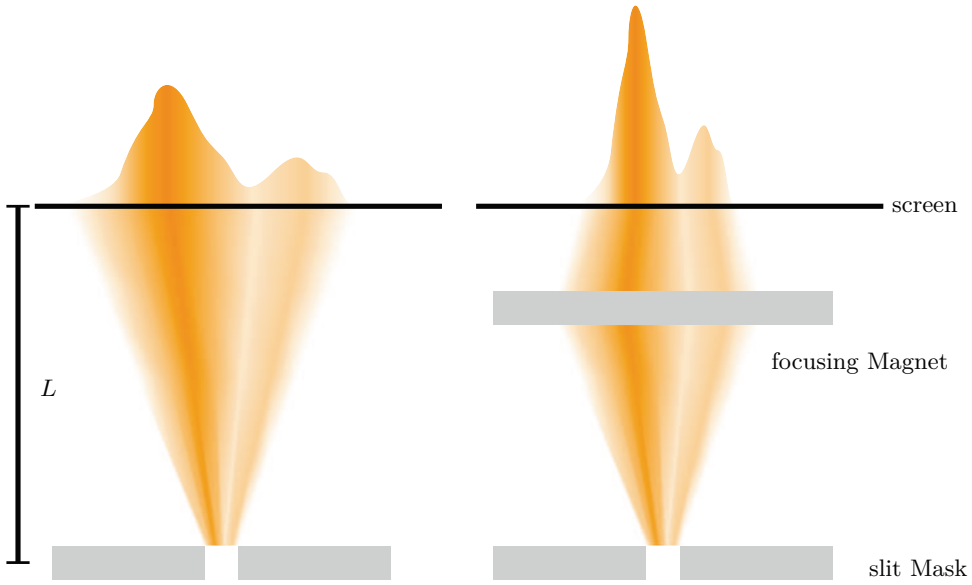

Figure 4.4: Particle trajectories in a slit scan experiments without (left) and with the use of focusing magnets (right). The angular distribution at the slit mask translates to a spatial distribution on the screen in both cases. While in the left case the reconstruction is easier, as the drift length is known with high accuracy, it is more complicated in the right case as the transfer matrix elements R_{11} and R_{12} have to be known precisely for a correct phase space reconstruction. The advantage however is the higher signal strength on the screen.

and

$$x'_{m,c} = (x'_{m,c}|_{\text{ini}} - x'_c) = x'_{m,c}|_{\text{ini}} - \frac{\sum_{m=1}^{N} I_m x'_{m,c}}{\sum_{m=1}^{N} I_m}. \tag{4.3.6}$$

This allows to calculate the three second-order beam momenta. The squared rms beam size is determined by calculating the charge-weighted squared beamlet position

$$\langle x^2 \rangle = \frac{\sum_{m=1}^{N} I_m x_{m,c}^2}{\sum_{m=1}^{N} I_m}. \tag{4.3.7}$$

Similarly, the divergence $\langle xx' \rangle$ is derived as charge-weighted product of beamlet position (centre-corrected slit position) and local beamlet divergence

$$\langle xx' \rangle = \frac{\sum_{m=1}^{N} I_m x_{m,c} x'_{m,c}}{\sum_{m=1}^{N} I_m}. \tag{4.3.8}$$

The squared angular beam divergence $\langle x'^2 \rangle$ is determined via

$$\langle x'^2 \rangle = \frac{\sum_{m=1}^{N} I_m \left(x'^2_{m,c} + \sigma'^2_m \right)}{\sum_{m=1}^{N} I_m}. \tag{4.3.9}$$

Here the local beamlet divergence and local angular beamlet spread are summed up quadratically, before the charge-weighted average over all slit positions is computed. The three second-order beam moments now allow (slice) emittance calculation via Eq. 2.2.10. While the transfer matrix element R_{11} is required for a calculation of the angular spread and the correlation term $\langle x_1 x'_1 \rangle$ at the slit position, it is not important for the emittance calculation, as this term describes the linear correlation between angle and beam position,

which is subtracted during the emittance calculation, as indicated by Eq. 4.3.2. As the beam size is changing along the longitudinal coordinate z of the bunch, the slice beam size at the slit position must be used for the scaling of slice emittance measurements. This however cannot be measured at PITZ, therefore no scaling of slice emittance values is done.
Figure 4.5 shows, how the centre slice phase space is reconstructed from the raw images. In the first image (a) the raw beamlet image during a slice emittance measurement is shown. The image was taken at the screen station PST.Scr1. In the first step the background and noise are removed from the beam image. This procedure is discussed in Sec. 4.5. The subplot (b) shows the filtered camera image. In this example, the peak signal intensity is normalised to 1. The colour scale is kept between 0 and 1, while the possibly occurring negative pixel values are kept white. The background and noise cut is applied to beamlet images at all slit positions. For this, the operator checks the slit position range in which the beam signal on the observation screen is seen. The slit scanning range is then selected to be slightly larger, usually by few hundred micrometers.
The overlap of all filtered beamlet images is shown in (c). The vertical bunch profile, i.e. the temporal bunch profile is shown as well. The pixel values y, in which the temporal bunch profile drops to 0.1 % of the maximum value are determined, as these give the temporal peak-to-peak limits of the bunch. The 0.1 % criterion was chosen, as it is more robust than selecting the range, at which the bunch profile drops to zero. Anyhow, such small bunch currents can be neglected, as their contribution to the bunch profile, slice emittance, as well as to free-electron lasing is negligible [19].
The temporal peak-to-peak range is then divided into several slices. In this thesis, the beam is usually cut into 11 slices. In frame (d) the filtered beamlet image from (a) is shown, where the bunch and slice borders of the temporally-centred slice are marked by the black lines. The centre slice distribution from this beamlet image is shown in (e). The projection onto the horizontal axis x contains the angular distribution of the electrons at this slit position. The projection is put into the centre slice phase space, seen in (f). Here, a different colour scale is chosen to distinguish between real space and phase space images. After this is repeated for all slit positions, image (g) is obtained. It shows the horizontal phase space of the centre slice. During the phase space reconstruction the divergence distribution has to be corrected by $x_1 \cdot R_{11}/R_{12}$, as indicated by Eq. 4.3.2. This corrects the contribution of the slit position to the average beamlet position on the observation screen, which is important for a correct calculation of the correlation term $\langle xx' \rangle$.
In the final reconstruction step the slit position is turned into a spacial coordinate, while the horizontal pixel coordinate is turned into the angular dimension by the screen-to-camera calibration factor and R_{12}. Finally, the emittance of the centre slice can be calculated from panel (h).

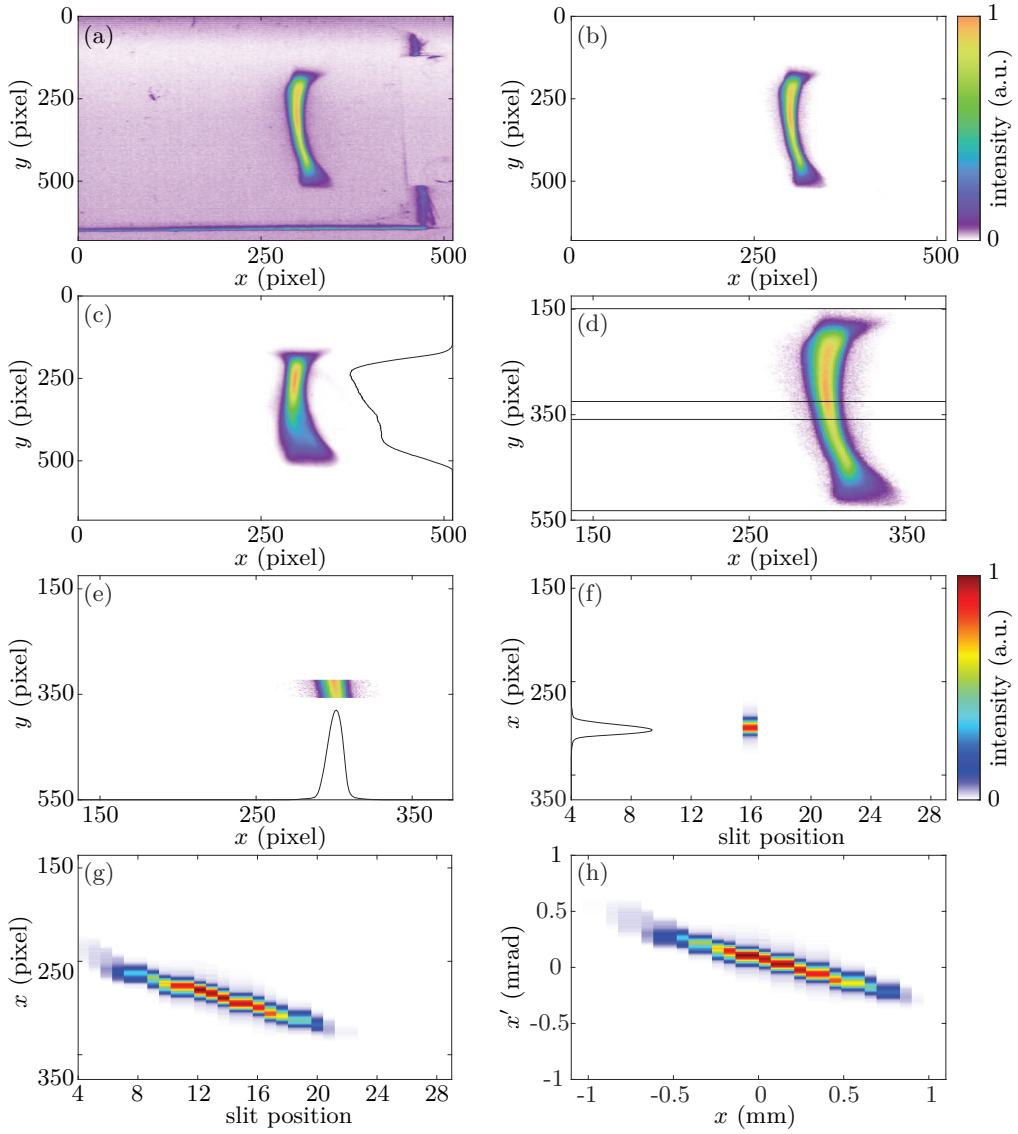

Figure 4.5: Reconstruction of (slice) phase space from beamlet images. The raw beamlet image at the 16th slit position is shown in (a). As the beamlets are deflected with the TDS the vertical axis y also corresponds to the temporal axis, while the horizontal axis x is simultaneously the angular axis x'_1. The beamlet image from (a) is filtered, see (b). All filtered beamlet images are added up before the vertical projection (the temporal bunch profile) is calculated (c). Here the temporal peak-to-peak bunch limits are determined for later temporal slicing of the images. In (d), the upper and lower peak-to-peak limit of the whole beamlets, as well as the upper and lower limit of the central temporal slice are shown. The horizontal projection of the central slice of this beamlet is shown in (e). The horizontal projection in (e) is added to the slice phase space, see (f). If done for all beamlet images (all slit positions) the whole transverse phase space of the central slice is obtained (g). Finally, the slit position and camera pixel are translated to x and x' and the phase space centroids are shifted to zero, so that the mean values vanish, see (h). The colour map has 0 as lower limit, even for the images with negative pixel values, i.e. (b) to (e).

4.4 Online Calibration of Transport Matrix Elements

While the slit-scan measurement using quadrupole magnets has an advantage in higher sensitivity compared to a pure drift space, precise knowledge of R_{11} and R_{12} is crucial for the phase space reconstruction. In order to exclude systematic errors in the slice emittance calculation from faulty transfer matrix elements due to a wrong accelerator optics model, beam-based measurement of the transfer matrix elements R_{11} and R_{12} is done before each slice emittance measurement. This section describes how the transfer matrix element R_{12} is calibrated using an optics response measurement with a corrector magnet High1.St1, which is located close to the slit mask EMSY1. In a second step, a thin-lens model is assumed to determine the focusing strength of the magnetic doublet used to focus the electron beam during slice emittance measurements. With the focusing strength known, the transfer matrix elements R_{11} and R_{12} from the slit mask to the observation screen is determined. Lastly, the difference between the analytic correction using the thin-lens model is compared with the transfer matrix elements derived from an ASTRA simulation, estimating a systematic error remaining after correction.
The beamline arrangement, used for the optics calibration, is sketched in Fig. 4.6. As the horizontal (slice) emittance is measured, only the transport matrix elements in the horizontal plane are of interest. Therefore, a horizontally deflecting corrector magnet is chosen for the optics response measurement. The magnet High1.St1 is chosen which is located 38 cm upstream the slit mask. In a first step, the deflection strength is of the corrector is calibrated. As the BPMs were not fully commissioned during the slice emittance measurements, the target screen PST.Scr1 was chosen for the corrector magnet calibration. During the corrector calibration all quadrupole magnets between the corrector magnet and the observation screen are degaussed. As the distance L between the steering magnet and the observation screen is well-known, the transfer matrix from the corrector to the screen is given by Eq. 2.1.4. Equation 2.1.3 allows to determine the deflection strength x' when both the transfer matrix and the beam position x_2 at a downstream position is known.
For the corrector calibration the beam position x_2 is monitored for different corrector currents I, as shown on the left side of Fig. 4.7. The slope of the linear fit is the change of beam position per change in corrector current $\mathrm{d}x_2/\,\mathrm{d}I$. Here, the steering magnet current has been scanned from 0.6 A to 1.6 A in five steps of 0.2 A. The error bars show the ten-times rms beam position, which was calculated by twenty measurements for each current. The corrector strength (for the beam momentum during the calibration) is then derived by dividing the slope $\mathrm{d}x_2/\,\mathrm{d}I$ by the drift length L. The corrector strength in the example is $-12.30\,\mathrm{mrad/A}$ for a beam momentum of $19.354\,\mathrm{MeV}/c$.
After the corrector strength is determined, two quadrupole magnets are set to reduce the horizontal beamlet size and to focus the beam in the vertical plane y. For this, the doublet High1.Q09 and High1.Q10 is chosen, as these two magnets are the magnets close to the TDS and upstream to it, see Fig. 4.3. The bunch trajectory is chosen such, that the quadrupole magnets have no net deflection due to an off-centre passage through the magnets. These are set in a way, that the magnet High1.Q09 is focusing in the horizontal plane, while High1.Q10 is defocusing in the horizontal plane. This allows for a smaller vertical beam size σ_y on the observation screen, which leads to a good time resolution. Strong focusing with $R_{12} \approx 0$ is not allowed in the horizontal plane, as for the case $R_{12} = 0\,\mathrm{m}$ the angular distribution does not contribute to the spatial distribution, i.e. the reconstruction becomes impossible. The optimum focusing strength is investigated in experiment and simulation in Ch. 5. Usually the R_{12} value in the horizontal plane is reduced by a factor of ~ 2 compared to the drift, i.e. $R_{12} \approx 3.5\,\mathrm{m}$.
For the optics-response measurement the corrector currents have been scanned in five steps between 0.6 A and 1.6 A while the beam position is observed. The quadrupole magnets

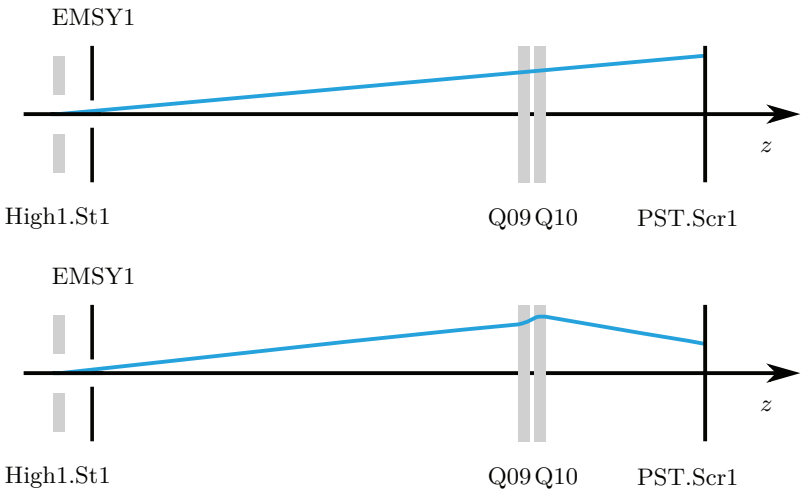

Figure 4.6: Sketch of the online transport matrix element calibration. The strength of the horizontal corrector magnet High1.St1 is determined by measuring the deflection of the beam on a downstream screen for different currents (top). In a second step the quadrupole magnets High1.Q09 and High1.Q10 are used to focus the beam in the vertical plane while reducing the beam size in the horizontal plane by roughly a factor of two. The horizontal beam position is measured with the optics applied for different corrector magnet deflection strength (bottom), which allows calculation of R_{12} in the horizontal plane.

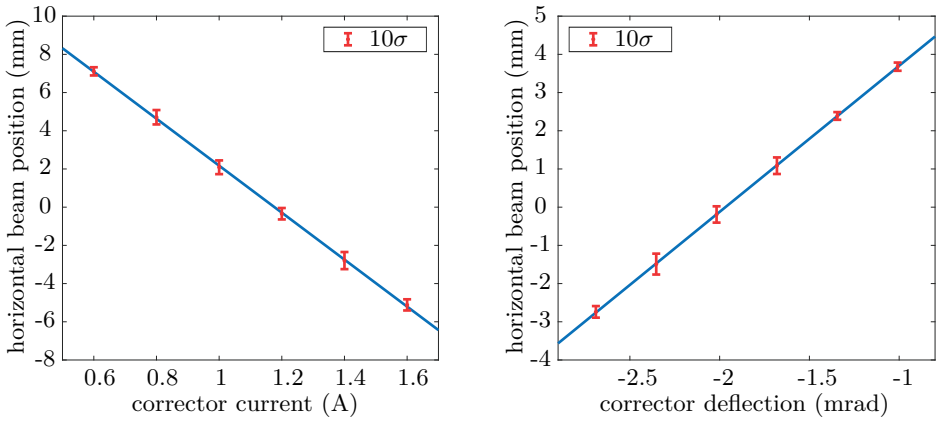

Figure 4.7: Example of the calibration of the horizontal corrector magnet High1.St1 (left) and the horizontal beam transport matrix element R_{12}^{*} from the centre of the corrector magnet to the screen PST.Scr1 (right), while the quadrupole magnets High1.Q09 and High1.Q10 were set for slice emittance measurements. The rms position uncertainty is below 45 µm. The error bars show ten σ for a better visibility. A typical rms beam size at PITZ is $x_{\mathrm{rms}} \sim 0.3\,\mathrm{mm}$.

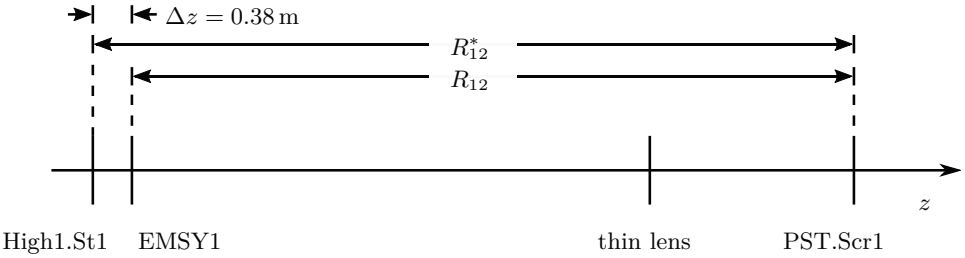

Figure 4.8: Thin-lens model assumed for the correction of the transfer matrix elements. The optics response measurement allows to measure the transfer matrix element R_{12}^* from the corrector magnet High1.St1 to the observation screen PST.Scr1. Of interest for the slice emittance reconstruction are the transfer matrix elements R_{11} and R_{12} from the slit mask EMSY1 to the observation screen. These are calculated from the measured element R_{12}^* by calculating the strength a thin lens, located centrally in the doublet would have. In a second step, the beam transport elements are determined, as the strength of the thin lens, and the length of the drifts before and behind the thin lens are known.

are set in the same manner as in the slice emittance measurement. With the previously determined corrector strength, this yields (absolute) deflections between $-2.7\,\mathrm{mrad}$ and $-1\,\mathrm{mrad}$ at the corrector magnet. As the corrector magnet High1.St1 is set to a non-zero value for beam trajectory adjustment the scanning range is not symmetrically around zero. The right plot in Fig. 4.7 shows the $R_{12,x}$ calibration. The linear slope of the horizontal beam position against the corrector deflection yields the beam transport matrix element R_{12} in the horizontal plane, from the centre of the corrector magnet, to the observation screen, according to Eq. 2.1.3. The beam position x_1 is neglected in this calculation, as the beam is not moving at the corrector magnet position, i.e. x_1 is constant. Therefore, the proportionality factor between angular deflection x_1' and beam position x_2 is given by R_{12}, the slope of the linear fit. In the example in Fig. 4.7 the beam transport matrix element is $R_{12}^* = 3.825\,\mathrm{m}$, see also Fig. 4.8.
However, for the reconstruction of the angular beam distribution at the slit mask, and hence the phase space, the transfer matrix element R_{12} from the slit mask to the screen has to be determined, as depicted in Fig. 4.8. To have a correction which is robust against deviations of the actual magnetic model from the theoretically predicted the correction is calculated assuming the simplest model, i.e. by assuming the optics model of a thin focusing lens of strength kl_q, located centrally between the two doublet quadrupole magnets. Therefore the transfer matrices of the first quadrupole magnet, the short drift between the first and the second quadrupole magnet, and the second quadrupole are substituted by the transfer matrix of a thin lens. Then the transfer matrix in the horizontal plane x from the centre of the corrector magnet to the observation screen is given by

$$\boldsymbol{R}_{\mathrm{Corrector}\to\mathrm{Screen}} = \boldsymbol{R}_{\mathrm{Drift}} \cdot \boldsymbol{R}_{\mathrm{Quad}} \cdot \boldsymbol{R}_{\mathrm{Drift}} \cdot \boldsymbol{R}_{\mathrm{Quad}} \cdot \boldsymbol{R}_{\mathrm{Drift}} \approx \tag{4.4.1}$$

$$\boldsymbol{R}_{\mathrm{Drift}} \cdot \boldsymbol{R}_{\mathrm{Lens}} \cdot \boldsymbol{R}_{\mathrm{Drift}} = \tag{4.4.2}$$

$$\begin{pmatrix} 1 & L_1 \\ 0 & 1 \end{pmatrix} \cdot \begin{pmatrix} 1 & 0 \\ -kl_\mathrm{q} & 1 \end{pmatrix} \cdot \begin{pmatrix} 1 & L_0 + \Delta z \\ 0 & 1 \end{pmatrix} = \tag{4.4.3}$$

$$\begin{pmatrix} 1 - kl_\mathrm{q} L_1 & L_0 + \Delta z + L_1 - kl_\mathrm{q} L_1 (L_0 + \Delta z) \\ -kl_\mathrm{q} & 1 - kl_\mathrm{q}(L_0 + \Delta z). \end{pmatrix} \tag{4.4.4}$$

Here, the distance between the centre of the steering magnet and the slit mask is given by $\Delta z = 38\,\mathrm{cm}$, the drift from the slit mask to the lens by $L_0 = 5.021\,\mathrm{m}$ and the drift from the lens to the observation screen by $L_1 = 1.98\,\mathrm{m}$. This yields the transfer matrix elements

$$R_{11} = 1 - kl_\mathrm{q} L_1 \tag{4.4.5}$$

and

$$R_{12} = L_0 + \Delta z + L_1 - kl_\mathrm{q} L_1 (L_0 + \Delta z). \tag{4.4.6}$$

Equation 4.4.6 is then solved for the focusing strength kl_q, yielding

$$kl_\mathrm{q} = \frac{\Delta z + L_0 + L_1 - R_{12}^*}{L_1 (L_0 + \Delta z)}, \tag{4.4.7}$$

where R_{12} was substituted by the calibrated R_{12}^* from the corrector magnet to the screen. Finally, the transfer elements R_{11} and R_{12} are calculated using Eq. 4.4.5 and Eq. 4.4.6 by setting $\Delta z = 0\,\mathrm{m}$ and using the focusing strength of the lens from Eq. 4.4.7. This yields

$$R_{11} = 1 - kl_\mathrm{q} L_1 = 1 - \frac{\Delta z + L_0 + L_1 - R_{12}^*}{L_0 + \Delta z} \tag{4.4.8}$$

and

$$R_{12} = L_0 + L_1 - kl_\mathrm{q} L_0 L_1 = L_0 + L_1 + \frac{L_0}{L_0 + \Delta z} \left(R_{12}^* - \Delta z - L_0 - L_1 \right). \tag{4.4.9}$$

The thin-lens model, together with the optics response measurement, allows to determine the transfer matrix elements reliably. However, systematic errors in the R_{11} and R_{12} calculation might arise from the choice of the model, despite the fact that the quadrupole magnets High1.Q09 and High1.Q10 are very close, see Fig. 4.6 and Appendix A.
The systematic error is estimated in an ASTRA (a space charge tracking algorithm) simulation [41]. Here the transfer matrix elements R_{11} and R_{12} are calculated both from the corrector magnet and the slit mask to the observation screen for varying focusing strength, see Fig. 4.8. The (simulated) transfer matrix elements from the slit station are compared with the calculated transfer matrix elements, calculated according to Eq. 4.4.8 and Eq. 4.4.9.
For this a particle distribution is created at the centre of the corrector magnet. This is done by simulating the beam transport from the emission of macro particles at the photocathode to the corrector. The particle bunch is then tracked further, where the whole distribution is saved at the position of the slit mask, as well as at the observation screen. The tracking to the observation screen is done several times, each with a different doublet focusing strength applied. Space charge forces are neglected in the simulation. Now each macro particle has a position x and an angle x' which is saved at the corrector magnet, the slit mask, and at the observation screen. As the position and angle of each macro particle at a start position, as well as the final position is known, the transfer matrix elements R_{11} and R_{12} can be determined by fitting these to the initial particle coordinates according to Eq. 2.1.3 via

$$x_2 = R_{11} x_1 + R_{12} x_1'. \tag{4.4.10}$$

In this tracking simulation 1000 macro particles are used, while two macro particles are sufficient to determine both transfer matrix elements R_{11} and R_{12} between the two positions 1 and 2.
When the macro particle distribution at the corrector magnet is considered for the fit the retrieved transfer matrix element R_{12} is the simulation equivalent to the measured value R_{12}^* from the centre of the corrector magnet to the observation screen PST.Scr1, see

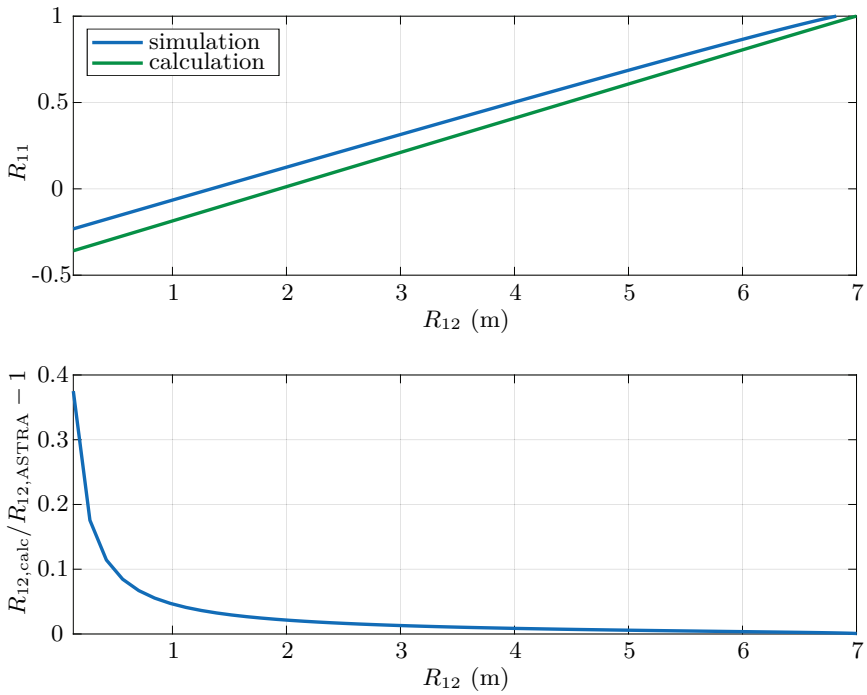

Figure 4.9: Comparison of calculated and simulated matrix transfer elements. The absolute difference between calculated R_{11} value from the slit station to the observation screen and the R_{11} value determined from simulation versus the simulated matrix transfer element R_{12} from the slit station to the screen is shown on top. The maximal difference for R_{11} values between 3.5 m and 5 m is 0.15, while $R_{11} = 1$ for a pure drift space. The relative difference of the calculated and simulated transfer matrix element R_{12} remains below $\sim 4\,\%$ for all focusing strength $1\,\mathrm{m} \leq R_{12} \leq 7\,\mathrm{m}$. Only at stronger focusing strength, i.e. $R_{12} < 1\,\mathrm{m}$, the error increases. This region however is excluded from the usable parameter space due to the worsening angular resolution.

Fig. 4.8. Correspondingly, when the distribution at the slit mask is considered as starting point, the transfer matrix elements $R_{11,\mathrm{Astra}}$ and $R_{12,\mathrm{Astra}}$ correspond to the elements needed for the slice phase space reconstruction. These are compared to the transfer matrix elements $R_{11,\mathrm{calc}}$ and $R_{12,\mathrm{calc}}$, which are obtained from Eq. 4.4.8 and Eq. 4.4.9, while using the R_{12} from the corrector to the screen as input for R_{12}^{*}.

The tracking from the slit mask to the observation screen are done for different focusing strengths of the magnets High1.Q09 and High1.Q10 in order to investigate whether the transport matrix elements are calculated correctly for different focusing strength. The result is shown in Fig. 4.9. The top plot shows the absolute difference between the calculated and simulated matrix element R_{11}. For a pure drift space, i.e. $R_{12} = 7\,\mathrm{m}$ a very small difference between simulated and calculated R_{11} value exists, which increases slightly towards tighter focusing, i.e. smaller R_{12} values. The lower part of Fig. 4.9 shows the relative difference between the calculated $R_{12,\mathrm{calc}}$ value and the simulated $R_{12,\mathrm{Astra}}$. For R_{12} values between 7 m and 2.5 m the relative difference does not raise above 1 %. For even smaller R_{12}'s the relative error rises to ~4 % at 1 m, before it sharply increases for even stronger focusing. The systematic error in the calculation of R_{11} and R_{12} have different effects on the reconstruction of the angular distribution and the phase space. An erroneous transfer

matrix element R_{12} translates directly into an erroneous (slice) emittance, as the emittance is proportional to the angular spread, see Eq. 2.2.10, while the angular spread is proportional to R_{12}, see Eq. 4.3.4.
An error in the beam transfer matrix element R_{11} however does not translate into any error of the (slice) emittance, as R_{11} is not used to reconstruct the angular beamlet distribution at each slit position, nor the spatial beam distribution from the intensities of the beamlets. However, the transfer matrix element R_{11} is used to consider the net angle the beamlets have for each slit position, thus affecting the correlation term(s) $\langle xx' \rangle$, and therefore also the calculation of the alpha function and the mismatch parameter.
The calibration of the horizontal transfer matrix elements R_{11} and R_{12} allows for reliable slice emittance measurements, as discrepancies between the theoretical optics model and the actually applied beam optics do not spoil the measurements. Errors in how the quadrupole magnets are set, e.g. due to an erroneous power supply, or the corrector magnet strength are excluded due to the calibration of the optics and the corrector magnet. An error in wrong screen calibration also does not contribute to this values, as the same observation screen is used for both the corrector magnet and beam optics calibration, so that any error cancels.

4.5 Image Analysis

Detection of transverse beam distributions is fundamental for emittance measurements. A correct reconstruction of the beam momenta requires reliable measurements of the rms beam size for rms emittance calculation. Since the rms values are sensitive to noise, a proper image analysis has to be done. During slit-based slice emittance measurements the bunch charge is reduced by the slit mask. In addition, the rf deflection further reduces the signal density on the beamlet measurement screen. Besides the beam signal camera noise, dark current contributions and screen features line non-uniformities and scratches are included in the final beam image, which might spoil the slice phase space reconstruction as shown in Fig. 4.5. A camera image of a beam, measured at the screen station PST.Scr1, after it was deflected by the TDS, is given in Fig. 4.10. These issues impose stringent requirements on the image analysis. For the measurement of the projected emittance a noise cut has already been developed. However, first slice emittance measurements[1] showed, that this noise cut is too aggressive and underestimates the beam sizes. Thus, a less aggressive noise cut was developed for the slice emittance measurements.

The presented filtering algorithm was mainly developed by B. Beutner and H. Huck especially for time-resolved emittance measurements [90]. It proceeds the images without fitting routines. The algorithm especially allows to keep several unconnected groups of pixel containing signal. This is a very important option for the use at PITZ due to its vast pulse shaping possibilities.
An example of the image analysis procedure for an image, obtained during a slit-based slice emittance measurement is given in Fig. 4.11. At first the ten-times averaged background image is subtracted from the raw image. Here, the background is defined as the image the camera takes while the laser beam shutter is closed. Dark current contribution might still be included in background images, which makes it possible to subtract them. In a second step a manual area-of-interest is applied to cut out image areas with high intensity which

[1] During the first slice emittance measurements, no quadrupole magnets behind the slit mask have been used, which resulted in a small signal strength. Also, high sensitivity LYSO screens were not available.

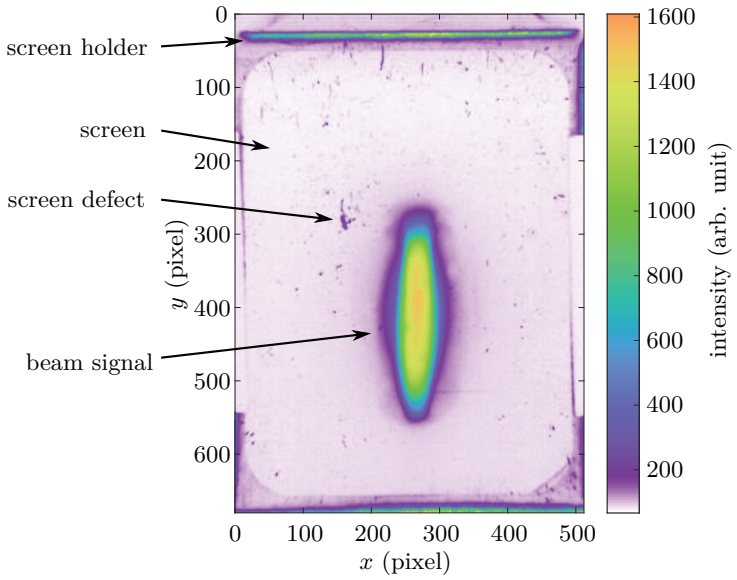

Figure 4.10: Ten-times averaged camera image of a vertically deflected electron beam, taken at the screen station PST.Scr1. Besides the deflected beam, also the screen holder, in particular strong light reflections on the screen holder, as well as scratches on the screen are visible.

do not arise from beam signal, i.e. the screen edge. The obtained distribution is smoothed with a Gaussian function

$$f(x,y) = \frac{1}{2\pi\sigma^2_{\text{smooth}}} \exp\left(\frac{-\left(x^2+y^2\right)}{2\sigma^2_{\text{smooth}}}\right) \tag{4.5.1}$$

which is applied to every pixel of the image, i.e. every pixel value is locally smoothed with its surrounding pixel values. The rms width σ_{smooth} of the smoothing distribution remains as free parameter and has to be set.
Next the mask-of-interest (MOI) is generated. The MOI is a boolean map, which either discards an area of an image, or contains it, so it is then considered for calculation of an image property. For a reliable phase space reconstruction all areas of the image containing beam signal have to lay inside the MOI, while all non-beam related contributions have to be rejected from the MOI. The beamlet image can consists of several pieces, which are spatially separated on the screen. These *satellites* or *islands* have to be all kept in the MOI to not underestimate the emittance. As up to 2 islands can occur in beam images during slice emittance measurements with a single slit the *number of islands* (noi) is set to $n_{\text{noi}} = 2$.
For the calculation of the MOI all pixels with fillings bigger than $n_{\text{bkg}} \cdot \sigma_{\text{bkg}}(x,y)$ are kept, where $\sigma_{\text{bkg}}(x,y)$ is the pixel-wise rms intensity jitter of the background images and n_{bkg} a scaling parameter. The islands are sorted according to their highest pixel intensity. Since the image has already been smoothed, the highest pixel value corresponds to signal and not to intensity jitter. Only the $n_{\text{noi}} = 2$ number of islands with the highest intensity are kept in the MOI, the remaining islands are discarded. The discarded satellites are usually caused by minor scratches of the scintillator screen, which glow when the electron beam hits the screen, see screen defect in Fig. 4.10.
The final MOI is applied to the image after background subtraction, all values outside the MOI are set to zero. Inside the MOI the pixel values are kept as they were in the filtered

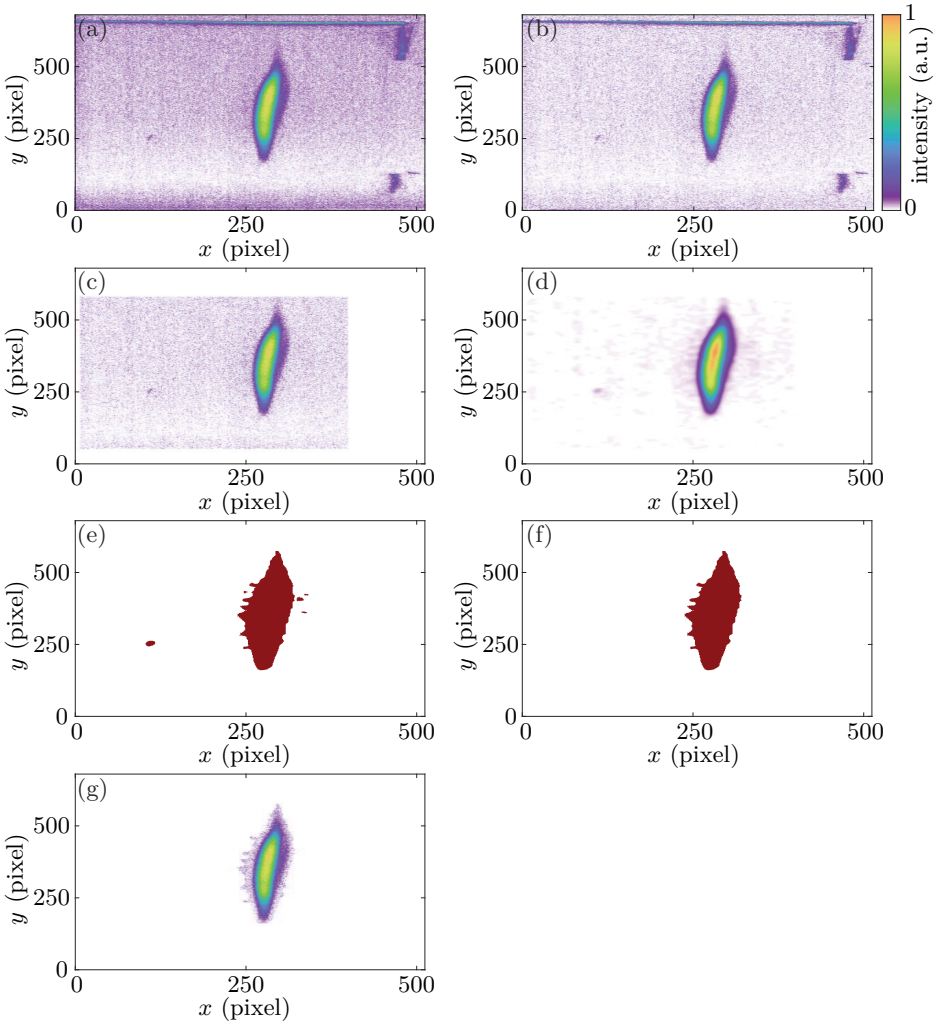

Figure 4.11: Steps of the noise cut algorithm. It shows an image taken during measurement of the time-resolved emittance with the slit method. Image (a) shows the raw image, (b) after ten-times-averaged background subtraction, (c) after an area-of-interest has been applied (manually by the operator), (d) after smoothing, (e) shows the pixel above threshold, (f) only the n_{noi} (here $n_{\mathrm{noi}} = 1$) group of pixel with the highest filling and (g) the image, after (f) has been applied to (c) and the mean pixel filling outside the mask-of-interest (MOI) has been subtracted inside the MOI. The colour scale was kept between 0 and the maximum value in each image, even for the images with negative pixel filling, i.e. (b), (c), (d) and (g).

image in (b), e.g. negative pixel values are kept as well. The images might still include an unwanted contribution from the electron beam. Since the electrons are not stopped at the slit mask but scattered, they travel further downstream the accelerator, with some eventually causing the screen to scintillate. To correct for this the averaged pixel filling outside the MOI is subtracted from the remaining pixel to obtain the final signal image to correct for an overall light intensity on the camera which cannot be subtracted with the background subtraction.
Drawback of this method are the two parameter n_{bkg} and n_{noi}, which have to be set externally. A proper choice of these parameters requires a calibration. Also, measurement results are only comparable if the parameters are the same. For all slice emittance measurements presented in this thesis, the parameters were set to $n_{\mathrm{bkg}} = 1.5$ and $n_{\mathrm{noi}} = 2$. The standard tool for projected emittance measurements uses a noise cut with $n_{\mathrm{bkg}} = 3$.

4.6 Emittance Underestimation Analysis via Intensity Cuts

Correct reconstruction of the emittance makes consistent detection of the beamlet images crucial. However, the images taken during the measurement are subjected to noise. The noise is included in the whole images, creating a *noise floor*, on which the beam signal is located. Due to the noise in the taken images the signal-to-noise ratio (SNR) remains finite, which in turn means that some regions of the beamlet have an intensity comparable to the image noise level, making it impossible to detect the full signal. Therefore, not the 100 % rms emittance is measured, but a lower fraction, yielding a smaller emittance. In order to evaluate the emittance underestimation the emittance is reconstructed, after an intensity cut is applied. This will once be done in the slice phase space directly and another time in the beamlet images created from the simulation of the measurement.
For this, the generation and transport of electrons with injector settings typical at PITZ is simulated from the cathode to the measurement station EMSY1. This is done with the ASTRA code [41]. The photocathode laser pulse has a Gaussian temporal shape with a FWHM pulse length of 6 ps and a transversely uniform shape. The beam properties are listed in Table 4.1. The bunch charge and momentum after the gun corresponds to the routine settings at the European XFEL [91].

In the start-to-end simulation, the transverse laser pulse width, as well as the main

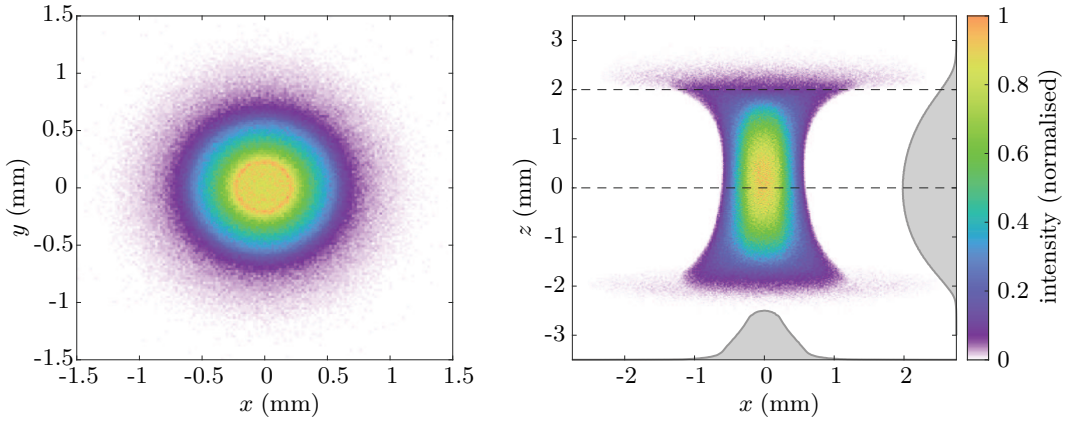

Figure 4.12: Real space images of the simulated electron beam at the slit position EMSY1. It was optimised for minimal projected emittance. A projected emittance of $\epsilon_x = 0.61\,\mu\mathrm{m}$ was simulated. The x-z-plane (right) shows, that the head and tail contain the outermost particles. The slice phase space at the dotted lines is shown in Fig. 4.13.

Table 4.1: Settings of the ASTRA start-to-end simulation of the PITZ-typical beam, emitted from a laser pulse with temporal Gaussian and transversely flattop shape. The electric field in the gun cavity and booster cavity are set to achieve the listed momenta. The main solenoid current and transverse flattop beam size on the cathode are set to the point yielding minimal projected emittance at the slit position EMSY1. The resulting emittance and beam size are listed in the second part of the table.

Beam property		unit	value
Number of macro particles			$2 \cdot 10^6$
Bunch charge	Q	pC	250
Laser spot diameter on cathode	σ_x	mm	1.3
Temporal laser pulse length	t_{FWHM}	ps	6
Thermal emittance	ϵ_{th}	µm	0.28
Main solenoid current	I_{main}	A	366
Momentum after gun cavity	p_{Gun}	MeV/c	6.32
Momentum after booster cavity	p_{Boo}	MeV/c	19.29
Beam size at EMSY1	σ_x	mm	0.37
Projected emittance at EMSY1	ϵ_x	µm	0.61

solenoid magnet strength are optimised for minimal projected emittance at the slit mask. The minimum was found at a solenoid current of $I_{\mathrm{main}} = 366\,\mathrm{A}$ and a laser pulse diameter of 1.3 mm.

The real space image of the optimised beam at the slit mask, i.e. at 5.28 m (downstream the photocathode surface) is given in Fig. 4.12. The image shows, that the beam distribution is close to a two-dimensional Gaussian shape in the x-y-plane.

The picture of the x-z-plane shows that the temporal core of the beam is well-focussed, while the head and tail of the beam are mismatched with the core. The outermost particles are scattered to almost $\pm 2.5\,\mathrm{mm}$ in the horizontal plane x. This is the result of the mismatch between space charge forces and solenoid focusing due to much weaker charge density at beam head and tails. The tail and centre slice phase space of this distribution is given in Fig. 4.13.

To estimate the emittance underestimation the slit scan is simulated with a beam transport to PST.Scr1. To emulate the slit scan a planar collimator is included in the simulation. The width of the collimator is selected to be the same as the slit opening at the EMSY1 station, i.e. 50 µm. The simulation is then carried out several times, where the transverse position of the planar collimator is shifted, which is the simulation equivalent of different slit positions. As the large fraction of macro particles is lost at the slit mask, the simulation is carried out with $2 \cdot 10^6$ particles, while usually $2 \cdot 10^5$ particles are considered for ASTRA simulations, in which e.g. the projected emittance is optimised. Special care has also be taken to take small iteration steps near the slit mask, so that the macro particles get lost at the collimator and do not move through it in simulation.

As in the actual experiment, the quadrupole magnets High1.Q09 and High1.Q10 are set to achieve an R_{12} value of 3.52 m from the slit mask to the observation screen. To yield a good time resolution the rf deflector is set to an effective voltage of 1.7 MV, which is the design deflection voltage of the TDS at PITZ. The beamlets are tracked from the slit position EMSY1 to the observation screen PST.Scr1, located 12.28 m downstream the cathode surface plane.

The beamlet images are constructed by creating a histogram from the tracked macro

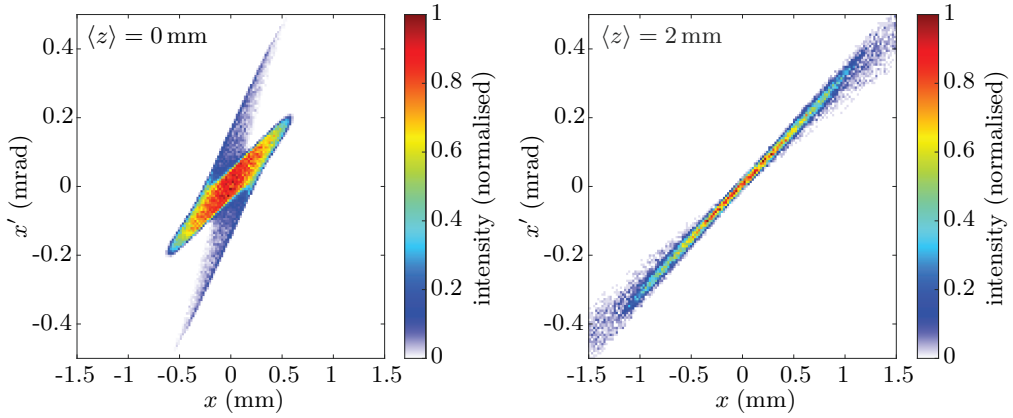

Figure 4.13: Centre slice phase space of the temporal Gaussian laser beam $\langle z \rangle = 0\,\mathrm{mm}$ (left), and slice phase space of the temporal Gaussian distribution, located at $\langle z \rangle = 2.0\,\mathrm{mm}$ (right). Both slices have a thickness of 0.2 mm. The colour map are normalised individually to the maximal density in each slice individually.

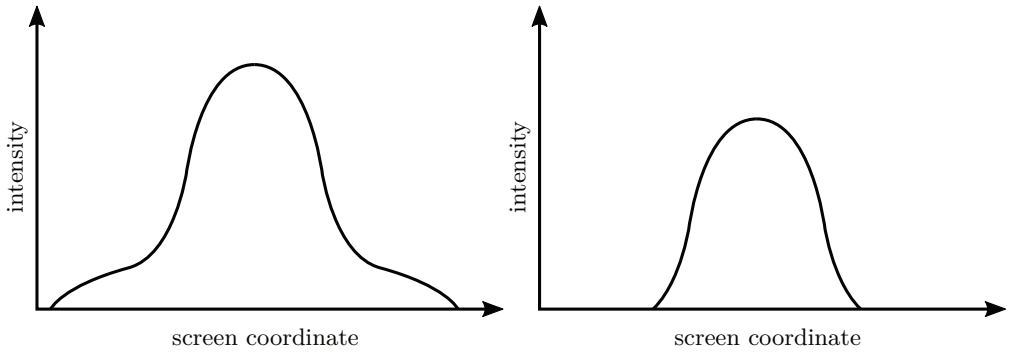

Figure 4.14: Scheme of the intensity cut. All pixel values are reduced by a certain intensity, negative pixel values are set to zero. Note that the scheme shows a cut through the beamlet and no projection.

particles. The simulated beamlet images undergo an intensity cut as depicted in Fig. 4.14: All pixel values for all beamlet images are reduced by a fixed intensity level, i.e. by

$$\text{reduction} = \text{intensity cut amplitude} \cdot q_{\max}, \tag{4.6.1}$$

where $q_{\max}$ is the maximum beamlet charge density. In a second step, all negative pixel values are set to zero, creating intensity-cut beamlet images. However, due to the loss of particles at the slit mask and the vertical deflection only few integer intensity levels exist in the beamlet images, making it impossible to resolve may different signal-to-noise ratios. To overcome this issue the beamlet images are smoothed with a 2d-Gaussian function. This creates non-integer pixel values, allowing to assume any SNR, while not changing the emittance values significantly.
After the intensity cut the slice phase space is reconstructed with the intensity-cut beamlet images, before the projected and slice emittance are reconstructed. To make an objective comparison the emittance values are divided by the emittance when no intensity cut is

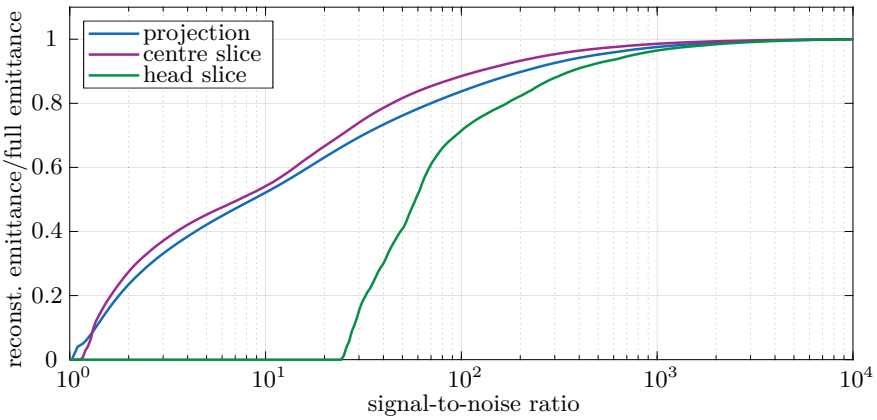

Figure 4.15: Emittance reconstructed after intensity cut over full emittance for different signal-to-noise ratios. The intensity cuts are applied in the simulated beamlet images themselves. The curves are given for the projected emittance (blue), the centre slice (purple) and the head slice (green).

done. Figure 4.15 shows this fraction for the projected emittance, the head slice emittance, and the centre slice emittance. The SNR is derived from the intensity cut via

$$\mathrm{SNR} = \frac{1}{\text{intensity cut amplitude}}, \tag{4.6.2}$$

where no intensity cut describes the zero noise case, i.e. the SNR is infinity, while an intensity cut amplitude of 1.0 describes the case where the signal amplitude is as big as the noise level, making it impossible to distinguish the signal from noise, and leading to an empty beamlet image.
The plot of Fig. 4.15 shows that for SNRs around 10^3 the emittance is underestimated by less than 5 %. For even higher SNRs this deviation decreases further as the emittance fractions converge to 1. When the SNR decreases below 10^3 the deviation is larger. The head and tail slices are most sensitive, as the temporal Gaussian beam profile has only low signal strength in the tails. At a SNR of 100 the shown head slice measures only 70 % of the actual slice emittance. The centre slice and the projected phase space have also an underestimated emittance, but only by 12 % and 16 %, respectively. The plot also shows, that the projected emittance is slightly more sensitive to noise than the centre slice emittance. This is due to the fact, that the projected emittance is calculated from the projection of all beamlet images. The projections contain both the centre slices with a high charge density and thus a high signal strength, as well as the tails, which have only a low charge density. Therefore, the projected emittance is slightly more sensitive to emittance underestimation than the centre slices. However, the difference is very small over the whole range of SNRs, so that it can be assumed both have the same dependence.
The reconstructed slice emittance curves, for selected SNRs, are depicted in Fig. 4.16. It shows that the reconstructed slice emittance is underestimated due to noise. The shape of the reconstructed slice emittance curve can differ significantly from the slice emittance curve, calculated from the macro particle distribution at the slit position (actual slice emittance curve). This method used intensity cuts in the beamlet images. The advantage of this method to estimate the emittance underestimation due to finite SNR requires only few prerequisites. Here, a start-to-end simulation is done to generate a macro particle distribution representing the actual electron beam. The simulation settings were optimised for minimal projected emittance using a transverse flattop beam, from a temporal Gaussian laser pulse profile. This is similar to the experimental optimising steps. Then, the slit

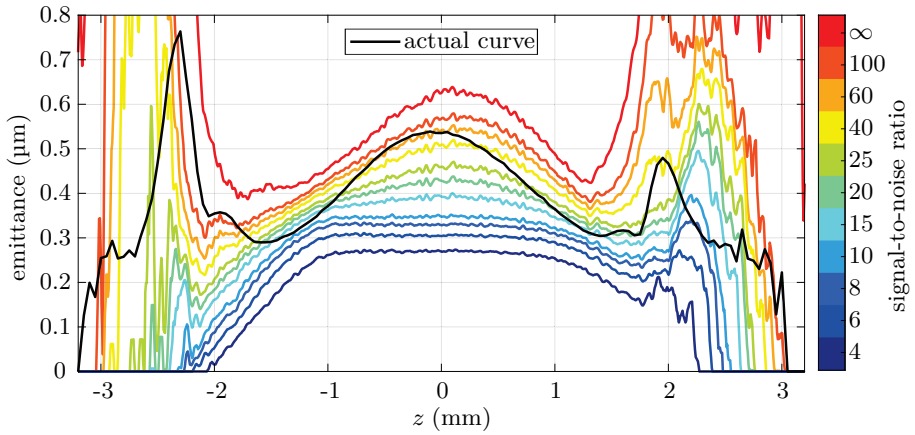

Figure 4.16: Reconstructed slice emittance curves at different signal-to-noise ratios. Here, space charge forces were considered in the beam transport, the focusing was set to a beam transfer matrix element of $R_{12} = 3.5\,\mathrm{m}$ and a TDS deflection voltage of 1.7 MV. The intensity cuts were applied in the beamlet images, before the emittance was reconstructed. The 100 % projected rms emittance is 0.61 µm, see Table 4.1. The slice emittance curve, calculated from the macro particle distribution at the slit position EMSY1 (actual curve) is given in black.

scan slice emittance measurement setup is simulated using the beam. This is quite time consuming when space charge forces are included in the simulations, as the beam transport has to be done for each slit position individually, i.e. ~ 100 times. Also, the number of macro particles has to be higher to ensure a decent sampling of the beamlet images: The slit mask removes most of the macro particles, in the drift the number further reduces, before they are sorted into a histogram, describing the beam profile measurement with a camera. Alternatively, the macro particles are tracked to the slit mask. Here, the time-resolved phase space is reconstructed. A TDS voltage of 1.7 MV was assumed in simulation. Then the intensity cuts, as shown in Fig. 4.14, are done directly in the phase space. The emittance fraction for different SNRs is shown in Fig. 4.17. As the directly reconstructed phase space has a higher density, no smoothing has been applied. Both the curves of the projected and centre slice emittance show similarity with the curves from Fig. 4.15, therefore, the emittance underestimation can be easily checked for the centre part of the bunch and the projection with an intensity cut in the slice phase space. For the head slice however a bigger deviation is observed.
The circumstance, that the slice emittance changes quicker for some slices and slower for other, leads to the fact that the emittance underestimation cannot be described by a global factor for all slices, nor for different electron beams. The emittance underestimation can be roughly estimated by the shown emittance reduction, but different electron beams might be even more, or also less sensitive to a finite SNR.
Since the reconstructed emittance changes faster for some slices and slower for others, the slice emittance curve is altered. The slice emittance curve of a temporal Gaussian beam can be seen in Fig. 4.18. The red curve shows the slice emittance from the phase space, when no intensity cut is applied, i.e. 100 % of the particles are considered. In this case the SNR is infinity. For higher intensity cuts, i.e. lower SNRs the curves decrease, as described in Fig. 4.15 and Fig. 4.17. The high slice emittance around $z = -2\,\mathrm{mm}$ and 2.2 mm is characteristic for electron beams from temporal Gaussian laser pulses. These peaks in slice emittance curve however first decrease and then fully disappear due to the finite SNR. This

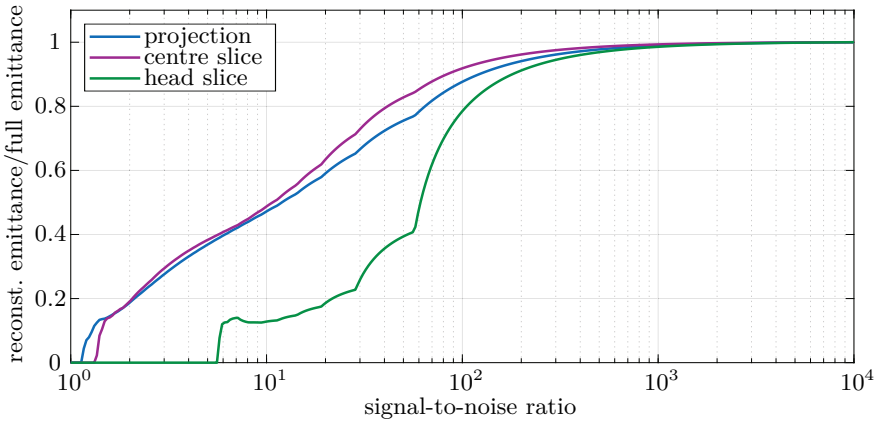

Figure 4.17: Emittance reconstructed after intensity cut over full emittance for different signal-to-noise ratios. The intensity cuts are applied in the slice phase space, reconstructed from the macro particle distribution at the slit mask. The curves are given for the projected emittance (blue), the centre slice (purple) and the head slice (green).

allows to judge on the achieved SNR, based on the shape of the measured slice emittance curve.

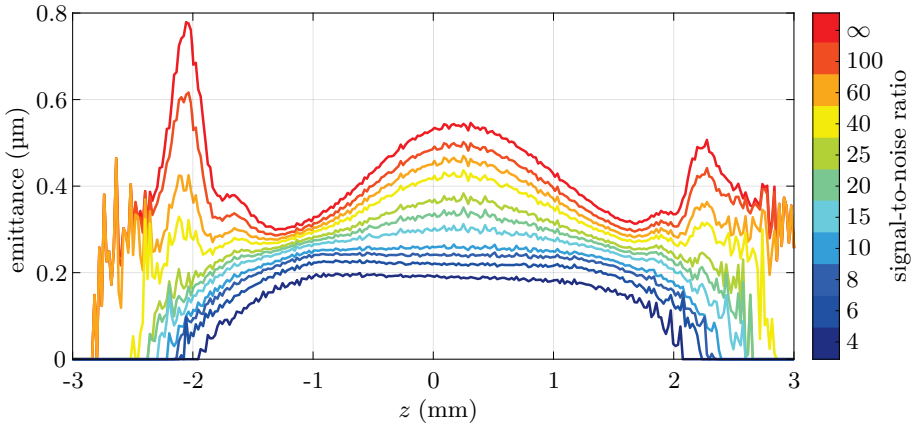

Figure 4.18: Simulated slice emittance curves, after intensity cuts constituting different SNRs have been applied in the slice phase space. The electron bunch has a temporal Gaussian shape at the emission and was tracked to the slit station. The smaller the SNR, the smaller the slice emittance and the smaller the total reconstructed bunch length. The intensity cuts were applied in the slice phase space after it was reconstructed from the macro particle distribution at the slit position.

5 Error Analysis

In order to evaluate the reliability of any beam diagnostics the sources of systematic errors have to be investigated, as they might limit the measurement accuracy and reliability. For the slice emittance diagnostics at PITZ, possible sources of a systematic error are

- an overestimation of the angular spread due to the contribution of the slit width to the beamlet size,
- an underestimation of the angular spread due to the finite thickness of the slit mask, leading to loss of particles with large angles,
- an increase of the beamlet width due to space charge forces,
- an overestimation of the emittance due to poor spatial and angular resolution of the phase space,
- an underestimation of the phase space volume due to low signal-to-noise ratio (SNR),
- a miscalculation of the angular spread due to the beam dynamics in the transverse deflecting structure and the accelerator optics,
- a faulty beam momentum measurement,
- machine jitter, and
- imperfections of the observation screen and TV system.

The impact of spatial and angular resolution is inspected in Sec. 5.1 by calculating the projected emittance with varying resolution. For this, the macro particle distribution, described in Table 4.1 is binned using different spatial and angular bin width. Simulation of the slit scan experiment allows to determine influences from space charge forces, slit width, drift length, focusing strength and TDS deflection voltages. This is done in the Sec. 5.2. The calculation of the statistical uncertainty is outlined in Sec. 5.3, before Sec. 5.4 and Sec. 5.5 cover measurements of slice emittance using different focusing strength and TDS deflection voltages, respectively. Influences from the finite SNR was already analysed using simulation in Sec. 4.6.

5.1 Measurement Resolution

First, the influence of the measurement resolution is investigated. For this, the phase space of the electron beam distribution is reconstructed with varying spatial and angular resolving power. The result from the start-to-end simulation described in Ch. 4 is used. The spatial resolution of the phase space is determined by the slit width and slit scan step size. For slice emittance measurements usually the step size is chosen to be the same as the slit width, i.e. 50 µm. When the beam size is very large a larger spacing of slit positions is selected proportionally to limit the data size and measurement time.
The angular resolution $\Delta x'$ of the measurements depends on the matrix transfer element

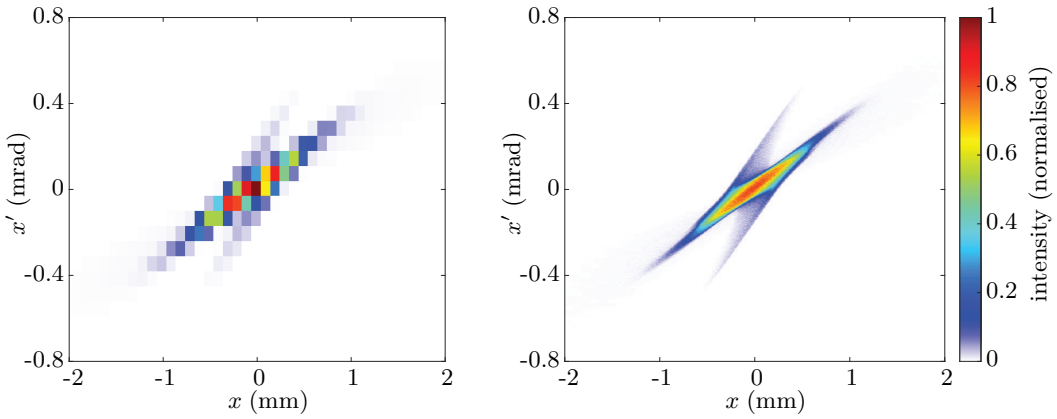

Figure 5.1: Projected phase space at EMSY1 with different resolutions. The left image has a spatial resolution of 100 µm and an angular resolution of 70 µrad, while the right phase space has a resolution of 10 µm and 1 µrad, respectively. The calculated, normalised emittance is 0.68 µm for the case of poor resolution, while being 0.61 µm for the well-resolved phase space.

R_{12} from the slit mask to the observation screen, as well as the spatial resolution Δx_{screen} of the screen station. It is given by

$$\Delta x' = \frac{\Delta x_{\text{screen}}}{R_{12}}. \tag{5.1.1}$$

Thus, a limit for the focusing of the quadrupole magnets is imposed: while a stronger focusing strength, i.e. a smaller matrix transfer element R_{12} reduces the systematic error from low signal strength, a small R_{12} increases the reconstructed emittance due to the poor angular resolution. This effect is observed in the measurement and is shown in Fig. 5.14. An emittance resolution can easily be calculated by multiplying the spatial and angular resolution:

$$\Delta\epsilon_{\text{n}} = \beta\gamma\Delta x\Delta x'. \tag{5.1.2}$$

This equation is derived from Eq. 2.2.14. As the correlation term $\langle xx' \rangle$ is determined with the same technique as the beam size and the divergence their resolution is the same. Therefore only the first term has to be considered. Since the resolution is always positive, the square root cancels with the square of the beam size and divergence. The normalisation of the emittance is considered by the factor $\beta\gamma$, just as in Eq. 2.2.14. Both the spatial and angular resolution should be sufficient to measure the rms size of the beam and the non-correlated rms divergence of the beam individually.
The lower limit for the resolution of the screen station is given by the size of the pixels on the camera chip, as well as the magnification factor of the screen image onto the camera chip. In the PITZ case the lower resolution limit is given by the camera calibration factor 0.046 mm/pixel, when the camera is operated in (2×2)-binning mode[1].
The phase space is reconstructed from the simulated macro particle distribution at the slit position using different bin width for the digitisation. The spatial resolution of the reconstructed phase space is changed between 10 µm and 100 µm, while the angular resolution is sampled from 0.001 mrad and 0.07 mrad. The phase spaces with the worst resolution, as well as the best resolution are shown in Fig. 5.1. While from the well-resolved phase space

[1] The screen-to-camera calibration factor can slightly change when the camera optics is realigned. The calibration factor of 0.046 mm/pixel was achieved for the PST.Scr1 (bottom) station at PITZ in January 2020.

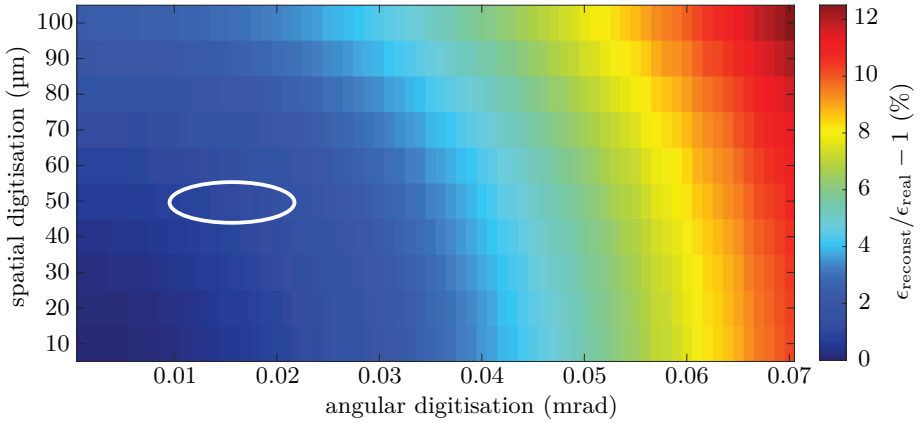

Figure 5.2: Systematic error in emittance calculation arising from phase space digitisation. It was calculated by reconstructing the projected phase space from the macro particle distribution using different bin widths and comparing the result with the actual projected emittance. The best resolution is given in the bottom left corner. There, the error in the emittance calculation is negligible. However, it rises up to 12.5 % when the spatial peak-to-peak resolution is 100 µm, while the angular peak-to-peak resolution is 0.07 mrad. The white ellipse show the digitisation which is usually achieved at PITZ.

a normalised projected emittance of 0.61 µm is calculated, the normalised emittance of the poorly resolved phase space is 0.68 µm, i.e. 12.5 % higher.
Figure 5.2 shows how the systematic reconstruction error changes with a varying measurement resolution. In the bottom left corner the error vanishes, i.e. the resolution is excellent. For both increasing spatial and angular digitisation the relative error increases.
The digitisation gives the limitation for the resolution. This applies for the experiment, in which the camera is used to measure the beam signal, as well as in following simulations of the experiment, where a macro particle distribution is sorted into a histogram for the emittance calculation. In experiment however additional influences which worsen the resolution have to be taken into account: The resolution of the screen station $\Delta x_{\mathrm{screen}}$ is influenced by the resolution of the scintillation screen itself, the size of the camera pixel, the magnification between the screen image and the camera chip, the orientation of the screen w.r.t. the electron beam, the observation angle, as well as the resolution of the imaging optics itself, given by the point spread function (PSF) of the camera setup.
At the screen station PST.Scr1 a minimal rms beam size of 55 µm has been measured, which provides the rms resolution of this screen station. According to Eq. 5.1.1 this yields an angular resolution $\Delta x' = 15.7\,\mu\mathrm{rad}$ for a transfer matrix element of $R_{12} = 3.5\,\mathrm{m}$. A typical beam size at PITZ is $\sigma_x = 0.2\,\mathrm{mm}$. Equation 5.1.2 yields $\Delta\epsilon_{\mathrm{n}} = 0.13\,\mu\mathrm{m}$ for a normalisation factor of $\beta\gamma = 40$. This is the smallest emittance which can be measured for the given parameters. The resolution is sufficiently low to measure the slice emittance at PITZ.

5.2 Beam Dynamics during Slit Scans

After the influence of the measurement resolution is analysed, the dependence of the emittance reconstruction on the beam dynamics behind the slit mask is analysed. Firstly, the systematic error arising from both the finite slit width, as described in Eq. 2.9.1, and from the space charge forces in the beamlet are investigated in ASTRA simulations [41].

This is done for projected emittance at first. Later also focusing quadrupole magnets and the TDS are added into the simulation. With the TDS included, the error on slice emittance measurements is derived as well.

5.2.1 Slit Scan with Drift Space without Transverse Deflection

To simulate the slit scan measurement for projected emittance, a collimating aperture with 1 mm thickness is included in the simulation, emulating the slit mask. The position of the aperture opening is shifted in steps of 50 µm, as it is done in the real experiment. The macro particles, which pass the aperture opening are tracked farther downstream. The distribution of macro particles is analysed by calculating the histogram of the distribution with the same resolution as the observation screen PST.Scr1 at the PITZ beamline. When the histogram is calculated after different distances behind the slit the simulation of different drift length after the slit becomes possible.
The simulation is carried out for both slit widths of 10 µm and 50 µm twice, once including space charge fields and once without space charge forces after passage through the aperture, i.e. four different cases, while the slit position is scanned between −2.4 mm and 2.4 mm.
The reconstructed emittance over the true emittance at the slit mask versus the drift length is depicted in Fig. 5.3. The plot shows, that the reconstructed emittance is very large when the drift length is below 1 m. Due to the short drift length the slit width contributes significantly to the beamlet width, leading to an overestimation of the angular spread, and thus, to the emittance. This can be estimated as well with an analytical calculation: The 50 µm-wide slit leads to an rms beam size of

$$\sigma_x = \frac{\Delta x_{\mathrm{FWHM}}}{\sqrt{12}} = 14.4\,\mu\mathrm{m}. \tag{5.2.1}$$

After a drift length of 1 m this is interpreted as a divergence of

$$\sigma_{x'} = \frac{\sigma_x}{L} = 14.4\,\mu\mathrm{rad}. \tag{5.2.2}$$

On the other hand, a beam with a momentum of $p = 19.29\,\mathrm{MeV}/c$ and a normalised emittance of 0.61 µm corresponds to a geometric emittance of 16.2 nm. Assuming an uncorrelated phase space, the divergence of this beam is

$$\sigma_{x'} = \frac{\epsilon_{\mathrm{geo}}}{\sigma_x} = 43.7\,\mu\mathrm{rad}, \tag{5.2.3}$$

where $\sigma_x = 0.37\,\mathrm{mm}$ is the beam size at the slit mask. The comparison shows, that the initial beam size due to the finite slit width leads to an overestimation of the emittance on the scale of $\sim 33\,\%$. The difference to the simulation values might be due to the neglection of the phase space correlation, as well as poor angular resolution.
At a drift length of around 2 m the reconstructed emittance values for an opening of 10 µm and 50 µm when including space charge effects have an almost vanishing slope. From 2 m on the error in projected emittance reconstruction is determined by the space charge forces in the beam transport. These however depend on the slit width, a projected emittance measurement with a 10 µm-wide slit shows only a slightly increased reconstructed emittance when including space charge forces.
For the simulation run without space charge fields the systematic emittance error is below 5 % at 2 m for a slit width of 50 µm, while being even below 1 % for a slit width of 10 µm. However, when the space charge forces are considered in the simulation the systematic error in the 50 µm case is ~9 % at 2 m, while being 1.5 % for the small slit width. Similar reconstruction errors are also achieved at a drift length of 3.13 m, i.e. the drift length used

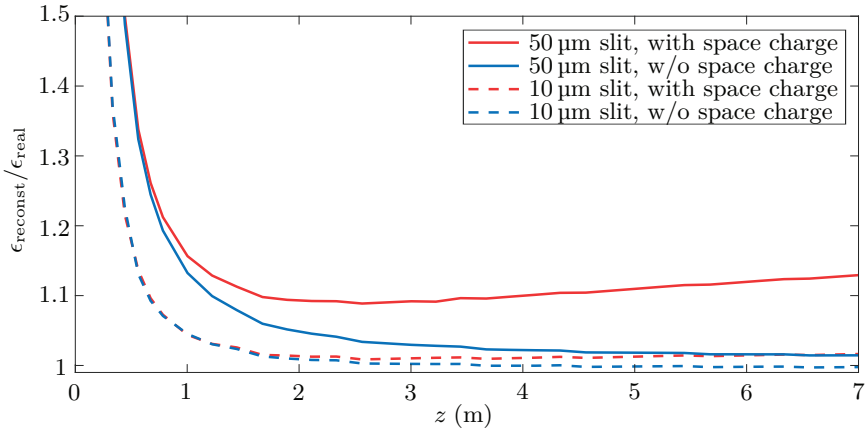

Figure 5.3: Systematic error in projected emittance measurements caused by space charge forces in the beamlets and different slit widths along the drift length z. The simulation shows, that the contribution of the finite slit width to the beamlet size is large close to the slit mask, but decreases for longer drift lengths. Also the influence of the space charge fields is bigger when using the slit mask with 50 µm-wide opening. The screen station for projected emittance is located 3.13 m downstream the slit mask, while the screen for slice emittance measurements is 7 m away.

in regular projected emittance measurements at PITZ, indicating a well-suited setup for projected emittance measurements.
With increasing drift length the systematic error for the slit scan simulation with the 50 µm slit grows up to 13 % at 7 m, when space charge forces are considered. For the other three cases the errors are well below 1.7 %. The reconstruction error of 13 % gives a significant error contribution for slice emittance measurements, as this slit width is used for its measurements due to the higher charge passing the slit, which leads to a higher signal strength.
When reconstructing the phase space from the beamlet images, the contribution from the slit width can be removed via deconvolution of the beam projections. However, the simulation result shows, that for all drift length used at PITZ (and with similar beams as the simulated) this is not necessary, and is therefore not done. It is notable to mention, that for a slit width of 10 µm the error is smaller than one, i.e. the reconstructed emittance is slightly underestimated. This is possibly due to loss of few macro particles in the halo region, which lay beyond the range −2.4 mm and 2.4 mm, which then do not contribute to the reconstructed emittance at all, while being included in ϵ_{real}.

5.2.2 Slit Scan with Quadrupole Magnets without Transverse Deflection

Although Fig. 5.3 shows good measurement accuracy with a drift distance between 2 m and 4 m this setting cannot be used, as the drift space for the slice emittance measurement setup at PITZ is $\sim$ 7 m at least, which reduces the signal intensity on the measurement screen. Therefore a pair of quadrupole magnets is used to increase the signal-to-noise ratio (SNR) as shown in Fig. 4.4. Such a measurement setup is also simulated in ASTRA.
Here, only a slit width of 50 µm is assumed. The experiment is simulated from the slit mask at EMSY1 to the observation screen PST.Scr1 while the TDS is kept off in this simulation. This setting yields a distance of 7 m. In the experiment the quadrupole magnets High1.Q09 and High1.Q10 are used to reduce the horizontal beam size, while focusing the beam vertically. The magnets are located in the beamline at the positions

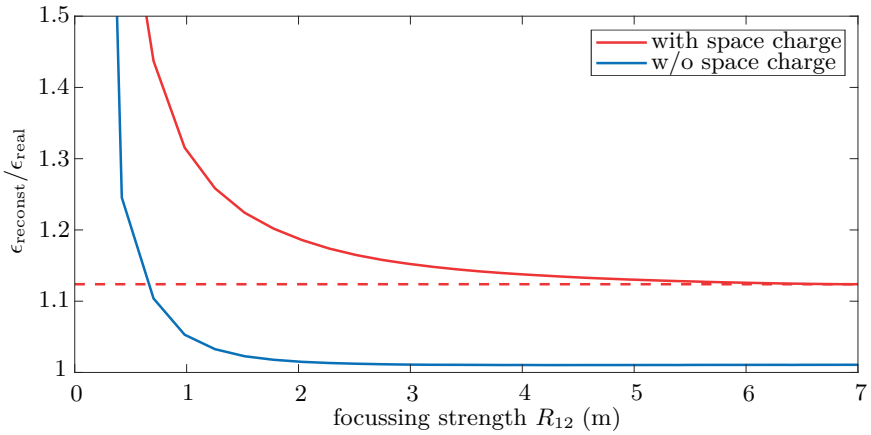

Figure 5.4: Systematic error in an slit scan projected emittance measurement, when the transfer matrix element R_{12} is reduced with the quadrupole magnets High1.Q09 and High1.Q10 to reduce the beam size at the observation screen. The red-dotted line shows the level of systematic error in the emittance measurement, when space charge effects are considered but no quadrupole magnets are used. For focusing strength below $R_{12} = 1.5\,\mathrm{m}$ the error increases rapidly.

$z_{\mathrm{High1.Q09}} = 10.208\,\mathrm{m}$ and $z_{\mathrm{High1.Q10}} = 10.388\,\mathrm{m}$. The focusing magnet currents are set to achieve the wanted beam focusing. In the simulation both quadrupole magnets are set as quadrupole doublet, i.e. they have the same current. In the experiment the strength of both quadrupole magnets is set more freely, to minimise the vertical beam size y_{rms} while achieving the R_{12} value in the horizontal plane the operators aim for. In total the absolute currents of both focusing magnets might differ by up to $\sim 10\,\%$ in experiment.
The beam transport is then simulated from the slit to the observation screen with different focusing strengths. The range of transfer matrix elements R_{12} assumed in simulation is $0.13\,\mathrm{m} \leq R_{12} \leq 7\,\mathrm{m}$. The result is shown in Fig. 5.4. The case where the quadrupole gradients are set to zero is given at $R_{12} = 7\,\mathrm{m}$. It is the same point which is shown in Fig. 5.3 at 7 m. This case gives a baseline for the systematic error: It includes the error in the emittance reconstruction resulting from finite slit width, as well as space charge forces in the drift in one case. With focusing the beam size starts to decrease. This degrades the angular resolution and increases the space charge forces due to the higher charge density. Therefore, the systematic error starts to rise already for small focusing strength around 6 m. It then grows further for even smaller R_{12} values, reaching a total reconstruction error of $\sim 15\,\%$ at $R_{12} = 3\,\mathrm{m}$. The comparison with the systematic error curve without space charge forces behind the slit shows, that this error is caused by space charge forces. The blue curve in Fig. 5.4 shows no error for focusing strength between $R_{12} = 7\,\mathrm{m}$ down to 2 m. Only for even stronger focusing strength a big systematic error arises, due to the rapid worsening of the angular resolution.
The plot shows, that for focusing strength with R_{12} below 3 m the reconstruction error increases strongly when including space charge forces in the simulation. Therefore a focusing strength with R_{12} values around 3 m or slightly above are considered for the experiment. However, this simulation does not contain the reduction in systematic error due to an increased signal-to-noise ratio. Also, the deflecting cavity still has to be included to give rise to slice emittance measurements. This is described in the following section.

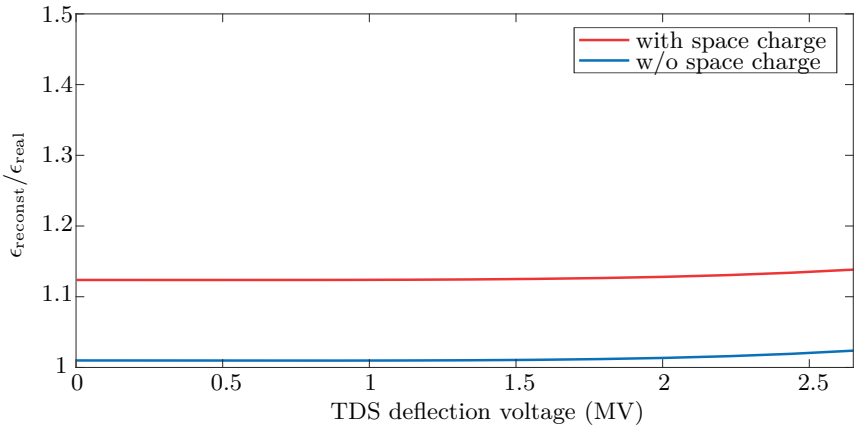

Figure 5.5: Systematic error in an slit scan emittance measurement, for different TDS deflection voltages, when no focusing magnetic fields are applied. The data shows only a minor increase in error for high voltages. For voltages below 1.7 MV, i.e. the maximal deflection voltage of the PITZ TDS, the systematic error increase is negligible. The 13 % systematic error comes from space charge forces, which defocus the beam right after the slit mask.

5.2.3 Slit Scan with Transverse Deflection

The electromagnetic fields inside an rf deflector can lead to an additional error in the emittance reconstruction. At first, the effect solely arising from the TDS fields inside the drift is analysed. For this, again the beam is tracked from the slit mask to the observation screen at different slit positions, while the three-dimensional field map of the TDS cavity is included in the simulation. The quadrupole magnets are neglected, while the TDS fields are scaled in amplitude, to see a dependence on the effective deflecting voltage V_0. The voltage is scanned between 0, i.e. no deflection, and 2.65 MV, while the PITZ TDS has a design deflection voltage of 1.7 MV [30]. The rf field phase was set, so that the beam centre is not deflected. Again, the simulation is carried out while including and excluding space charge effects. The resulting curves are depicted in Fig. 5.5. In the case of no deflection, the systematic error is given again by the error arising from space charge forces during the beam transport in the pure drift, as well as the finite spatial and angular resolution. For higher deflection voltages no significant increase in systematic error of the projected emittance is found. Only for the highest simulated deflection voltages a small increase in the error by only 1 % is seen. A possible reason might be non-linear defocusing rf fields in the TDS, which increase the beamlet divergence slightly. Compared with the magnitude of the other systematic errors, as well as the range on which this error is achieved, this one is negligible. Yet, at higher deflection voltages the charge density on the observation screen becomes smaller, leading to a lower signal strength, and therefore to a smaller signal-to-noise ratio.
Due to the separation of the particles at different longitudinal positions on the screen now the slice emittance can be calculated as well. The reconstructed slice emittance curves while assuming different TDS deflection voltages is depicted in Fig. 5.6. In this plot, space charge effects have been considered during the beam transport. The beam was cut into 1000 slices for the reconstruction of the slice emittance.
The plot shows, that at higher deflection voltages the reconstructed slice emittance in the tail increases, until it reaches a high value around 3 µm at slices around −3 mm. In the centre the slice emittance curves are similar for all but the lower deflection voltage of 0.45 MV. Here the vertical beam size gives a significant contribution to the vertical bunch

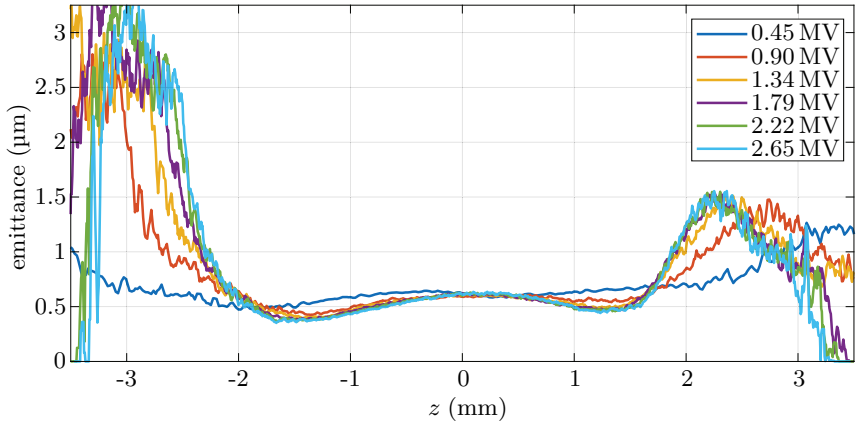

Figure 5.6: Reconstructed slice emittance curves for different TDS deflection voltages when considering space charge forces. For higher voltages the reconstructed slice emittance is increasing, particularly in the tails. This is probably due to the reduced number of macro particles in this area, leading to poor sampling of the beam. The temporal rms resolution is given by the unsheared beam size divided by the shear parameter and is different for each voltage.

profile according to Eq. 3.8.1 and Eq. 3.8.6 due to the low TDS deflection voltage, which causes a small shear parameter.
Figure 5.7 shows the reconstructed slice emittance curve for a TDS deflection voltage of 2.65 MV with and without inclusion of space charge fields in the simulation. The reconstruction with and without space charge forces are fairly close: At the tails no significant difference is observed between the green and purple curve. Only in slices between -1.75 mm and 1.75 mm a difference is observed between both reconstructions. At this slices space charge effects lead to an overestimation of measured emittance. Additionally, the actual slice emittance curve is shown in blue. Comparison between the different curves show, that the slice emittance in the centre is overestimated by 4 % when no space charge forces are considered, while by 16 % for the case with space charge forces, compared to the actual emittance curve.
This is different at the head and tail of the reconstruction: While both reconstructions are akin in this regions, they both show significant differences to the actual slice emittance curve. Both the actual slice emittance curve and the two reconstructions show a high slice emittance at the head and tail, much bigger than in the centre. However, the actual slice emittance curve shows only a maximal slice emittance of 0.76 µm, the slice emittance in the reconstructions reaches up to 3.5 µm. A possible reason might be the large beam size of the slices at the tails, which leads to slice mixing due to the poor temporal resolution. The slice mixing then leads to a larger phase space ellipse, when the slice mismatch is changing for different slices. The overlap of different slices at the tails then leads to a big emittance.
With the measurement of the time-resolved second-order beam moments, as well as the slice emittance, projected emittance decomposition according to Sec. 2.5 is possible. The charge-weighted average slice emittance, mismatch emittance, and linear and non-linear misalignment emittance are calculated for the macro particle distribution at the slit position, and compared with the calculations from the reconstructions with and without space charge forces at different deflection voltages. The slice emittance and mismatch emittance are shown in Fig. 5.8.
The slice properties are analysed from the vertical profile of the beam images on the observation screen. Even at a deflection voltage of 0 MV time-resolved properties can be

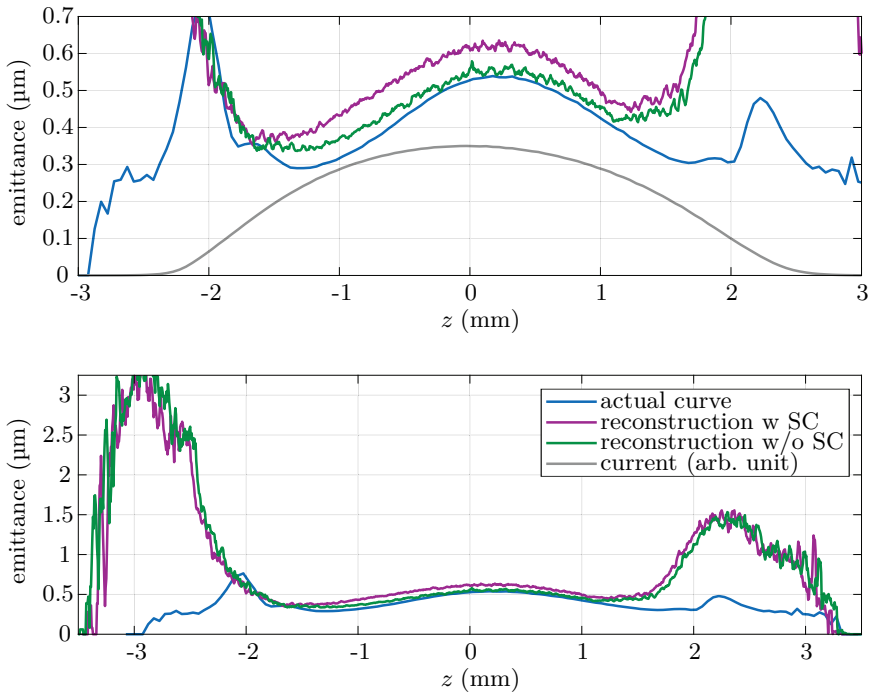

Figure 5.7: Reconstructed slice emittance curves with (purple) and without (green) consideration of space charge forces in the beam transport, together with the actual slice emittance curve (blue). The top plot is a magnification of the lower figure. The reconstruction without space charge forces is only slightly larger at the centre slices. Considering space charge forces a 16 % higher slice emittance is reconstructed compared to the actual (blue) slice emittance curve. At the tails the error is much bigger.

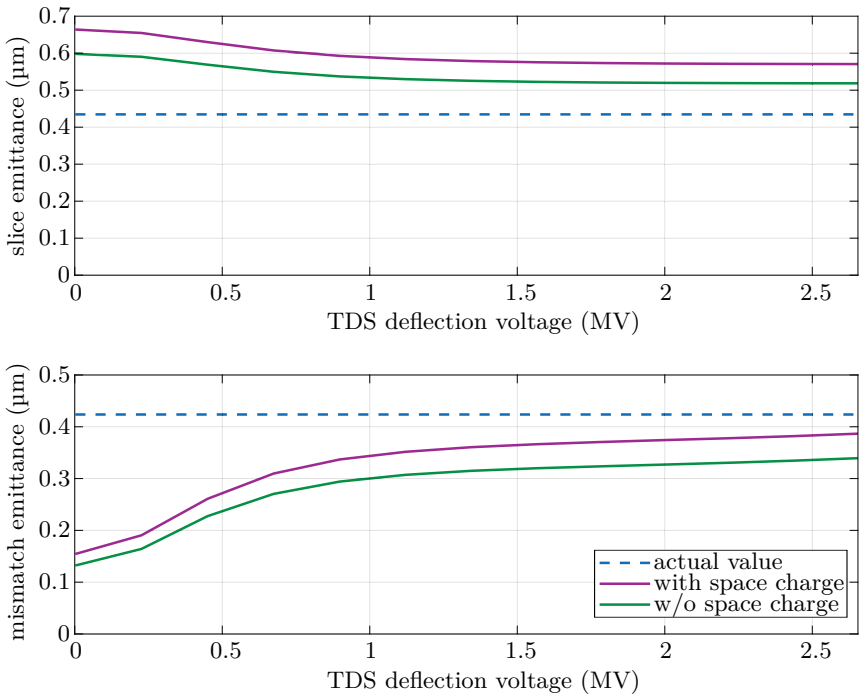

Figure 5.8: Charge-weighted average slice emittance and mismatch emittance of the distribution at the reconstruction point, i.e. the slit position (blue, dashed line), as well as the reconstruction with (purple) and without (green) space charge effects during the beam transport versus effective TDS deflection voltage. The slice-averaged slice emittance is overestimated along the whole range of deflection voltages simulated, while the mismatch emittance is underestimated. With space charge forces included always a higher emittance is measured.

calculated, even though they cannot be resolved. Therefore, the values at low deflection voltages do not bear physical meaning. The charge-weighted, averaged slice emittance is overestimated both with and without space charge forces over the whole simulated range. At higher deflection voltages, the error reduces to 31 % for the reconstruction which is considering space charge effects, while still 19 % without consideration of space charge forces. The reconstructed mismatch emittance on the other hand is underestimated at all deflection voltages. It grows at increasing deflection voltages, and reaches the minimal difference at the highest simulated voltage of 2.65 MV. Here, the mismatch emittance is underestimated by 9 % and 20 %, respectively. The linear and non-linear misalignment emittance curves are not shown, as no symmetry-breaking elements are included in the simulation. The misalignment emittance values only differ from being exactly zero due to numerical noise in simulation.
When the squared emittance contributions are added up according to Eq. 2.5.1 and the square root is calculated, the curves shown in Fig. 5.5 are reconstructed.

5.2.4 Slit Scan with Quadrupole Magnets and Transverse Deflection

Finally, the influence of both the rf deflector and the focusing quadrupole magnets is analysed. Again, the beam is tracked from the slit mask at EMSY1 to the observations screen at different slit positions to reconstruct the emittance from the screen images. The quadrupole magnets High1.Q09 and High1.Q10 are scanned in strength, while the TDS

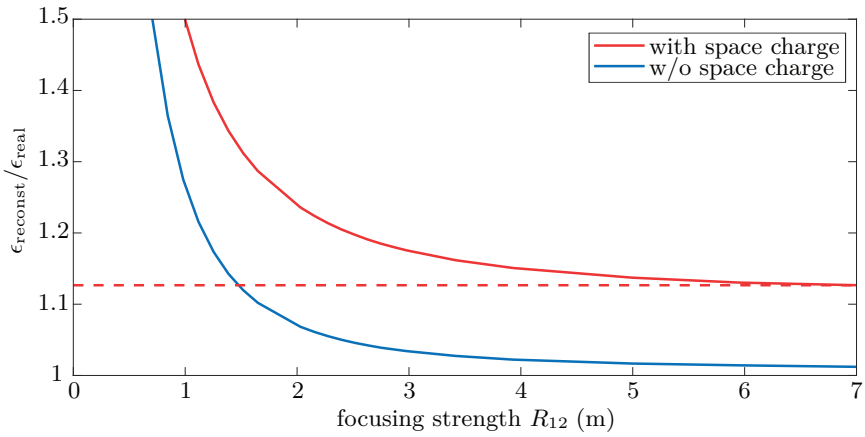

Figure 5.9: Systematic error in projected emittance measurement for different focusing strength R_{12}, while the TDS deflects the beam vertically.

deflection is kept at a deflection voltage of 1.7 MV. First the error in projected emittance is looked upon. It is shown in Fig. 5.9. Compared to Fig. 5.4, where no rf deflection was assumed, this curves exhibit a higher systematic error in the projected emittance reconstruction for the case with space charge effects. Here, the error starts rising from the baseline error of 13 % for little focusing strength already, i.e. transfer matrix elements R_{12} slightly smaller than 7 m. At a focusing strength of $R_{12} = 3.5$ m a total error of 16 % is reached. It then grows rapidly towards smaller transfer matrix elements R_{12}, reaching already a 24 % error at $R_{12} = 2$ m. The error curve for the case without space charge forces grow slower and stays below the case with space charge forces, but grows also faster than in the case without included rf deflector. At a focusing strength of $R_{12} = 1.67$ m the systematic error without space charge forces reaches 10 %, and is even much higher for smaller R_{12} values.

The slice emittance, reconstructed from beam images at different focusing strength, is depicted in Fig. 5.10. The plot displays a reduction of reconstructed slice emittance in the tails towards smaller R_{12} values, while the reconstructed slice emittance grows towards smaller R_{12} values at the centre, explaining the increase of reconstructed projected emittance towards tighter horizontal focusing.
These errors lead then also to errors in the calculation of the slice emittance, which is depicted in Fig. 5.11. At the centre of the bunch the reconstructed slice emittance is off the actual slice emittance by 16 % when space charge effects are considered in the beam transport. This is the same value as seen in Fig. 5.7 for a scan with the TDS, but without focusing quadrupole magnets. When space charge forces are excluded, the reconstructed emittance is only off by ~ 4 % at the centre of the bunch. The slice emittance at the tails is again strongly overestimated, both with and without space charge forces. However, for stronger focusing, i.e. smaller R_{12} values, the error decreases by ~ 50 % in the tail. In the head the error is slightly bigger at the strongest focusing. At the centre slices no significant increase of error is observed for all focusing strength but the strongest, $R_{12} = 1$ m.

The reconstruction of the slice emittance and second-order beam momenta allows to derive the charge-weighted average slice emittance, mismatch emittance and linear and non-linear misalignment emittance contributions to the projected emittance. Figure 5.12 shows the emittance contribution for different focusing strength, i.e. matrix transfer elements R_{12}. Over the whole range of focusing strength the charge-weighted slice emittance is overestimated, by around 15 % at the focusing strength $R_{12} = 3.5$ m. Space charge effects lead to an even higher error of 28 %. The mismatch emittance is underestimated when no

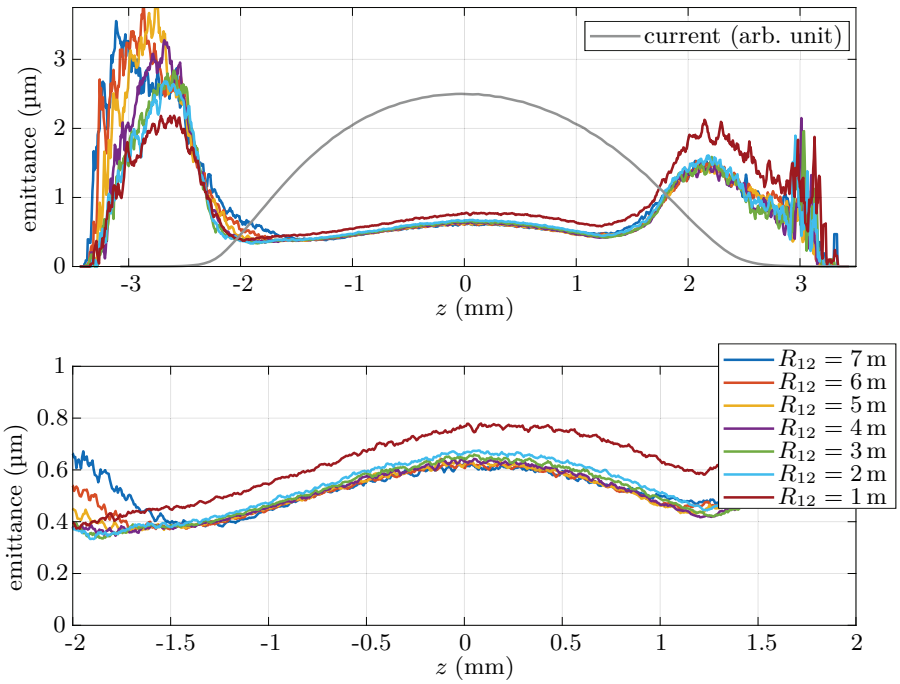

Figure 5.10: Slice emittance curve for different focusing strength R_{12}. Space charge forces were included in the simulation of the transport and the deflection voltage was set to 1.7 MV. The focusing ranges from 7 m, i.e. no quadrupole focusing, down to 1 m, which describes a strong horizontal focus. The bottom plot shows the zoom of the centre part. There is a small increase in reconstructed emittance for reducing R_{12} values, which becomes rapid for $R12 \leq 2\,\mathrm{m}$.

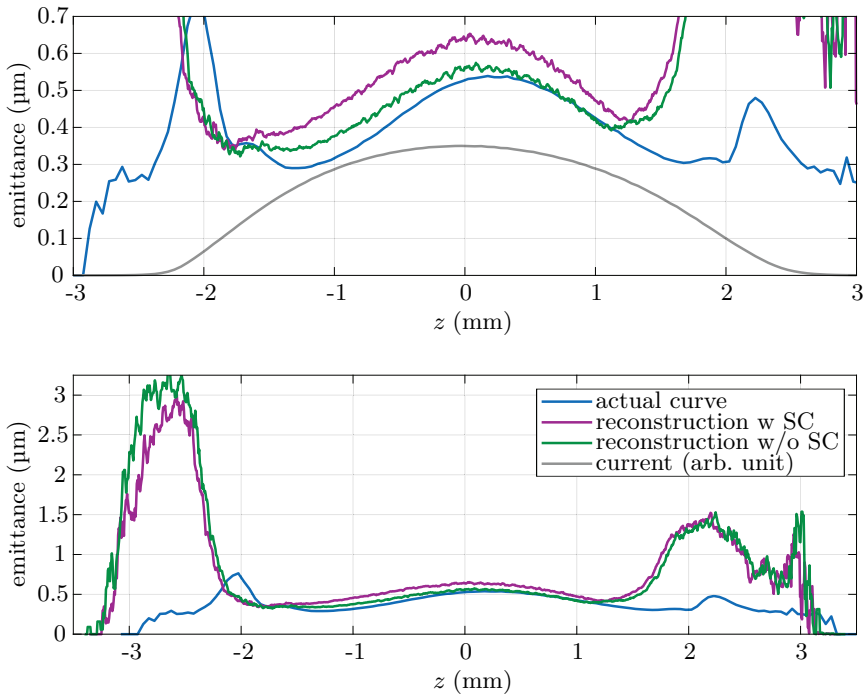

Figure 5.11: Reconstructed slice emittance curves after focusing of the beam with the quadrupole magnets High1.Q09 and High1.Q10 and deflection with the rf deflector. The beam transport in simulation yields $R_{12} = 3.5\,\mathrm{m}$. The purple curve shows the case when space charge effects were considered, green without space charge forces, while blue shows the actual slice emittance curve. The curves show, that the reconstruction overestimates the slice emittance in the head and tail. In the centre the reconstruction is correct when space charge forces are neglected, while $\sim 10\,\%$ higher with space charge forces.

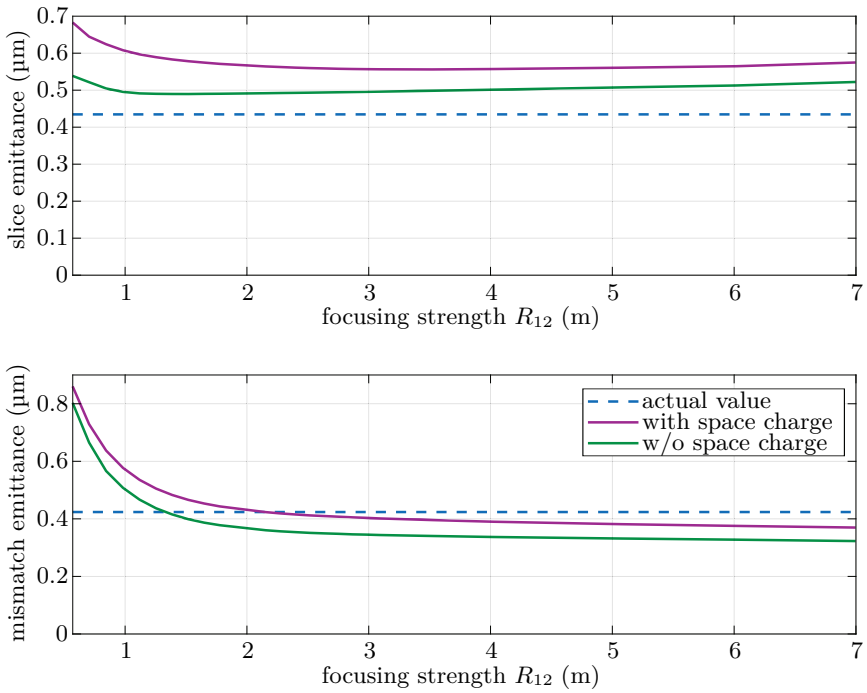

Figure 5.12: Charge-weighted average slice emittance and mismatch emittance for different focusing strength R_{12}. The blue, dotted line shows the actual emittance contribution at the slit position, while the purple line shows the calculated value when space charge forces are considered in the beam transport, while the green curve shows the reconstruction without space charge forces. The plot shows, that for focusing strength with R_{12} above $\sim 3\,\mathrm{m}$ the calculation does not depend on the focusing strength. Nevertheless, space charge forces lead to an overestimation of emittance contributions.

quadrupole magnets are used, i.e. at $R_{12} = 7\,\mathrm{m}$. The reconstructed mismatch emittance grows slightly towards smaller transfer matrix elements R_{12}, until the reconstructed mismatch emittance matches the actual value at $R_{12} = 2.15\,\mathrm{m}$ when space charge forces are considered. From then on, the mismatch emittance grows rapidly towards smaller R_{12}. The linear and non-linear misalignment emittance contributions are not shown, as these differ only slightly from zero due to the numerical noise in simulation. The values are zero, as no symmetry-breaking beamline element is considered, which causes a misalignment of slice centroids. When the slice emittance and mismatch emittance are squared and added, the squared curve shown in Fig. 5.9 is obtained, as suggested by Eq. 2.5.1.

5.2.5 Influence from Longitudinal Momentum Variation

Simulations of the experiment, based on a macro particle distribution, obtained via a start-to-end simulation allows calculation of the error during the emittance reconstruction via slice emittance measurement. Here, different cases have been analysed to synthesise the various contributions to the error, e.g. the finite resolution, space charge effects in the transport or rf deflector fields. It is observed, that a particularly big error occurs during the reconstruction at the tails of the beam. A possible reason might be the so-called *chirp*, i.e. a correlation of energy and longitudinal bunch coordinate, which changes the magnitude of the beam dynamics the bunch undergoes, e.g. focusing. Therefore the longitudinal phase

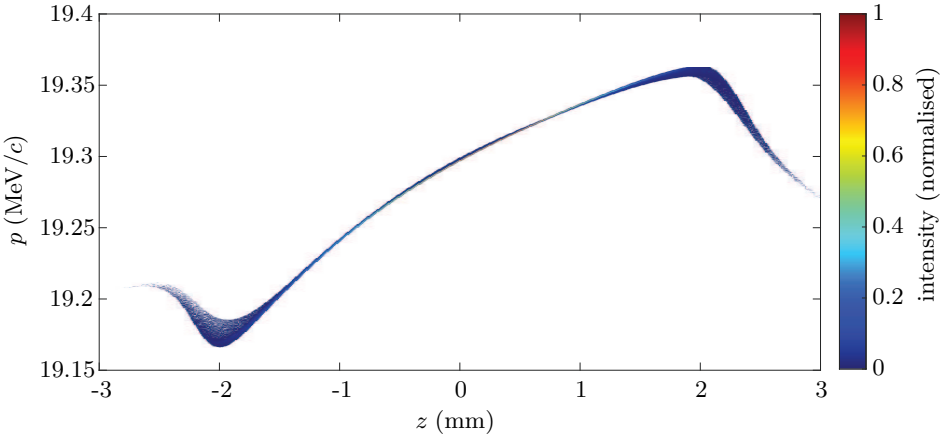

Figure 5.13: Simulation of the longitudinal phase space of an electron beam at the slit position, created with a temporal Gaussian laser pulse. It shows, that different slices have a different momenta along the bunch. Overall, the head has a higher momentum than the tails. Both the gun cavity and CDS booster cavity were set to the accelerating phase with maximum mean momentum gain.

space of the beam is analysed. It is depicted in Fig. 5.13. It shows, that the momentum is indeed not flat, but has a slope over most of the bunch length. The rf phase of the gun and booster have a major impact on the momentum chirp of the beam. During the optimisation of the emittance in the simulation, both rf phases were set to the phase, at which the reference particle witnesses the maximum momentum gain (MMMG phase). However, there is another important contribution to the chirp at PITZ: longitudinal space charge forces. These lead to a further acceleration of particles in the head beyond the acceleration in the cavities, giving them a higher momentum, while simultaneously decelerating particles in the tail, decreasing their momentum. At the head a maximum slice momentum of 19.36 MeV/c is achieved, while at the tail the momentum is only 19.17 MeV/c, as shown in Fig. 5.13. This yields a relative peak-to-peak momentum spread of

$$\Delta p_{\mathrm{P2P}} = \frac{p_{\mathrm{max}} - p_{\mathrm{min}}}{p_{\mathrm{min}}} = 1\,\%. \tag{5.2.4}$$

Henceforth, the error in emittance reconstruction should also be on a percentage level. However, as the errors observed in the Sec. 5.1 and the earlier part of Sec. 5.2 are much bigger than that, i.e. an error from an energy chirp is negligible.

5.3 Statistical Uncertainty

During measurements random fluctuations in the raw data are observed, when measurements are repeated while all measurement inputs are kept constant. These random variations are both in shape and intensity of the beam images, leading to small variations in the processed data. Therefore, a statistical uncertainty is created, which has to be parametrised. The statistical uncertainty calculation is done using Gaussian error propagation according to [92]. To calculate the statistical error, every beam and beamlet image is taken ten times. Then the slice and projected phase space is reconstructed ten times, using each statistical image at each slit position once. This allows to calculate the beam size $\langle x^2 \rangle$, the angular spread $\langle x'^2 \rangle$, and the correlation term $\langle xx' \rangle$ ten times, once for each slice phase space and

once for the projected phase space. The geometric emittance is then calculated from the arithmetic means of the second-order beam momenta according to Eq. 2.2.10. For the uncertainty of the geometric emittance, the uncertainty of the three second-order beam momenta is calculated via the variance

$$\sigma_q = \frac{1}{N-1}\sum_{i=1}^{N}(q_i - \langle q\rangle)^2 \tag{5.3.1}$$

and the covariance term

$$\sigma_{q,p} = \frac{1}{N-1}\sum_{i=1}^{N}(q_i - \langle q\rangle)\cdot(p_i - \langle p\rangle). \tag{5.3.2}$$

Here q and p assume the beam size $\langle x^2\rangle$, the angular spread $\langle x'^2\rangle$, and the correlation term $\langle xx'\rangle$. The arithmetic mean of a quantity q is denoted by $\langle q\rangle$. The correlation matrix

$$C_{\mathrm{X}} = \begin{pmatrix} \sigma_{\langle x^2\rangle} & \sigma_{\langle x^2\rangle,\langle x'^2\rangle} & \sigma_{\langle x^2\rangle,\langle xx'\rangle} \\ \sigma_{\langle x^2\rangle,\langle x'^2\rangle} & \sigma_{\langle x'^2\rangle} & \sigma_{\langle x'^2\rangle,\langle xx'\rangle} \\ \sigma_{\langle x^2\rangle,\langle xx'\rangle} & \sigma_{\langle x'^2\rangle,\langle xx'\rangle} & \sigma_{\langle xx'\rangle} \end{pmatrix} \tag{5.3.3}$$

is then reconstructed from the variances and covariances. Together with the derivative vector

$$A = \begin{pmatrix} \frac{\partial\epsilon}{\partial\langle x^2\rangle} & \frac{\partial\epsilon}{\partial\langle x'^2\rangle} & \frac{\partial\epsilon}{\partial\langle xx'\rangle} \end{pmatrix} = \frac{1}{\epsilon}\begin{pmatrix} \frac{1}{2}\langle x'^2\rangle & \frac{1}{2}\langle x^2\rangle & -\langle xx'\rangle \end{pmatrix} \tag{5.3.4}$$

the variance in the geometric emittance can be calculated via

$$C_{\sigma_\epsilon^2} = A\cdot C_{\mathrm{X}}\cdot A^{\intercal}, \tag{5.3.5}$$

see Ref. [92]. The standard deviation is used as statistical uncertainty. For this, the square root has to be calculated from the variance:

$$\Delta\epsilon_x = \sqrt{C_{\sigma_\epsilon^2}}. \tag{5.3.6}$$

From then on, the normalised slice and projected emittance are calculated using uncorrelated Gaussian error propagation. The uncertainty of the Twiss parameters α, β and γ are determined in a similar way from the uncertainty of the geometric emittance, as well as the second-order beam momenta.
This allows calculation of a statistical rms uncertainty, if several (statistical) images are taken. Like this, a statistical uncertainty can be given for each slice emittance measurement (and for the projected emittance obtained during the slice emittance measurement). Additionally, the measurement is usually repeated few times, while keeping the accelerator settings same. From the measured slice emittance and projected emittance again an average can be calculated. However, as this measurements are only repeated few times (~3 times), a peak-to-peak uncertainty is given instead. The peak-to-peak uncertainty is in the general case also asymmetric in both directions.

5.4 Variation of Beam Optics for Slice Emittance Measurements

Still, the optimum quadrupole magnet setting for slice emittance measurements have to be determined. The goal is to find a focusing setting, in which the signal-to-noise ratio (SNR), i.e. the signal density of the beamlet images is increased. Also, the measured slice emittance should not be sensitive to the focusing strength. A good focusing means a small beam size at the measurement screen along the TDS shearing direction when the

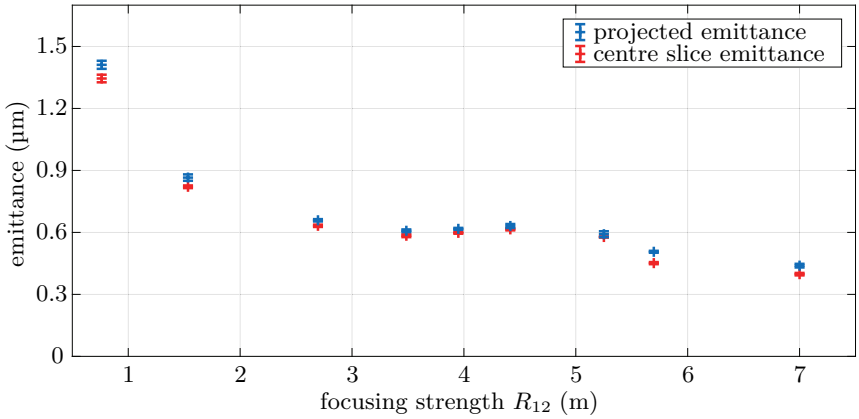

Figure 5.14: Projected (blue) and centre slice emittance (red) against the R_{12} value from the slit mask to the observation screen. It is changed by adjusting the strength of the quadrupole magnets. At $R_{12} = 7\,\mathrm{m}$ the magnets are turned off. For R_{12} values between 2.8 m and 5 m the emittance does not depend on the quadrupole strength, while being increased compared to no focusing due to a higher signal-to-noise ratio. For even smaller R_{12}'s the emittance increases strongly, as the angular resolution decreases.

TDS is turned off. This will help reducing the TDS shearing strength for a certain time resolution, leading to a higher beamlet signal density. Besides, a good focusing means a reduced beamlet size due to horizontal divergence, leading also to a higher signal density, but the reduced horizontal beamlet size should not affect the divergence measurement resolution or increase the space charge effect too much. In order to determine such focusing experimentally, the slice emittance was measured against different focusing strength.
For the measurement the electron momentum after the gun was $6.3\,\mathrm{MeV}/c$, while the main solenoid current was set to 370 A. The photocathode laser pulse had a Gaussian temporal shape with a FWHM duration of 6 ps and a transversely uniform laser pulse profile with an rms beam size of $\sigma_{xy} = 0.24\,\mathrm{mm}$. The laser pulse energy was tuned to create a bunch charge of 250 pC at the gun rf phase with maximum energy gain. The cut disk structure (CDS) cavity accelerated the electron further to an electron momentum of $19.4\,\mathrm{MeV}/c$ at the on-crest phase.
In total, the slice emittance was measured nine times, each with a different focusing strength of the quadrupole magnets High1.Q09 and High1.Q10. The TDS voltage and the number of bunches were kept constant at every measurement. The measured slice emittance of the centre slice, as well as the measured projected emittance is plotted in Fig. 5.14 against the focusing strength R_{12}. The value at $R_{12} = 7\,\mathrm{m}$ shows the case at which the quadrupole magnets are turned off, i.e. the drift space. Here, a projected emittance of $(0.46 \pm 0.01)\,\mu\mathrm{m}$ is measured, while the centre slice emittance is measured to be $(0.42 \pm 0.01)\,\mu\mathrm{m}$. These values are the lowest measured projected and centre slice emittance during the scan. For stronger quadrupole focusing, i.e. smaller R_{12} values, both the projected and slice emittance increase. For focusing strength between $R_{12} = 2.8\,\mathrm{m}$ and 5 m the emittance value is not sensitive to the R_{12} values. The projected emittance is around 0.66 µm, while the measured slice emittance is around 0.65 µm (for $R_{12} = 3.95\,\mathrm{m}$). The centre slice phase spaces, measured for $R_{12} = 7\,\mathrm{m}$ and $R_{12} = 3.95\,\mathrm{m}$, are shown in Fig. 5.15.
The images show, how the quadrupole magnet focusing increases the measured (slice) emittance. For the case with focusing, the signal-to-noise ratio is higher, see Fig. 5.16. For

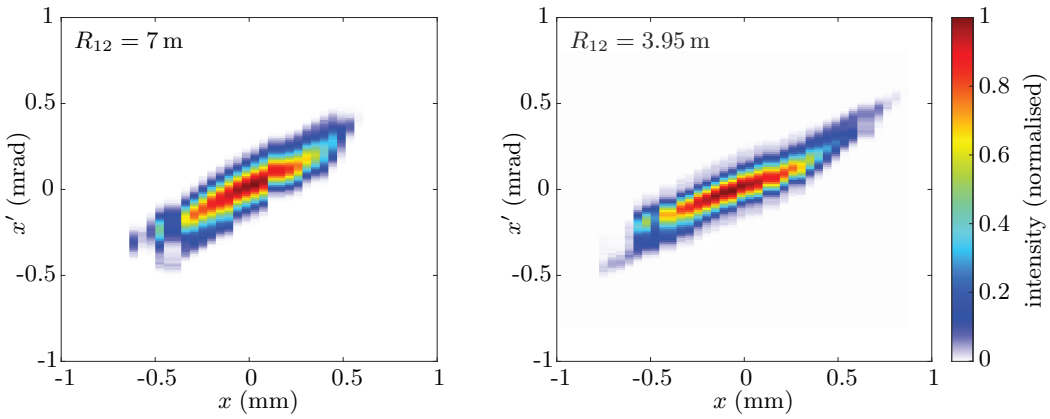

Figure 5.15: Centre slice phase spaces, measured with $R_{12} = 7\,\mathrm{m}$ (left) and $R_{12} = 3.95\,\mathrm{m}$ (right). With focusing quadrupole magnets, areas with smaller signal strength, i.e. the spatial tails, are detected in the measurement. Thus a higher (slice) emittance is measured, as a bigger fraction of electrons is considered in the phase space reconstruction. The slice thickness is on the scale of $\sim 2\,\mathrm{ps}$.

the calculation of the signal strength the raw images are filtered in a similar manner as for the phase space reconstruction. Additionally to the standard image filter, a median filter is applied to the signal images, to remove so-called *salt-and-pepper noise*[2] on the images. As signal level, the ten-times averaged maximum pixel value found in the filtered images is used. For the calculation of the noise level the background images are used. In a first step, the ten-times-averaged background images are subtracted from the background, so the average pixel filling is zero. This is done for all ten taken background images. In a second step, the rms pixel value spread due to noise is calculated. For this, the pixel values from different background images and different pixel itself are considered. The rms noise level is on the order of 7 counts.
Figure 5.16 shows, how the SNR increases for decreasing R_{12}. For a measurement without the use of focusing quadrupole magnets the SNR is only around 29.6 ± 0.3 and increases up to 104 ± 1 for the strongest focusing. The increase of SNR allows to measure parts of the phase space with low intensity, which otherwise are below the noise floor. Hence, the right image of Fig. 5.15 shows longer transverse tails in the phase space, i.e. a wider beam, but a similar core phase space as the lower SNR case. Therefore, the measured slice emittance is higher.
When the beam is further focused, so that R_{12} drops below 2.8 m, the measured emittance values increase. At the smallest measured transfer matrix element $R_{12} = 0.76\,\mathrm{m}$ a projected emittance of $(1.57 \pm 0.02)\,\mu\mathrm{m}$ is measured, while the centre slice emittance is measured to be $(1.53 \pm 0.02)\,\mu\mathrm{m}$. The sharp increase for small R_{12} values is also observed in simulations of the experiment, shown in Sec. 5.2.2.
The projected, scaled emittance, measured with fastscan, see Sec. 4.2, is $\epsilon_x = 0.72\,\mu\mathrm{m}$, while the non-scaled emittance is $0.60\,\mu\mathrm{m}$. Its R_{12} value is $\sim 3.1\,\mathrm{m}$ and SNR ~ 300. Thus, the use of quadrupole magnets to tune the transfer matrix element R_{12} to values between 2.8 m and 5 m allows to measure an emittance which is close to the unscaled, projected emittance, measured with the standard setup, while stronger quadrupole focusing introduces systematic errors, i.e. a poor beam divergence measurement resolution, which spoils the slice emittance measurements. This measurement was performed twice, where

[2]Salt-and-pepper noise is given by single pixel values with very high or very low pixel filling, which are surrounded by pixel with average pixel filling. It originates from X-ray Bremsstrahlung and scattered electrons. This noise spoils the calculation of the SNR, and is thus removed.

the outcome was the same. Therefore, the slice emittance measurements are carried out at quadrupole magnet focusing strength, which yield a transfer matrix element R_{12} between 3 m and 4 m.

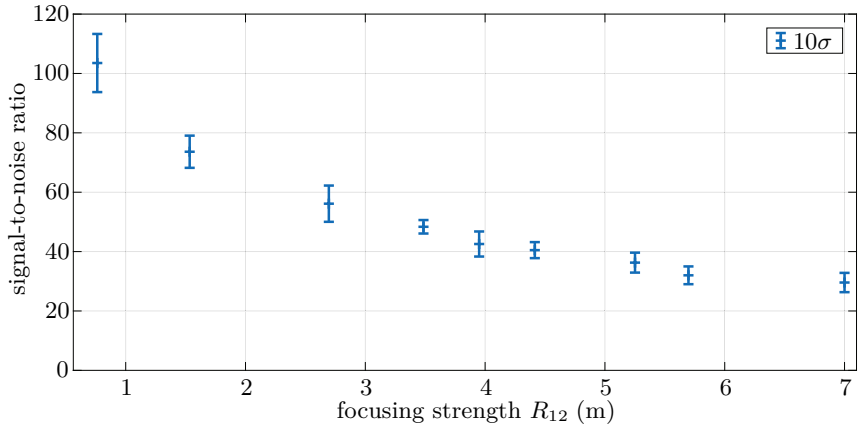

Figure 5.16: Plot of the peak signal-to-noise ratio for varying focusing strength R_{12}. After application of the image analysis, a median filter is applied to remove single, high intensity pixel values, which spoil the signal calculation. The peak signal is used for the calculation, while the rms pixel value of background images is considered as noise level. The error bars are plotted ten times bigger for better visibility.

5.5 Scan of Transverse Deflecting Cavity Voltage for Slice Emittance Measurements

Besides the focusing strength of the quadrupole magnets, the transverse deflecting cavity voltage affects both the time resolution and the SNR, therefore changing the slice emittance results, too. For the analysis of the TDS deflection voltage effects on the measured slice emittance data measurements at five different TDS voltages have been performed. For the analysis of the TDS deflection voltage effects on the measured slice emittance, the photoinjector is operated in the same way as described in Sec. 5.4, with the difference that the main solenoid current is set to 368 A, while the bucking solenoid magnet was off. This leads to increased emittance numbers.
As the TDS does not allow for a measurement of the power inside the cavity, the TDS deflection voltages are calculated from the measured shear parameters and the beam momentum by rearranging Eq. 3.8.3:

$$V_0 = \frac{Spc}{ekL}. \tag{5.5.1}$$

The measured projected and slice emittance are shown in Fig. 5.17. The R_{12} value was 2.96 m during the measurement. The plot shows, that for higher deflection voltages a slightly smaller emittance is measured. This applies for both the projected and slice emittance. A linear graph, fitted to the projected emittance values, is plotted in Fig. 5.17 as well. The linear graph has a slope of $m = -0.17\,\mu\text{m/MV}$.
Furthermore, the deviation of the two measured centre slice emittance values for a deflection strength of 0.66 MV shows, that the fluctuation between different measurements are strong, compared to the slope of the measurement.
Figure 5.18 depicts the FWHM bunch length, measured at the different TDS voltages,

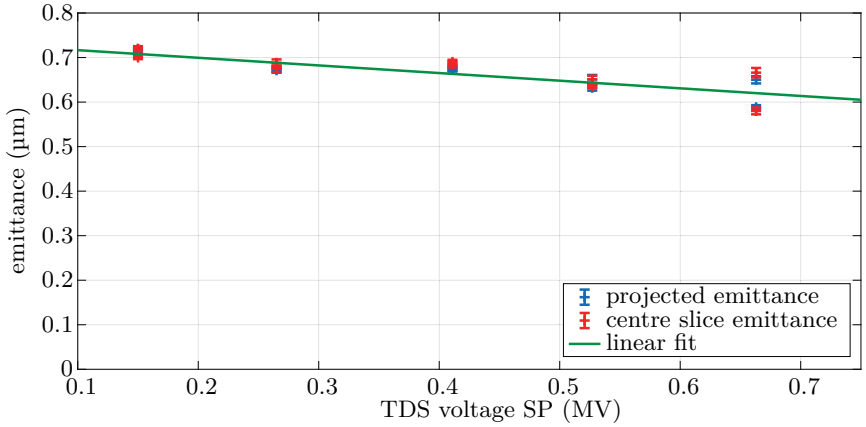

Figure 5.17: Plot of projected (blue) and centre slice emittance (red) against the TDS deflection voltage setpoint (SP). The R_{12} value was set to 2.96 m. The linear graph, fitted to the projected emittance value (green) shows, that with increasing deflection strength the measured emittance decreases slightly. The slices have a temporal width of ~ 1.8 ps.

and the corresponding time resolution of the measurement. The resolution is given by the vertical FWHM beam size of the beam when the TDS is off over the shear parameter and the speed of light:

$$\sigma_{\text{res}} = \frac{\sigma_{y,\text{FWHM}}}{Sc}. \tag{5.5.2}$$

The plot shows, that the measured bunch length is slightly increased for the smallest deflection voltage. Most likely, this is caused by the underestimation of the bunch length at high deflection voltages due to low SNR. Furthermore, the improvement of the time resolution is shown. A resolution of 0.22 ps still allows to distinguish up to 44 slices, while a number of ten slices is already sufficient to distinguish between head, tail and core of a bunch. The peak-to-peak bunch length is cut into eleven slices for calculation of slice emittance, where each slice has a peak-to-peak length of around 1.8 ps. Thus, the temporal resolution of 1 ps is more than sufficient to resolve the slices. While the resolution increases for higher TDS voltages, the SNR decreases. This leads to an emittance underestimation. Hence in future the TDS voltage should be set as small as possible, while ensuing that the needed temporal resolution is achieved. Like this, the underestimation of emittance is minimised.

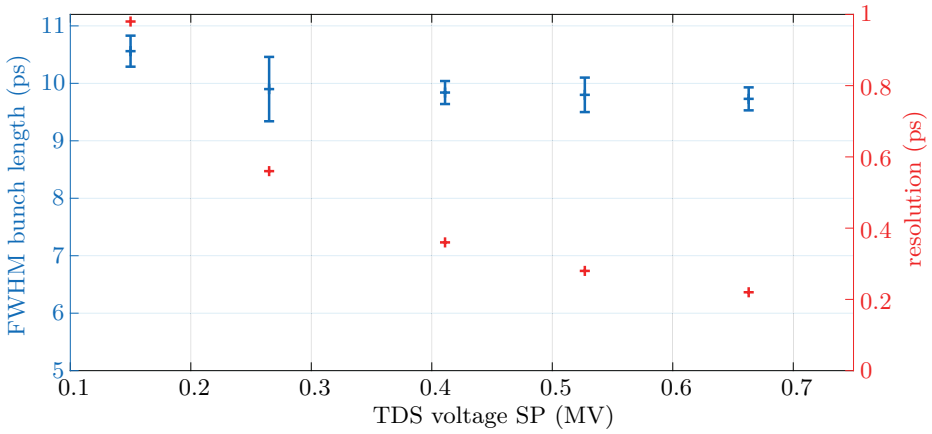

Figure 5.18: Measured FWHM bunch length and time resolution against the applied TDS deflection voltage. While the resolution decreases gradually for higher deflection voltages, the FWHM bunch length comes quickly to a stable level, at which the bunch length is measured reliably.

5.6 Summary of Slice Emittance Diagnostics Error Analysis

This chapter reviewed the methodology studies on time-resolved emittance diagnostics at PITZ, which has been developed and improved during this thesis. It is based on the use of a single-slit scan, to determine the transverse beam size, angular spread and correlation, with an rf deflector, used to spatially separate electrons according to their longitudinal position on a subpicosecond time scale, allowing calculation of the slice emittance. Low signal strength and space charge forces are the major challenges to tackle when developing such a scheme. The degrading effect of space charge effects was reduced by employing the slit scan. To improve the signal-to-noise ratio for a correct emittance reconstruction several steps were taken. The slit masks at PITZ are equipped with 10 µm and 50 µm-wide slits. The wider have been chosen for the experiment, as they pass roughly five times more charge, giving a five times higher signal, while simultaneously increasing the error in emittance reconstruction due to space charge forces. A further improvement was a scintillator screen, which has a higher light yield compared to the standard PITZ scintillator screens. Focusing quadrupole magnets have been used, to reduce the beam size on the screen, increasing the charge density, and henceforth the signal strength. Changes have also been made to the camera imaging optic: The imaging optic has been moved approx. two times closer to the screen to increase the light yield.
Yet, simulation studies showed that space charge forces lead to an overestimation of slice emittance in the applied measurement scheme for the PITZ-typical electron beam parameters. Moreover, analytical studies showed, that the finite signal-to-noise ratio would lead to emittance underestimation. Due to the opposite systematic errors on slice emittance, the measured slice emittance is close to true values for the central slice. Figure 4.16 depicts a simulated measurement result with a transfer matrix element $R_{12} = 3.5\,\mathrm{m}$ for different SNRs. Figure 5.16 shows, that a SNR of 50 can be achieved for such case. A comparison between the actual slice emittance curve, and the reconstructed slice emittance curve is given in Fig. 5.19. At this condition the reconstructed centre slice emittance is close to the actual slice emittance, yielding a small net systematic error, allowing precise centre slice emittance reconstructions. At $z = 0\,\mathrm{m}$ the error is 4 %.

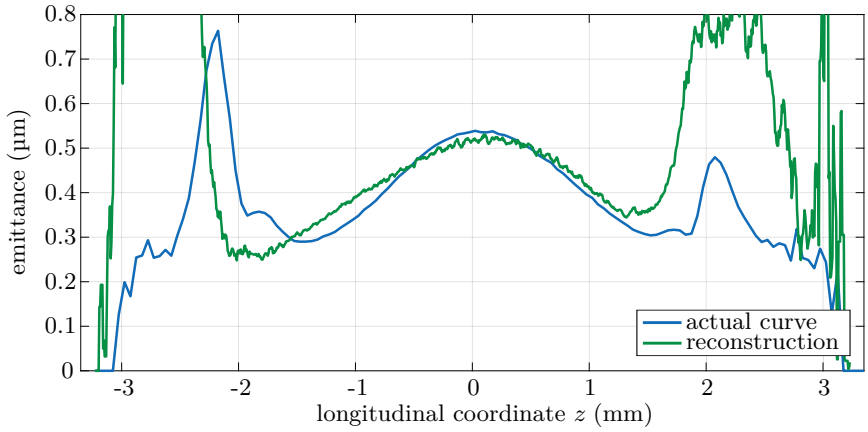

Figure 5.19: Comparison of the simulated slice emittance curve (blue) and the slice emittance, reconstructed from intensity-cut beamlet images with an assumed SNR of 50, a horizontal focusing yielding a transfer matrix element $R_{12} = 3.5\,\mathrm{m}$ and an rf deflector voltage of 1.7 MV. While both curves deviate strongly in the tails, the centre of the bunch shows only a relative difference of 4 %.

6 Slice Emittance Measurements

A low transverse beam emittance is needed to maximise the Pierce parameter, which indicates a high performance of a free-electron laser (FEL). As only technologically demanding schemes exist to reduce the transverse emittance of an electron beam after its emission, i.e. transverse-to-longitudinal emittance exchange [83], it is the best, to create an electron beam with a low transverse emittance at the source. Strong non-linearities in transverse space charge forces lead to degradation of the rms emittance in photoinjectors. Application of rf cavities with strong cathode field gradients can be used to reduce the emittance degradation, but this is also limited by cavity cooling capabilities. Therefore pulse shaping is employed to form a photocathode laser pulse which leads to the emission of an electron beam which creates only small non-linearities in space charge forces. This chapter contains the results of transverse emittance optimisation of electron bunches emitted from laser pulses with different pulse shapes. All beams have a charge of 250 pC. The projected emittance is optimised experimentally using the procedure described in Ref. [25], before the slice emittance is measured and compared with start-to-end simulations of the measurements, carried out in ASTRA [41]. The projected rms emittance decomposition according to Sec. 2.5 is done with the experimental and simulation results. Section 5.6 showed, that the systematic error is on the scale of 4 %. As the statistical uncertainty is larger, the measurement results are dominated by statistical uncertainty. Therefore the error given is the statistical uncertainty, unless stated differently.

6.1 Transverse Flattop and Longitudinal Gaussian Beam Profile

Gaussian laser distributions, both transverse and temporal, are commonly available in most laser systems, but the non-linear space charge forces from a Gaussian charge distribution degrade the rms beam emittance. To linearise the transverse space charge forces to improve the transverse rms emittance, the transverse laser profiles are shaped with an aperture by cutting out the central part of the Gaussian distribution for a quasi-uniform distribution. Then the transverse beam shaping aperture (BSA) is imaged onto the cathode to emit the photoelectrons.

Such a laser profile is routinely used at PITZ. Figure 6.1 shows a typical transverse flattop laser profile of 1 mm diameter used to optimise the emittance of a 250 pC beam, which is the main working point of the Eu-XFEL [91, 93]. The transverse laser profile is measured by a CCD camera at a $1:1$ imaging plane of the cathode (called the virtual cathode). For an ideal uniform distribution, 1 mm diameter corresponds to an rms size of $\sigma_x = \sigma_y = 0.25\,\text{mm}$, while the actual measurement shows an rms sizes of $\sigma_x = (0.239 \pm 0.001)\,\text{mm}$ and $\sigma_y = (0.246 \pm 0.001)\,\text{mm}$ for horizontal and vertical projections respectively.

The transverse laser profile shows also several diffraction rings, as the spatial bandwidth of the imaging optics from BSA to photocathode crops the higher frequencies. The dark spot inside the laser profile is most likely a camera measurement artefact, caused by dust grains lying on the camera chip or on an optical surface near the image plane.

In order to characterise the longitudinal laser pulse envelope, a measurement with the optical sampling system (OSS) is done. It is a cross-correlator, which crosses the short IR laser pulses from the laser oscillator with the UV laser pulse after the two second-harmonic generation crystals, see Fig. 3.2. The measurement of the temporal laser pulse profile is

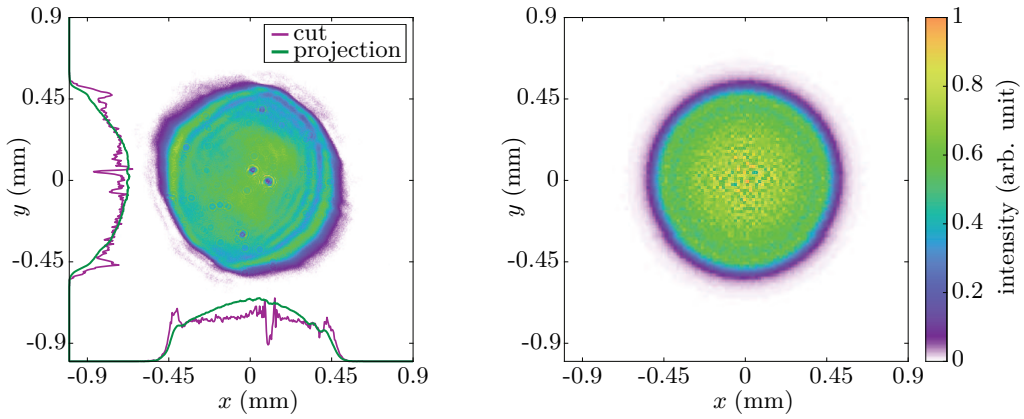

Figure 6.1: Laser beam on the camera at the virtual cathode position. The BSA was set to 1 mm, yielding a horizontal rms beam size of 0.239 mm and a vertical rms beam size of 0.246 mm. The cuts are done through the centre of the beam, i.e. $(0, 0)$. Dust grains on the camera chip lead to the spots with low intensity in the profile. The right image shows the initial electron distribution at the cathode, as it is considered in simulation.

shown in Fig. 6.2. A Gaussian function has been fitted to the temporal pulse profile. The resulting function has the form

$$f(t) = 1.05 \cdot \exp\left[-\left(\frac{t - 0.14\,\text{ps}}{3.29\,\text{ps}}\right)^2\right], \tag{6.1.1}$$

yielding a FWHM pulse length of 5.44 ps. In simulations, a Gaussian laser pulse length of 6 ps is assumed. The laser power was tweaked to achieve a bunch charge of (246 ± 10) pC.

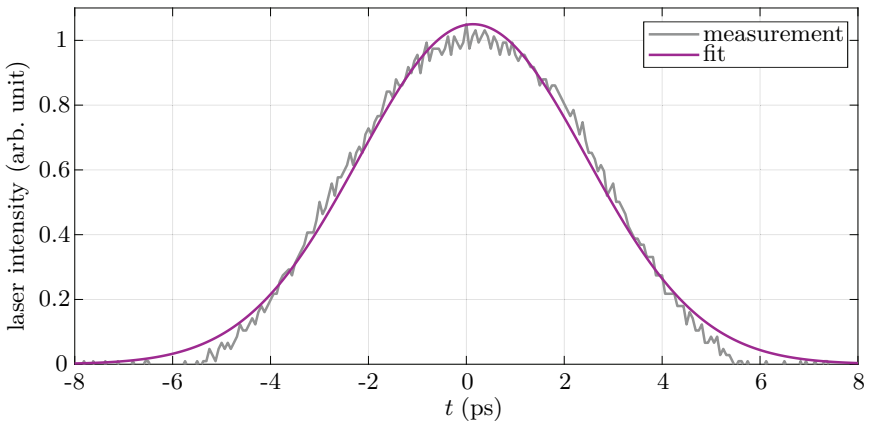

Figure 6.2: Temporal intensity profile of the photocathode laser pulse (grey), together with a Gaussian fit to the profile (purple). The measurement was done with the OSS. The fit shows a FWHM pulse length of 5.44 ps.

The power in the gun cavity was set to achieve a beam momentum of $p_{\text{Gun}} = 6.24\,\text{MeV}/c$, which corresponds to a cathode gradient of $\sim 57\,\text{MV/m}$ and is very close to the gun operation point at the Eu-XFEL. The gun cavity is operated at maximum mean momentum gain (MMMG) phase.
The booster cavity was operated at on-crest, yielding a mean momentum of $p_{\text{Boo}} =$

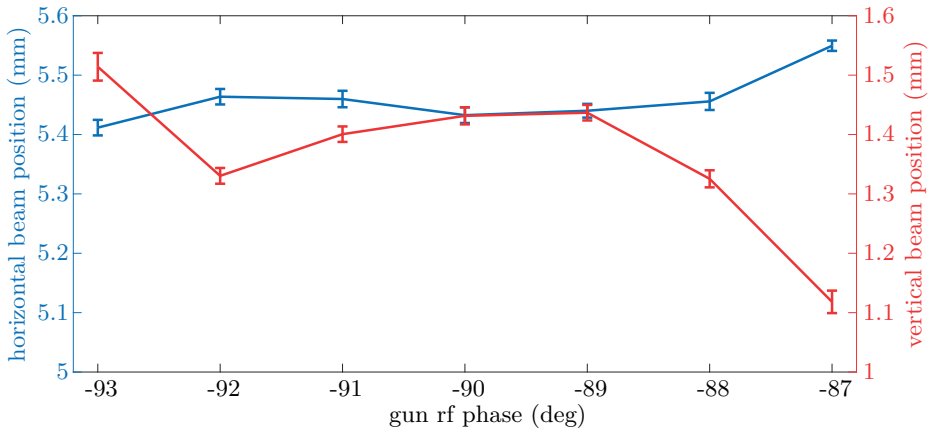

Figure 6.3: Result of the beam-based alignment of the laser spot w.r.t. the centre of the rf field. The plot shows the electron beam centroid position for different gun rf field phases, while the focusing solenoid is off. The position of the laser spot on the cathode is shifted, until the beam movement during the phase scan is minimised. A position movement of $\sigma_x = 0.04\,\text{mm}$ and $\sigma_y = 0.12\,\text{mm}$ is remaining.

19.06 MeV/c. The electron beam alignment with the gun cavity, the solenoid magnet, and the booster cavity is optimised using beam-based procedures. This reduces the beam transverse and longitudinal coupling due to dipole kicks in rf and solenoid magnet, minimising the transverse emittance growth.

The alignment between electron beam and rf fields is checked by observing the electron beam movement on a screen when varying the rf phases. The beam-based alignment is done independently for both rf cavities. It is iteratively improved by changing the position of the laser spot on the cathode, and changing the settings of corrector magnets upstream the booster, until the beam movement due to phase changes is minimised. The beam-based alignment of the laser spot w.r.t. the gun cavity rf fields is depicted in Fig. 6.3, while the beam-based alignment of the electron beam with the booster fields is shown in Fig. 6.4. At PITZ, the electron trajectory through the booster cavity is improved until the peak-to-peak difference in the beam position is below 0.2 mm. This is the case in Fig. 6.4, where the booster rf phase is scanned over a range of 70 degree, indicating a proper beam trajectory.

Similarly, the alignment of the solenoid magnet itself is done by monitoring the electron beam position while varying the solenoid focusing strength. The solenoid magnet misalignment is reconstructed via simulation, and then iteratively improved by moving the solenoid magnet using micro movers [94]. The alignment of the solenoid magnet is done once when the gun cavity and solenoid magnets are installed, while the beam alignment to rf is done before every emittance optimisation.

After the laser and electron beam alignment, the multipole-like distortions in the main solenoid and space charge fields in the electron beam due to laser and cathode inhomogeneities are compensated by gun quadrupole magnets inside the solenoid to minimise the transverse emittance growth due to coupling between horizontal and vertical phase space by achieving a round and symmetric transverse beam distribution on a downstream screen. The gun quadrupole strength settings are iterated by an optimizer until the transverse beam profile after the booster minimises both the correlation $\langle xy \rangle$ and difference in horizontal and vertical rms beam size. Finally, the projected emittance was measured for different main solenoid currents I_{main} in both the horizontal plane and the vertical plane by doing a slit scan at the slit station EMSY1.

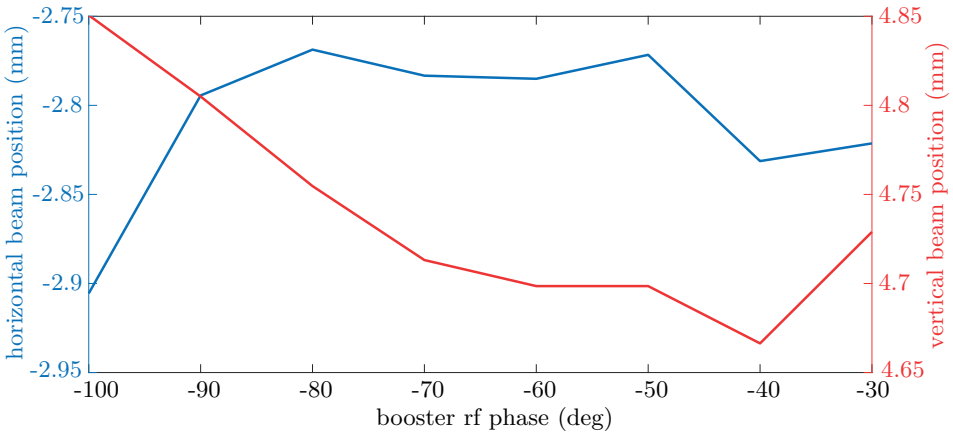

Figure 6.4: Final result of the beam-based alignment of the beam trajectory with the booster cavity rf fields. The booster rf phase is scanned around the on-crest rf phase, while the beam position downstream is monitored. The corrector magnets upstream the cavity are adjusted to minimise the beam movement. As the images, taken at a certain booster rf phase, are averaged in the first step, no statistical uncertainty is calculated. However, statistical uncertainties in beam position are small, see Fig. 4.7.

Figure 6.5 depicts the measurement result. The minimal projected emittance is $\epsilon_{xy} = \sqrt{\epsilon_x \epsilon_y} = (0.55^{+0.08}_{-0.07}\,(\text{syst.}))$ µm, achieved at the main solenoid current $I_{\text{main}} = 373$ A. The errors in emittance measurement are derived from the scaling factor, see Sec. 4.2.
Figure 6.6 shows the horizontal phase space, measured with the standard tool for the measurement of the projected emittance, the fastscan tool [26]. The Twiss parameters, determined with the same tool, are $\alpha_x = -0.68$ and $\beta_x = 3.68$ m. For the slice emittance measurement the beam was further transported to the first screen downstream the rf deflector (TDS). The beam orbit was tweaked to be centred through the quadrupole magnets High1.Q09 and High1.Q10, which were further on used to set up the slice emittance as discussed in Sec. 4.3. The magnets were set to $I_{\text{Q09}} = 4.20$ A and $I_{\text{Q10}} = -4.20$ A, to minimise the vertical beam size on the observation screen PST.Scr1. This improves the time resolution of the slice emittance measurement by reducing the vertical beta function at the observation screen, see Eq. 3.8.8. The horizontal focusing reduces the beam transport matrix element R_{12} from ~ 7 m to ~ 3.5 m, as discussed in Sec. 4.3, to improve the signal-to-noise ratio of the beamlet images, which are limited to up to 3 electron bunches, restrained by the short TDS rf pulse length. The horizontal beam optic was probed via beam trajectory response measurement from the corrector magnet High1.St1 to the observation screen PST.Scr1. The horizontal transfer matrix elements R_{11} and R_{12} from the slit mask to the measurement screen PST.Scr1 will be solved using a thin-lens model for the quadrupole doublet of High1.Q09 and High1.Q10. The measured R_{11} is 0.33 and R_{12} is 3.61 m. The transverse beam profile at the slit mask is shown in Fig. 6.7. Overall, the beam core is round, while the total beam profile is slightly asymmetric, due to an elliptic halo around the high-intensity core. The roundness of the electron beam at the slit mask is the result of the applied gun quadrupole magnets to correct the quadrupole-like field error in the main solenoid magnet, as mentioned earlier. During the slit scan, the slit mask was moved over a distance of 2.5 mm in steps of 50 µm, covering 51 slit positions in total. The TDS-deflected beamlet images were observed at PST.Scr1 at each slit position. The superposition of all beamlet images is shown in Fig. 6.8 next to the TDS-deflected electron

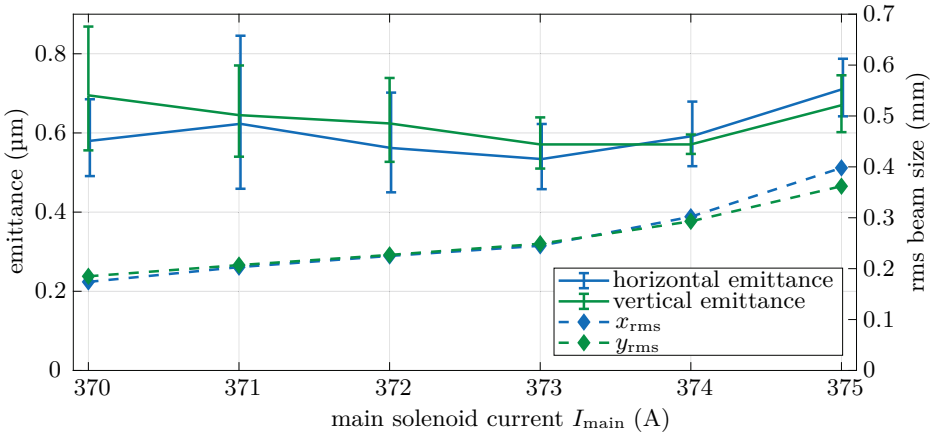

Figure 6.5: Projected emittance (solid lines) and rms beam size (dashed lines) measured with the slit scan tool for the 250 pC electron beam. The blue lines correspond to horizontal properties and the green lines to vertical properties. The minimal projected emittance is $\epsilon_{xy} = (0.55^{+0.08}_{-0.07}\,(\mathrm{syst.}))$ µm at the main solenoid current $I_{\mathrm{main}} = 373$ A. The error bars show the systematic error, derived as described in Sec. 4.2.

beam without the slit mask inserted. If the beam transport had only been dependent on externally applied fields, both images should have been equal. This is however not the case, as the full electron beam was defocused in the horizontal plane during the transport due to transverse space charge forces, leading to a wider horizontal beam size.
The defocusing is also occurring in the vertical plane, worsening the temporal resolution due to the larger vertical beam size. However, the main contribution to the vertical beam size on the observation screen is given by the rf deflection of the electron beam when the TDS is operated, so that vertical widening is not observed.
Figure 6.9 shows three beamlet images, taken at the centre of the beam, as well as at slit positions ±0.35 mm off the centre of the electron beam. While the beamlet at the centre slit position is horizontally symmetric and has a smooth longitudinal profile, the beamlet images at the halo region have a quite different shape: The beamlet image consists of two to three different beams, which are not connected, or only bridged with lowest charge density. The overall image intensity is low compared to the centre beamlet. Additionally, the dotted lines show along which lines the beamlet images are cut, in order to calculate the slice properties. The beamlet images are cut into eleven slices by default. With a good, i.e. small, time resolution, the images can be cut into thinner, i.e. more slices. During this experiment, however, the time resolution has not been determined. Nonetheless, the slice width is large compared to the vertical scale, on which the beamlet images change. This suggests, that more than eleven slices are resolvable.

The measured slice emittance curve, the mismatch parameter, and current profile are depicted in Fig. 6.10. In total, the measurement was done three times. The shown emittance values describe the average slice emittance, while the error bars describe the peak-to-peak slice emittance among the three measurements, i.e. the peak-to-peak error bar.
The centre slice shows a slice emittance of $\epsilon_0 = (0.69\,^{+0.05}_{-0.03}\,(\mathrm{stat.}))$ µm in the measurement. The slice emittance is highest in the centre slices, and drops to lower values at the head and tail.
Since no design beam optic is used, the mismatch parameter along the electron beam is calculated against the projected phase space, as described in Eq. 2.6.1. If the slice Twiss parameters are the same as the Twiss parameters of the projected phase space the

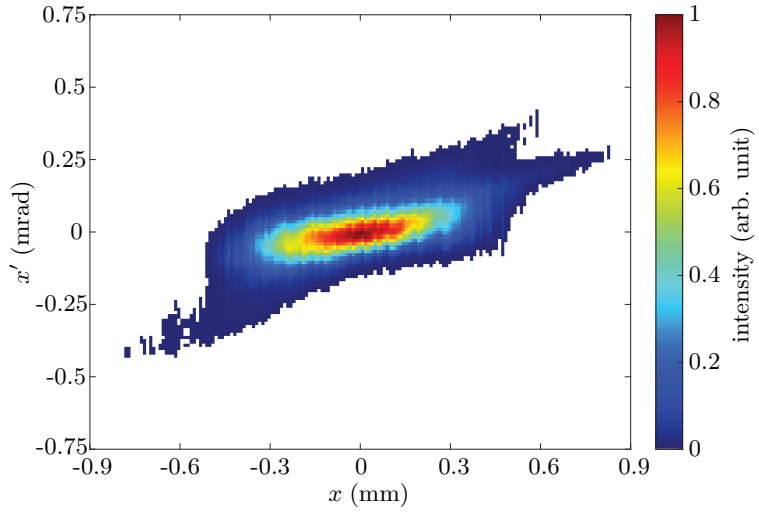

Figure 6.6: Projected, horizontal phase space of an electron beam generated from a temporal Gaussian laser shape, measured using the slit-scan technique (fastscan). The bunch charge is 250 pC. The projected, horizontal emittance at $I_{\mathrm{main}} = 373\,\mathrm{A}$ is $\epsilon_x = (0.53^{+0.09}_{-0.08}\,(\mathrm{syst.}))$ µm. During the scan 12 electron bunches were used at every slit position to measure the divergence.

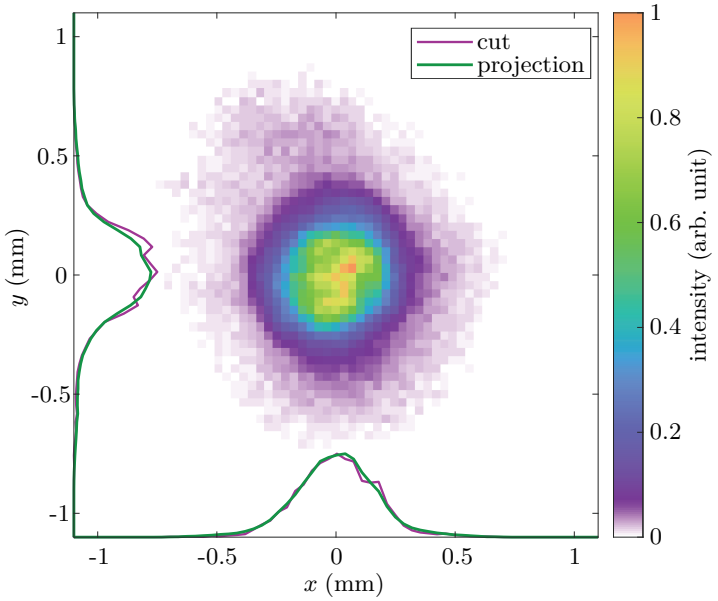

Figure 6.7: Beam spot at the slit position at $I_{\mathrm{main}} = 373\,\mathrm{A}$. The electron bunch has a charge of 250 pC and was created with a laser pulse of 6.0 ps (FWHM) temporal Gaussian shape. The electron beam has a horizontal rms width of (0.174 ± 0.003) mm and a vertical rms size of (0.202 ± 0.002) mm. For this image, three electron bunches from the same train were used.

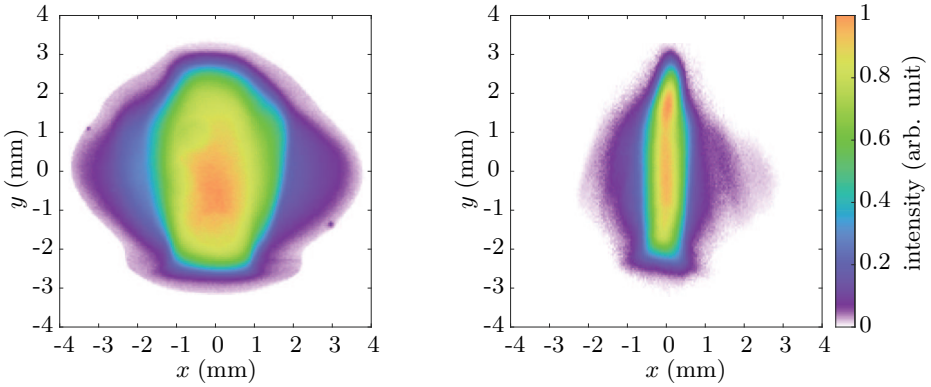

Figure 6.8: Image of TDS-deflected electron beam on the beamlet observation screen PST.Scr1 (left) and superposition of the deflected beamlet images at all slit positions (right). Three electron bunches were used for the left image, while three electron bunches at every slit position were used in the right image.

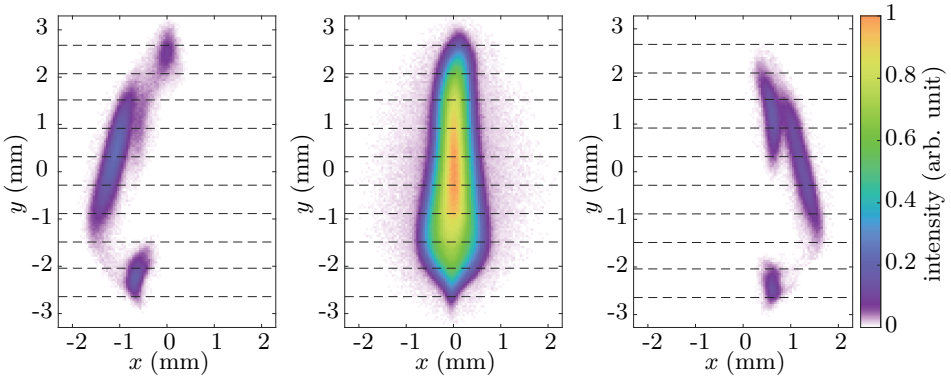

Figure 6.9: Filtered images of the streaked beamlets at three different slit positions on PST.Scr1. The outer beamlet images were taken when the slit was moved by 0.35 mm from the centre position.

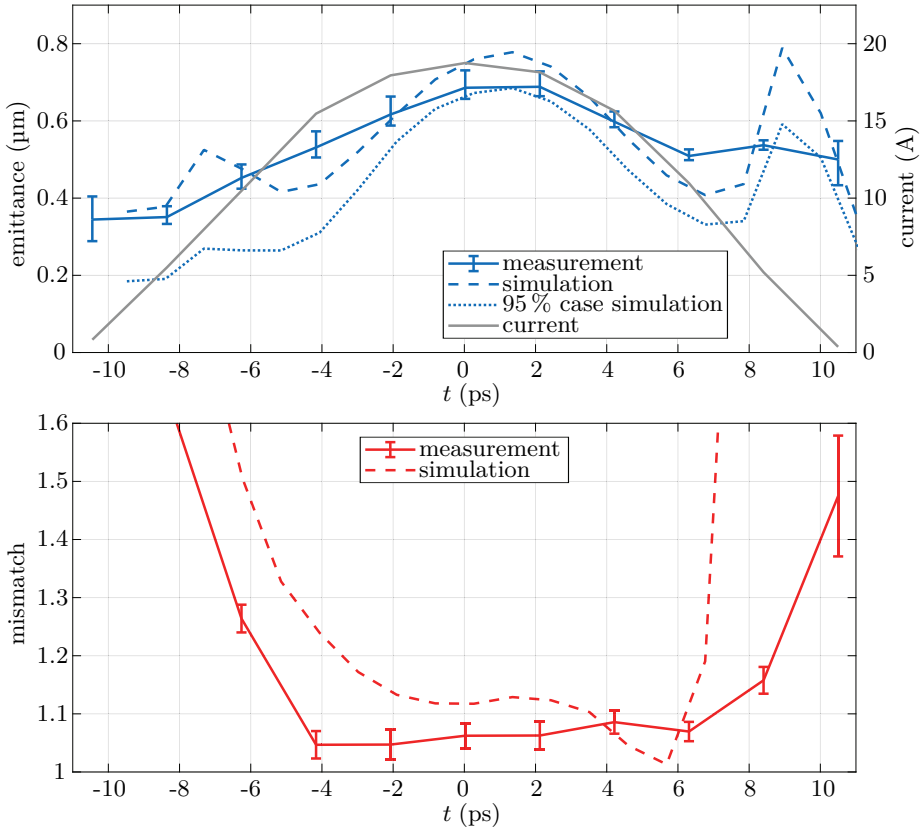

Figure 6.10: Measured slice emittance (solid blue), simulated slice emittance (dashed blue), the simulated slice emittance curve where only 95 % of the most contributing macro particles are considered (blue dotted line), measured mismatch curve (red), simulated mismatch curve (dashed red) and measured current profile (grey) of an electron beam with 250 pC, created with a laser pulse with a 6.0 ps FWHM temporal Gaussian shape. The measured slice emittance curve agrees well to the simulation in the centre, while agreeing better with the charge-reduced simulation curve in the tails. The error bars depict the peak-to-peak error between several measurements. The measured mismatch curve shows a small mismatch in the centre, which grows rapidly in the head and tails, although the growth is closer to the centre in the simulation.

mismatch parameter equals 1.0. In the range −4 ps to 6 ps a mismatch parameter of 1.05 is achieved. The slices closer to the head and tail however have a much higher mismatch parameter due to the mismatch of solenoid focusing and lower space charge forces.
The dashed curves in Fig. 6.10 illustrate the slice emittance and mismatch curve, obtained from an ASTRA simulation of the beam transport from cathode to the slit station. In the simulation, a laser pulse with a temporal Gaussian intensity envelope is used, with a FWHM pulse length of 6 ps. The emission process contributes significantly to the (slice) emittance formation. Therefore the macro particle distribution assumed in simulation must be close to the beam distribution achieved in experiment. However, mirror charges during the emission can only be included in the ASTRA simulation when cylindrically-symmetric space charge forces are considered. This means that the transverse laser pulse shape in ASTRA is tweaked to have the same radial charge distribution as the radial laser pulse shape, retrieved from the laser pulse shape shown in Fig. 6.1. The resulting transverse laser pulse profile corresponds to the core + halo model [95]. Here a high-intensity core, which largely follows the flattop distribution, is surrounded by a low-intensity ring, the so-called *halo*. Diffraction rings might be included in the transverse simulation laser profile as well, when they are centred in the transverse laser pulse profile. The measured transverse laser profile, as well as the distribution used in the ASTRA simulation are both shown in Fig. 6.1.
The electric field strength in the gun and booster cavity have been tweaked to achieve the same beam energy as in the experiment.
The simulation is done for different solenoid field strengths. In the simulation, a minimal projected emittance of 0.79 µm is reached at the solenoid current of 361 A, i.e. 12 A less than found experimentally, see Fig. 6.5. A possible reason for the difference is a discrepancy in the solenoid calibration. The slice emittance and mismatch curve, based on the simulation at 361 A, is shown in Fig. 6.10, next to the measured slice emittance curve. Since the shear parameter has not been determined, a direct comparison of temporal beam properties cannot be done. However, the temporal axis of the measured properties is scaled, so that the simulated and experimentally determined current profiles overlap.
The simulated slice emittance curve shows 10 % higher emittance values in the bunch centre. This might be due to the finite signal-to-noise ratio (SNR), which does not allow to detect 100 % of the bunch charge, therefore underestimating the measured slice emittance. The simulated slice emittance curve shows bumps close to the head and tail, before the slice charge drops to zero. This behaviour cannot be observed in the measurement curve. Measurements however show a lower emittance near the head and tail, due to the lower charge content, which leads to a smaller SNR.
The overall shapes of the simulated and measured mismatch curves are similar. Both the experimental and simulated mismatch curves show a good matching of the slice phase spaces to the projected phase space for the slices around the centre, and grow rapidly for head and tail slices. This is due to over-focusing of these slices with the solenoid magnet: The solenoid magnet is used to focus the electron beam leaving the electron gun. The head and tail slices however have a lower charge content, therefore the defocusing transverse space charge forces are smaller, leading to over-focusing, when the solenoid magnet is optimised to focus the centre slices.
Compared to the experimental curve, the increase in mismatch of the simulated bunch is more rapidly. A possible reason for the discrepancy might be caused by a measurement artefact: Due to the finite SNR in experiment, the tails of the charge distribution might be not correctly measured, leading to an underestimation of the actual bunch length. Fitting the simulated bunch profile to the shortened experimental bunch profile would stretch both the simulated slice emittance and mismatch curve in Fig. 6.10.
Figure 6.11 illustrates the phase space of the whole beam, i.e. the projected phase space,

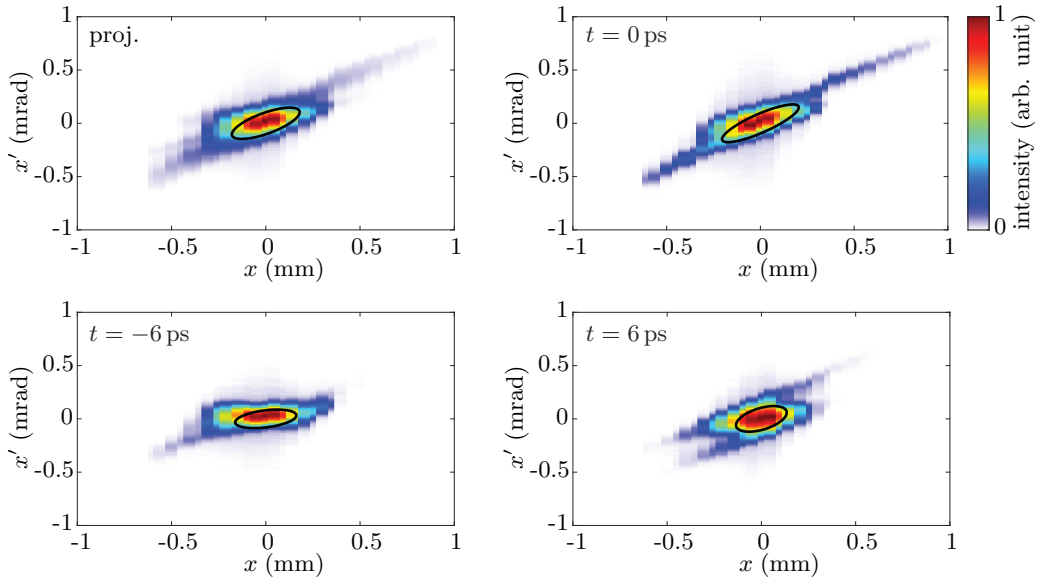

Figure 6.11: Projected phase space (top left), centre slice phase space (top right), and the slice phase space at −6 fs and 6 fs in the bottom row. The black ellipses depict the equivalent rms phase space ellipses.

the centre slice phase space ($t = 0$ fs), as well as the phase space of the slice at −6 fs and 6 fs. Additionally, the equivalent rms phase space ellipse, see Eq. 2.2.8, is shown in black. The projected phase space is reconstructed by overlapping all slice phase spaces. It shows a dense core between −0.35 mm and 0.35 mm, while exhibiting low-density regions further outside. The measurement with fastscan, the standard projected emittance tool, see Sec. 4.2, shows an emittance of $\epsilon_x = (0.53^{+0.09}_{-0.08}\,(\text{syst.}))$ µm. The slice emittance was measured in total three times. The projected emittance, determined with the slice emittance measurement tool, shows a projected emittance of 0.63 µm, 0.63 µm and 0.69 µm, where the statistical rms uncertainty is always below 0.01 µm. On average this yields a projected emittance of $\epsilon_x = 0.65^{+0.04}_{-0.02}$ µm, where the errors are the peak-to-peak limits of the measured values.

The main reason for the discrepancy between both measurements is the different image processing procedure, used to treat the beamlet images. Both image processing procedures utilise a noise cut, in which pixels below a threshold are discarded. In the projected emittance software, this threshold is 3σ, while being only 1.5σ when analysing the images during slice emittance measurements, see Sec. 4.5. Furthermore, the measurements differ in drift length, screen station, screen material, and the scaling of the projected emittance value in case of the projected emittance measurement analysis in fastscan, as described in Sec. 4.2. The slit width chosen for both the projected and slice emittance measurements is 50 µm.

For the time-resolved emittance measurement the beam has to be streaked with the rf deflector, which only allows for a moderate SNR compared to projected emittance measurements, due to the short TDS rf pulse length. The quadrupole magnets used for focusing increase the SNR by a factor of $7\,\text{m}/R_{12} \approx 2$, diminishing the sensitivity problem from lower SNR.

A comparison of the results, achieved with both tools, is given in Table 6.1. For the projected emittance, measured with the standard tool for projected emittance, systematic errors, derived from the different beam size, measured with the slit scan, and with the

Table 6.1: Comparison of beam properties, measured with the fastscan tool and the SlitScanner tool. Both measurements were taken at the slit position EMSY1. The error given for the projected emittance measured with the fastscan tool is derived from the fraction of the beam size of the phase space and the beam directly measured at the slit position, see Sec. 4.2. The results listed are from a single projected emittance measurements. The uncertainties given in the SlitScanner column are rms errors, derived as described in Sec. 5.3.

Beam property		unit	Fastscan	SlitScanner
Projected emittance	ϵ_x	µm	$0.53\ ^{+0.09}_{-0.08}$	0.69 ± 0.01
Screen beam size	x_{rms}	mm	0.245	0.174 ± 0.003
Phase space beam size	x_{rms}	mm	0.210	0.180 ± 0.001
Beta function	β_x	m	3.68	1.74 ± 0.01
Alpha function	α_x	-	-0.68	-1.01 ± 0.01

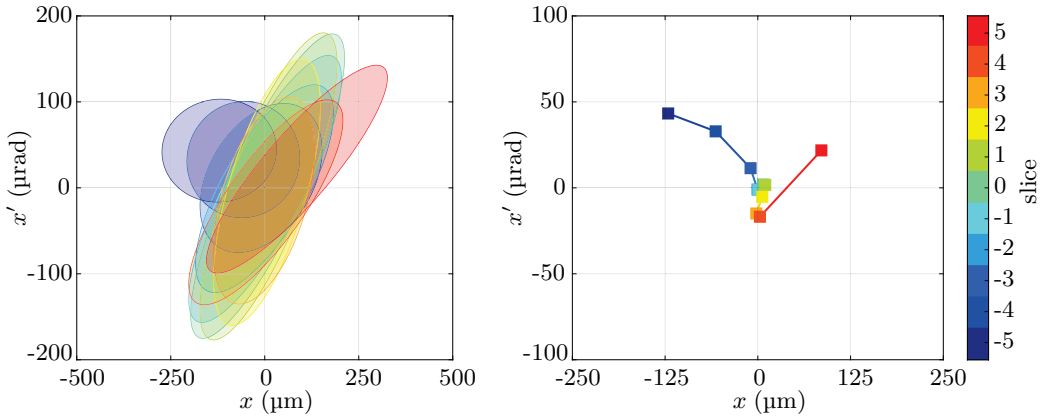

Figure 6.12: Slice phase space rms ellipses (left) and slice centroids (right) of an electron beam. The phase space and centroid positions were calculated from a single slice emittance measurement. During the measurement ten statistical beam images were taken, allowing calculation of a statistical rms uncertainty. The statistical uncertainty is negligible for this results.

scintillator screen directly at the slit station. Comparing the upper error limit of the projected emittance from Fastscan shows a difference of 0.07 µm to the projected emittance, reconstructed during slice emittance measurements. The beam sizes differ strongly between both measurements. The reason is a drift in beam properties during both measurements. An analysis of the screen image at EMSY1, taken for the Fastscan measurement, with the image processing procedure developed for slice emittance measurements, reveals a horizontal beam size of (0.240 ± 0.002) mm. As the beam sizes are strongly changed, also the Twiss functions are different.

The rms slice phase space ellipses, together with the slice ellipse centroids are shown in Fig. 6.12. The largest mismatch and misalignment are given by the head and tail slice. These however contribute least to the projected emittance, due to the low charge in these slices. Table 6.2 displays the different slice phase space contributions to the projected rms emittance according to Eq. 2.5.1. The slice emittance has the biggest contribution to the projected emittance: An amount of

$$\frac{\epsilon^2_{\mathrm{slice}}}{\epsilon^2_{\mathrm{Proj}}} = 81\,\% \tag{6.1.2}$$

Table 6.2: Decomposition of the measured and simulated transverse phase space of an electron beam. Additionally, the emittance decomposition is done for the full electron beam and the beam within the FWHM limits of the current profile. The misalignment emittances observed in simulation are artefacts based on numerical noise.

	Measurement		Simulation	
	full beam	±FWHM/2	full beam	±FWHM/2
Projected emittance	0.69 µm	0.68 µm	0.79 µm	0.69 µm
Slice emittance	0.62 µm	0.64 µm	0.59 µm	0.60 µm
Mismatch emittance	0.28 µm	0.25 µm	0.52 µm	0.30 µm
Linear misalignment emittance	0.14 µm	0.05 µm	0.01 µm	0.01 µm
Non-linear misalign. emittance	0.01 µm	< 0.01 µm	< 0.01 µm	< 0.01 µm

of the projected emittance is contributed from the charge-weighted, averaged slice emittance, see Eq. 2.5.1. The mismatch only contributes to 16 % of the projected rms emittance. Additions by linear and non-linear misalignment emittance values are small and negligible. These values are minimised by the beam alignment procedure before emittance measurements.
Table 6.2 shows not only the emittance decomposition of the measured slice phase space, but also of the simulation. Considering the full beam, a 15 %-higher projected emittance and a 86 %-higher mismatch emittance are calculated. The slice emittance values are comparable. The measured linear misalignment emittance does not significantly contribute to the projected emittance, it only makes up

$$\frac{\epsilon^2_{\text{linear misalignment}}}{\epsilon^2_{\text{Proj}}} = 4\,\% \tag{6.1.3}$$

of the projected emittance. In simulation however, this properties vanishes almost completely. This is due to the perfect symmetry of magnetic and rf fields, and symmetric alignment of the fields w.r.t. the electron trajectory, assumed in the simulation.
Overall, the discrepancy between the mismatch emittance of the measurement and simulation is striking. A possible reason is again issues arising from the limited signal strength in the tails of the distribution. For a more robust comparison, only particles within the ±FWHM/2 are considered for the calculation of the projected emittance, and the temporal emittance contributions. Here, both measurement and simulation show a matching projected emittance, as well as similar time-resolved emittance contributions. This result suggests, that a high SNR is critical for a meaningful comparison of measurements and simulations. A good agreement between simulation and measurements within the high-current region of the electron beam is more important than the full-beam comparison because the high-charge part gives the main contribution to free-electron lasing.

6.2 Longitudinal and Transverse Flattop Profile

Laser pulses with a temporal and transverse flattop profiles require a more sophisticated laser pulse shaping stage in the laser system, which reduces non-linearities in the transverse space charge forces and induced growth of angular spread, yielding a smaller rms beam emittance compared to electron beams from temporal Gaussian laser pulses with a transverse flattop shape. Characterisation of the projected emittance of beams, created with laser pulses with longitudinal flattop profile have already been performed in 2012

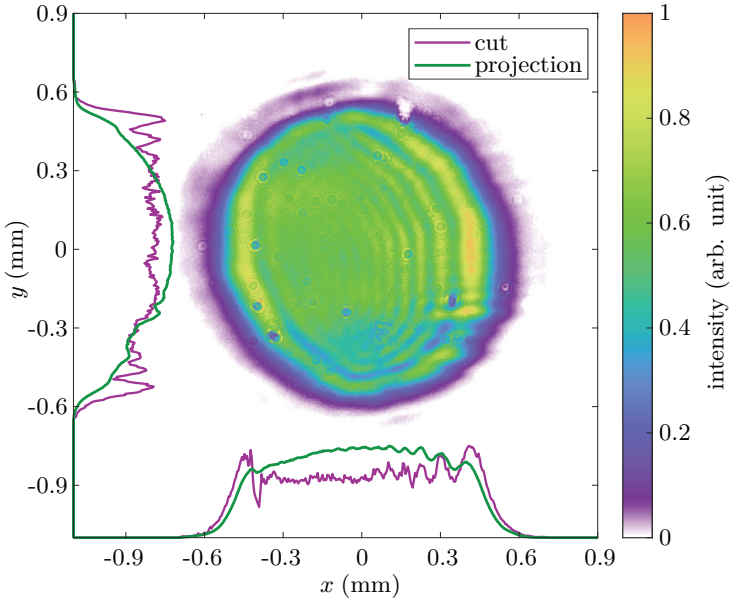

Figure 6.13: Transverse laser profile on the cathode. The iris was set to a diameter of 1.1 mm, yielding a horizontal rms size $\sigma_x = 0.277$ mm and a vertical rms beam size of $\sigma_y = 0.268$ mm. The projection of the laser profile on the horizontal and vertical axis is shown in green, while the cut though the intensity profile at (0,0) is shown in purple.

[25]. Now we are also able to measure the slice emittance of such an electron beam with high temporal resolution. The measurements are performed with the PHAROS laser, see Sec. 3.2.2. Temporal laser pulse shaping is performed with spatial light modulators. The transverse flattop shaping of the laser pulses is achieved in the same manner as for the MBI laser system, i.e. cutting out a central part of a transversely Gaussian beam profile with an aperture. The beam shaping aperture was set to a diameter of 1.1 mm during the measurements. The transverse laser profile is shown in Fig. 6.13. The transverse laser profile achieved during this shift shows a higher intensity modulation of the central part due to diffraction rings than the transverse laser profile used to create the temporal Gaussian, radial flattop profile. The horizontal and vertical intensity profile through the centre of the laser profile (cut, purple lines) exhibits the amplitudes of the modulation. The laser profile shows a so-called *halo* around the centre, i.e. an extended low-intensity distribution beyond the ideal hard-edge boundary. The horizontal rms beam size is $\sigma_x = 0.277$ mm and the vertical rms beam size is $\sigma_y = 0.268$ mm, while an ideal flattop profile with 1.1 mm diameter has an rms beam size of 0.275 mm.
The PHAROS laser system does not have a reliable optical diagnostics to measure its temporal pulse shape, so a 5 pC-electron beam replica of the laser pulse by photoemission is guided to the rf deflector in the PITZ beamline to measure its temporal distribution. Figure 6.14 depicts the longitudinal bunch profile at low charge. The uncertainty in the amplitude is derived from the rms fluctuations. The current profile shows a flattop profile, with finite rise and fall time, as well as modulation of the current profile on the plateau. The intensity modulations on the plateau are bigger than the modulation of the profiles achieved at PITZ with the MBI laser, shown in Ref. [25].
The measurement of the temporal bunch profile is recreated in ASTRA with varying laser pulse length and rise and fall times of the laser profiles. The simulated temporal bunch profile, which quite matches the measured profile, is shown in Fig. 6.14. A laser pulse, with

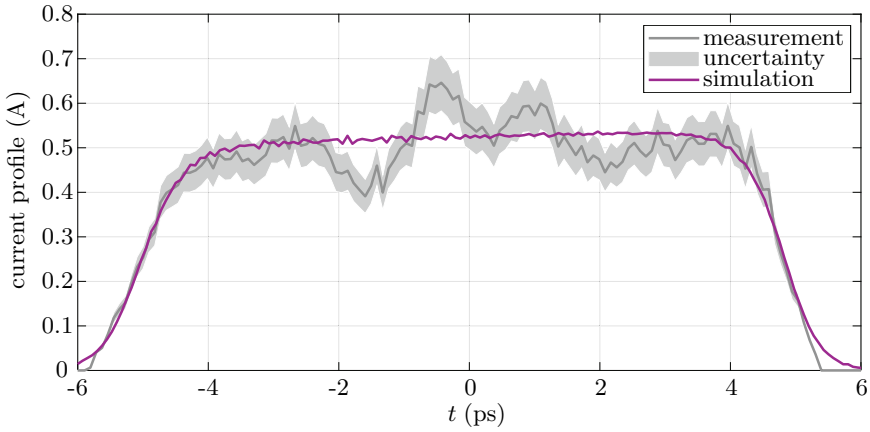

Figure 6.14: Temporal current profile of the electron beam with 5 pC. The simulation with a temporal flattop laser pulse, with a FWHM pulse length of 10.4 ps with rise and fall times of 1.2 ps yields a temporal bunch profile, matching the length, rise and fall time of the measured profile. The simulated electron current profile has a FWHM length of 9.74 ps. The measured profile exhibits modulations, which have not been included in the simulation.

a FWHM pulse length of 10.4 ps and a rise and fall time of 1.2 ps leads to this simulation result. No intensity modulation was applied to the simulated laser pulse profile, therefore both profiles show differences here.
For the 250 pC emittance measurements, the gun and booster are set to a similar rf amplitude and phase as in Ch. 6.1, i.e. $p_{\mathrm{Gun}} = 6.28\,\mathrm{MeV}/c$ and $p_{\mathrm{Boo}} = 19.44\,\mathrm{MeV}/c$ after gun an booster respectively with MMMG and on-crest acceleration phases.
The projected emittance is optimised by means of the solenoid magnet. Slits with 50 µm-wide opening were used, while the beamlets were observed on a LYSO screen at the screen station High1.Scr5. The result is shown in Fig. 6.15. At the solenoid current of 370 A a minimal projected emittance of $\epsilon_{xy} = \sqrt{\epsilon_y \epsilon_y} = (0.54 \pm 0.05\,(\mathrm{syst.}))$ µm is achieved. The given error is estimated from the scaling factor of the projected emittance.
The horizontal phase space, measured with the standard slit scan tool (fastscan), is depicted in Fig. 6.16. At the solenoid current of 370 A a beta function of $\beta_x = 7.69\,\mathrm{m}$ at the slit mask is yielded, while the alpha function is $\alpha_x = -1.37$ according to the measurement with the fastscan tool. This transverse phase space yields the same transverse emittance than that of the electron beam from a temporal Gaussian laser pulse, shown in Fig. 6.6. A reason might be the transverse laser pulse size at the cathode, which could not be optimised for lowest emittance. For the temporal Gaussian laser pulse shape, a beam with 1 mm diameter was used. As the temporal flattop laser pulse shape should linearise the space charge forces of the emitted electron beam, the laser spot size at the cathode should be smaller or the same. However, as the laser power was limited during the experiment, the iris in the laser beamline was increased to extract a bunch charge of 250 pC. For this, the diameter of the transverse laser pulse shape was set to 1.1 mm.
The electron beam at the slit position is depicted in Fig. 6.17. The image shows a round beam without any significant halo around the beam. This is quite in contrast to the electron beam profile illustrated in Fig. 6.7, which shows a large halo, particularly in the vertical plane.
Afterwards the optics is set up for the slice emittance measurement. For this, the quadrupole magnets High1.Q09 and High1.Q10 are set to currents of $I_{\mathrm{Q09}} = 4.00\,\mathrm{A}$ and $I_{\mathrm{Q10}} = -4.00\,\mathrm{A}$, respectively. This yields the horizontal transport matrix elements

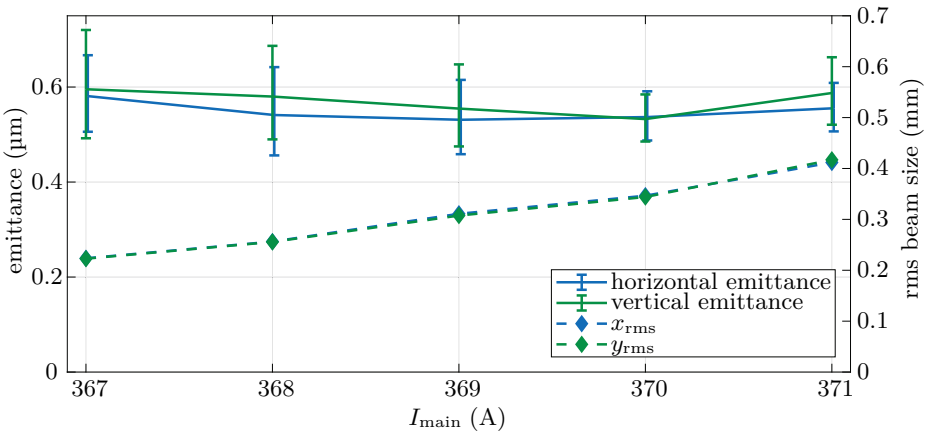

Figure 6.15: Measurement of the horizontal and vertical projected emittance for different solenoid currents. The electron beam has a temporal flattop profile and a bunch charge of 250 pC. The projected emittance minimum was found at $I_{\mathrm{main}} = 370\,\mathrm{A}$, where an emittance of $\epsilon_{xy} = (0.54 \pm 0.05\,(\mathrm{syst.}))$ µm was measured. Both the measured rms beam size and emittance are very similar in both transverse planes, i.e. the beam has an excellent roundness.

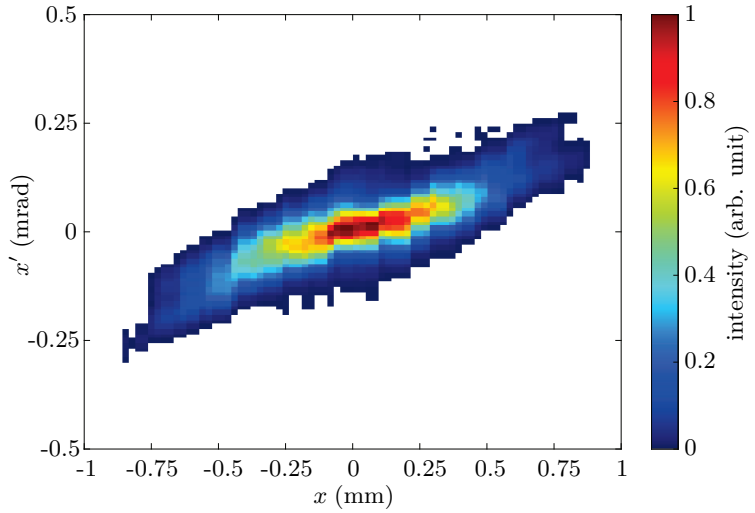

Figure 6.16: Projected phase space of an electron beam with a bunch charge of 250 pC, created from a temporal flattop laser pulse with 10.4 ps pulse length. The projected, horizontal emittance at $I_{\mathrm{main}} = 370\,\mathrm{A}$ is $\epsilon_x = (0.53 \pm 0.05\,(\mathrm{syst.}))$ µm, where the error is a systematic error, derived from the beam size measured in the slit scan and directly with a scintillator screen at the slit position, see Sec. 4.2. It was determined with the fastscan tool. For more details on the fastscan compare with Sec. 4.2.

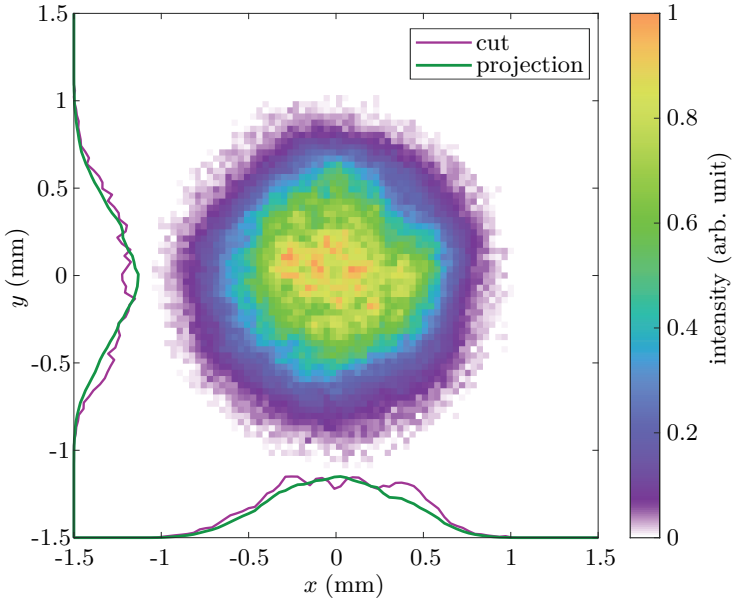

Figure 6.17: Beam image at the slit position. The solenoid magnet was set to $I_{\text{main}} = 370\,\text{A}$, since this value yields the minimal projected emittance. The beam has a horizontal rms size of $\sigma_x = (0.342 \pm 0.005)\,\text{mm}$ and a vertical rms beam size of $(0.341 \pm 0.004)\,\text{mm}$

$R_{11} = 0.33$ and $R_{12} = 3.66\,\text{m}$ from the slit mask to the observation screen. The electron beam, sheared vertically with the TDS, is shown in Fig. 6.18. The streaked bunch shows a much more uniform horizontal beam size along the beam compared to the temporal Gaussian case, see Fig. 6.8. A reason should be the reduced mismatch of space charge defocusing in the tails, due to the longitudinal pulse shaping. The superposition of all filtered beamlet images after deflection is shown on the right side of Fig. 6.18. As in Sec. 6.1, the superposition of the beamlets shows a much smaller size than the full beam. Due to the use of the slit mask the transverse space charge forces are reduced, while the full beam experiences stronger space charged forces which defocus the beam more.
Figure 6.19 shows the images of three beamlets, as well as their slicing for the calculation of time-resolved beam properties. The beamlet shown in the centre is taken close to the centre of the beam, while the beamlets left and right next to it are taken at slit positions with 0.6 mm offset in both directions, see Fig. 6.19.
The shown beamlet images have all similar vertical length, i.e. the electron beam does not show strong variations in the horizontal beam size along the bunch at the slit mask. Moreover the off-centre position beamlets exhibit a tilt in the x-y-plane on the observation screen. This is equivalent to a tilt in the x'-z-plane of the beamlets at the slit position, which is caused by Twiss parameter mismatch between different slices. For calculation of the time-resolved beam properties, the beam images are cut into 11 slices of $\sim 2\,\text{ps}$. The slice emittance is plotted in Fig. 6.20. The solid blue line shows a flat slice emittance profile, with an emittance of $(0.50 \pm 0.01)\,\mu\text{m}$ at the centre slice and similar emittance along the bunch, which drops slightly at the tail to a slice emittance value of $(0.34 \pm 0.03)\,\mu\text{m}$. The slice emittance was measured twice, where the plotted values show the average between both measurements, and the error bars the peak-to-peak span of the measured values. The values of both measurements are close to each other for all slices but the head, where the slice emittance is $(0.44 \pm 0.10)\,\mu\text{m}$.
Besides the measurement, the dashed blue line shows the slice emittance, calculated from

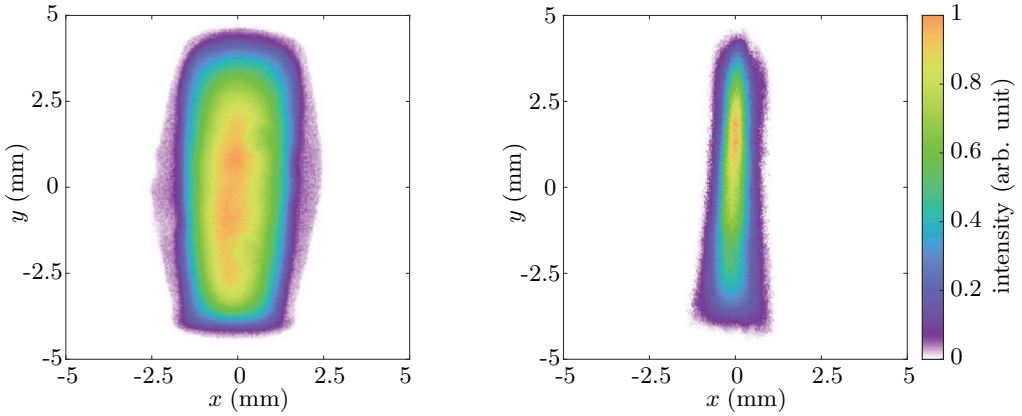

Figure 6.18: Image of the full TDS-deflected flattop electron beam on the left, in comparison with the beamlet images, taken at all slit positions and then overlapped (right). The reduced space charge forces after the slit mask lead to a lower space-charge-induced correlation term $\langle xx' \rangle$, leading to a smaller horizontal beam size.

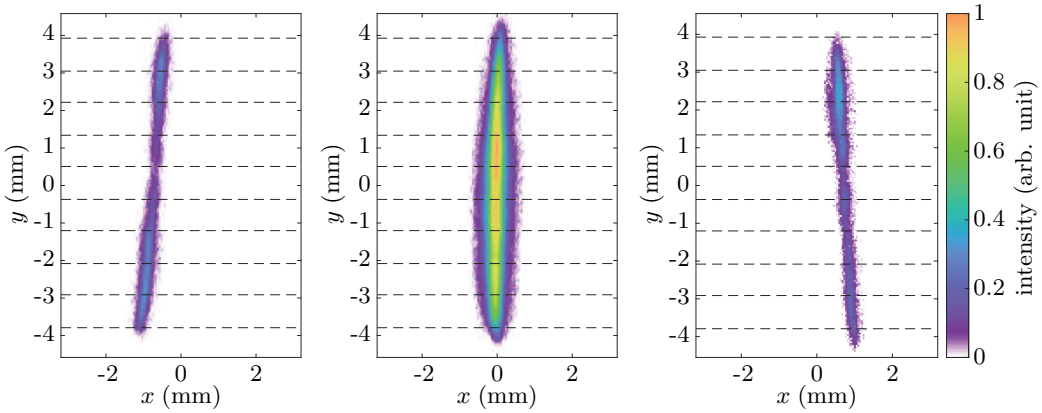

Figure 6.19: Filtered beamlet images on the observation screen, after deflection with the rf deflector. The two outer beamlet images were taken at slit positions 600 µm off the position of the shown, central beamlet.

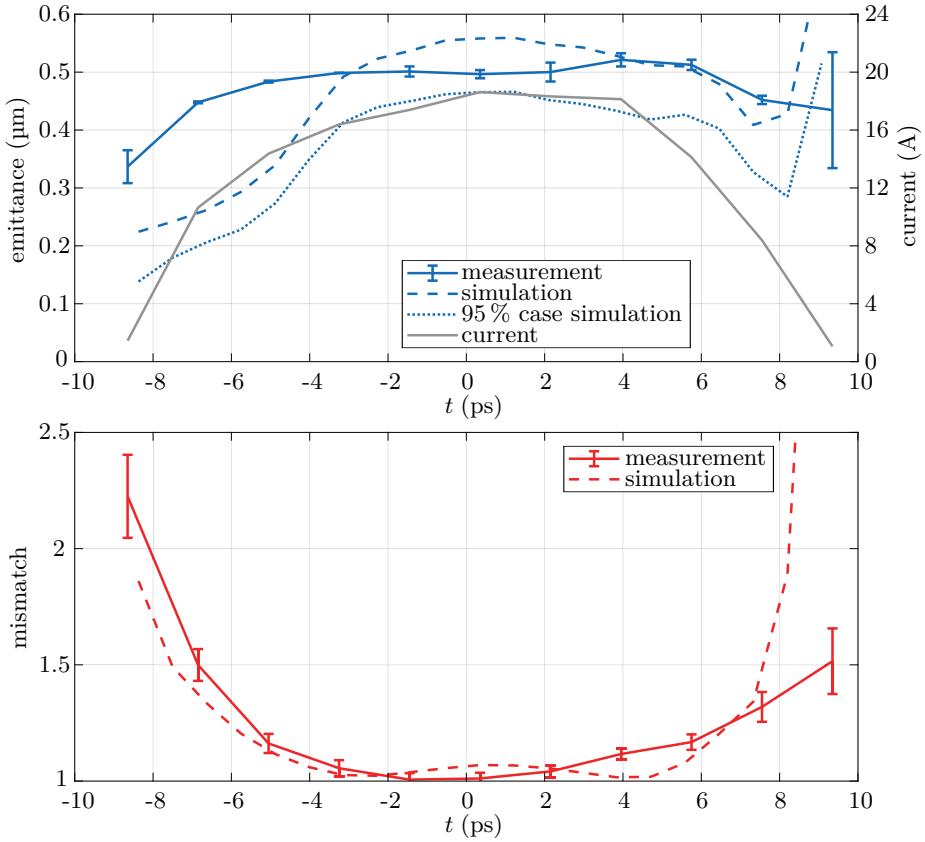

Figure 6.20: Measured slice emittance (solid blue), simulated slice emittance (dashed blue), simulated slice emittance curve only considering 95 % of the charge (dotted blue), and mismatch curve (red line) along the bunch. The slice emittance was measured twice; the slice emittance shows the average between both measurements, where the error bars indicate the peak-to-peak spread of the two measurements. The grey curve shows the bunch current. The slice emittance curve is flat along all slices; in the centre slice an emittance of (0.50 ± 0.01) µm is achieved. The mismatch curve is very close to 1.0, i.e. the optimum, for the centre slices. It is higher in the head and tail slices.

a beam transport simulation. The essence of the VC2 image was captured by the core + halo model [95] by using the same radial charge distribution in ASTRA simulation as in experiment, see Fig. 6.13. The pulse shape and length assumed in simulation are the same that have been found to match the temporal bunch profile shown in Fig. 6.14, i.e. 10.4 ps flattop pulse length, with a rise and fall time of 1.2 ps. The charge was set to 250 pC, as in experiment, while both the gun cavity phase and booster cavity phase were set to on-crest phase. In simulation, a beam momentum of $p_{\mathrm{Gun}} = 6.26\,\mathrm{MeV}/c$ was achieved behind the gun, which grew further to $p_{\mathrm{Boo}} = 19.88\,\mathrm{MeV}/c$ after the booster cavity.
The calibration of the vertical screen axis to temporal bunch axis was not done in the experiment. To compare both the experimental and the simulated slice emittance curve both temporal bunch profiles are compared. The time scaling of the measured value was chosen such that the measured and simulated bunch profile are matched.
The simulation shows a decent agreement with the measurement curve, although some differences between both curves are visible as well. In the centre, the simulation shows a slice emittance of 0.56 µm. The simulation curve shows a plateau in the centre, just like the measurement case, just that the plateau is shorter in simulation than in experiment.
Besides the slice emittance curves, Fig. 6.20 displays the measured and simulated mismatch curves. The mismatch parameter in measurement (red solid line) and simulation (red dashed line) show a remarkable agreement, showing only slight disagreement in the head and tails on a moderate level. The measurement shows a small mismatch parameter below 1.17 ± 0.04 between -5 ps and 5 ps. In the centre even a mismatch of 1.01 ± 0.02 is measured. The temporal flattop case shows a larger mismatch only at both tails, probably due to the rapid change in transverse space charge fields [46].
Figure 6.21 depicts the horizontal projected phase space in the top left subplot, as well as the centre slice phase space at the top right, and the slice phase space at ± 5.5 ps in the bottom row. Additionally the equivalent rms phase space ellipses are shown by black ellipses. The centre slice and projected phase space show similarity. Additionally, the phase space depicted in the bottom-left subplot shows a curvature, leading to an S-shape of the phase space. This however is not resembled by the equivalent slice phase space ellipse, which is tilted instead.
A comparison of projected beam properties, measured with the Fastscan tool (see Sec. 4.2) and with the slice emittance measurement tool is given in Fig. 6.3. The horizontal projected emittance, determined with both tools, is consistent with one another within the errors listed. For the beam properties, determined with the SlitScanner tool for slice emittance measurements, the listed uncertainty is the rms error. The error given for the projected emittance measured with the Fastscan tool is determined from the ratio of the beam size measured with the slit scan, and the beam size measured with a screen directly at the slit position. Both tools show the same horizontal beam size, measured on the screen at the slit position. The beam size, derived from the phase space however is larger during the projected emittance measurement. Therefore also the calculated beta function is larger in the measurement with the fastscan tool than it is in the slice emittance measurement. The alpha functions are also different.
The phase space ellipse of all slices, as well as the centroid positions in the phase space are given in Fig. 6.22. It shows, that the ellipses at the tail, coloured in blue, have a small correlation. Towards the centre the tilt in the phase space increases and stays quite similar for several slices, before the ellipses tilt further at the bunch head, which is shown in red. This reflects the mismatch curve, which shows good matching in the centre and larger mismatch at both tails. The plot of the slice centroid positions reveals misalignment of several ellipses. The presented error bars describe the rms uncertainty, which is particularly high at the head and tail centroid.
The time-resolved centroid positions, as well as the slice emittance and Twiss parameters

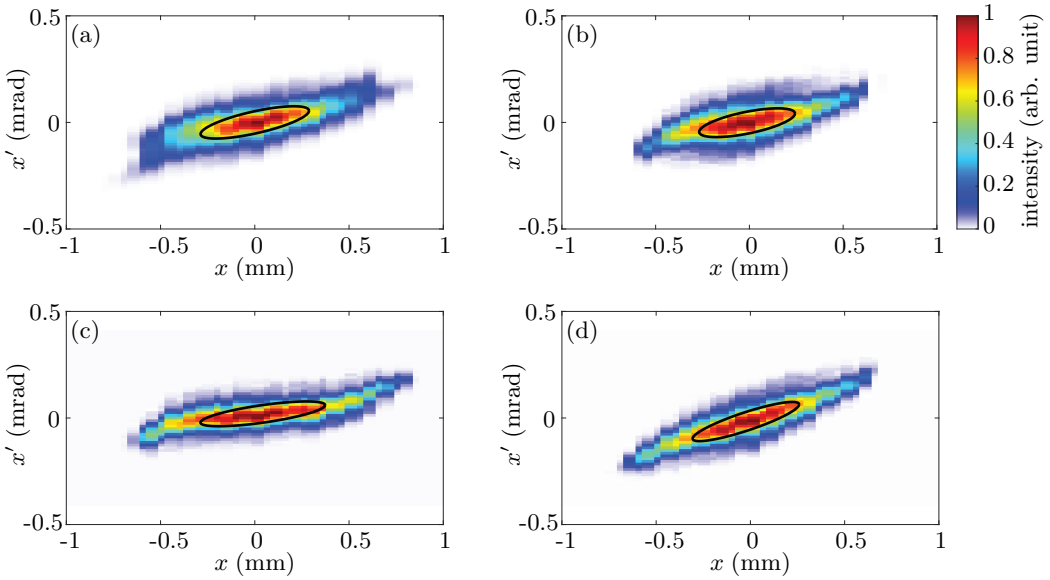

Figure 6.21: Transverse phase space of the electron beam, created with a 10.4 ps-long flattop laser pulse. The image (a) shows the projected phase space, determined during the slice emittance measurement. The image (b) shows the centre slice phase space, while (c) and (d) show the slice phase space ±5.5 ps from the centre. The rms phase space ellipses are shown in black.

Table 6.3: Comparison of beam properties, determined with the tool for projected emittance measurements versus the tool for slice emittance measurements. Both measurements were done at the slit station EMSY1. The projected emittance, determined with the two different measurement procedures, yield the same result, considering the errors. For the SlitScanner tool always a statistical rms uncertainty is listed, while the error given for the projected emittance measured with Fastscan is calculated from the comparison of the screen beam size and phase space beam size.

Beam property		unit	Fastscan	SlitScanner
Projected emittance	ϵ_x	µm	0.54 ± 0.05	0.58 ± 0.01
Screen beam size	x_{rms}	mm	0.347	0.342 ± 0.005
Phase space beam size	x_{rms}	mm	0.315	0.288 ± 0.001
Beta function	β_x	m	7.69	5.47 ± 0.06
Alpha function	α_x	-	-1.37	-1.04 ± 0.01

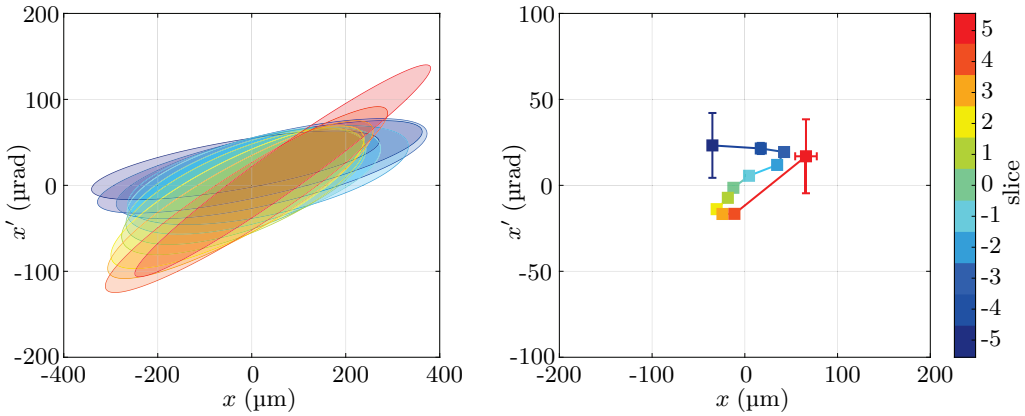

Figure 6.22: Measured rms slice phase space ellipses (left) and slice ellipse centroids (right). The electron beam had a temporal flattop shape, with a bunch charge of 250 pC. The figure shows the slice phase space ellipse and slice centroid position of a single slice emittance measurements. During the measurement ten statistical images were taken, which allows derivation of a statistical rms uncertainty. The error bars indicate the rms uncertainty.

Table 6.4: Decomposition of the projected rms emittance into the different slice phase space contributions. The slice emittance contributes most strongly to the projected emittance, followed by the mismatch emittance. Both the linear and non-linear misalignment emittance are small. The mismatch in simulation is caused by numerical noise.

	Measurement		Simulation	
	full beam	±FWHM/2	full beam	±FWHM/2
Projected emittance	0.58 µm	0.57 µm	0.53 µm	0.52 µm
Slice emittance	0.50 µm	0.50 µm	0.48 µm	0.49 µm
Mismatch emittance	0.26 µm	0.23 µm	0.23 µm	0.19 µm
Linear misalignment emittance	0.11 µm	0.10 µm	0.01 µm	< 0.01 µm
Non-linear misalign. emittance	0.01 µm	< 0.01 µm	< 0.01 µm	< 0.01 µm

allow a projected emittance decomposition as described in Sec. 2.5. The emittance contributions, both derived from the measurement and simulation, are listed in Table 6.4. The slice emittance measurement determined a projected emittance of $(0.58 \pm 0.01\,(\text{stat.}))$ µm, while the simulation shows a projected emittance of only 0.53 µm. The charge-averaged slice and mismatch emittance are slightly bigger in experiment than in simulation. However, the difference is less than 10 % of the projected emittance. The only bigger difference between both measurement and simulation is given in linear misalignment emittance. In simulation this quasi vanishes, due to the perfect symmetry of the beam and of external electromagnetic fields, as well as the perfect alignment, which makes correction of the beam orbit unnecessary in simulation, while it is needed in experiment. Nevertheless, the contribution from the linear misalignment emittance to the projected emittance is only

$$\frac{\epsilon^2_{\text{linear misalignment}}}{\epsilon^2_{\text{Proj}}} = 3.6\,\%, \tag{6.2.1}$$

i.e. on a similar level as in case of the electron created with a temporal Gaussian laser pulse. This suggest an equally good optimisation of the beam transport by the operators, which is also quite reproducible in terms of beam quality.
Compared to the emittance decomposition of the electron beam emitted from a laser pulse with temporal Gaussian shape, the emittance decomposition of measurement values in the temporal flattop case accord with simulation values for the whole beam, and not only for FWHM values. It agrees with the thesis, that the measured beam properties have a higher uncertainty in the low-intensity tails, due to the lower signal-to-noise ratio, which are reduced for the temporal flattop case. The emittance decomposition is also done for the centre part of the bunch, limited by ±FWHM. The agreement between measurement and simulation is similarly good.

6.3 Transversely Truncated Gaussian and Longitudinal Gaussian Beam Profile

Shaping of the temporal laser pulse profile from Gaussian to a flattop leads to a reduction of slice emittance. However, this puts stringent requirements to the longitudinal laser pulse shaping in terms of long-term stability, which form a challenge at photoinjectors. An alternative is transverse laser pulse shaping, while keeping the longitudinal laser pulse profile Gaussian. A laser pulse, with a transversely Gaussian distribution, which is clipped at a certain level should also lead to an emittance reduction, while relaxing the demands on laser systems by shifting the pulse shaping from the temporal to the transverse plane, which is achieved more easily. An emittance optimisation with such a transversely truncated Gaussian laser pulse profile had been done as well. Figure 6.23 illustrates the transverse pulse profile used for the photoemission of the electron beam. The laser pulse shows a Gaussian distribution which is cut at a radius of 0.5 mm, where the laser intensity dropped to approximately 60 % on its maximal value. As the flattop distributions shown before, the laser profile exhibits a low-intensity halo around the beam. In total, the beam has a beam size of $\sigma_x = 0.228\,\mathrm{mm}$ and $\sigma_y = 0.226\,\mathrm{mm}$ in the horizontal and vertical plane, respectively. The longitudinal pulse profile was not shaped, therefore yielding the standard 6 ps-long Gaussian pulse shape, as plotted in Fig. 6.2.
The optimisation of this electron bunch was done for a bunch charge of 250 pC. The bunch charge versus laser pulse energy for this BSA and truncation level is depicted in Fig. 6.24. The emission curve shows, that the working point chosen is at the beginning of the so-called *transition regime*, where the emitted bunch charge does not depend linearly onto the laser pulse energy. At this working point the minimal emittance is achieved, see Ref. [96]. The gun was operated at on-crest phase, with a cathode gradient of $\sim 57\,\mathrm{MV/m}$. After the gun cavity the electron beam had a momentum of $6.33\,\mathrm{MeV}/c$. The CDS booster cavity was accelerating the electron to a mean momentum of $19.45\,\mathrm{MeV}/c$ at on-crest phase. The horizontal and vertical projected emittance was measured while the solenoid magnet strength was scanned. Figure 6.25 depicts the measured projected emittance in both planes, as well as the horizontal and vertical rms beam size at the slit position. At the solenoid current of 371 A the minimal emittance was achieved. At this solenoid magnet current the beam shows good symmetry between the x and y plane. This is due to the roundness optimisation with the gun quadrupole magnets, which has been performed beforehand. It was optimised at a solenoid current of 373 A at the screen High1.Scr4, which is the beamlet observation screen during the projected emittance measurement. A minimal projected rms emittance of $(0.39 \pm 0.01)\,\mu\mathrm{m}$ and $(0.42 \pm 0.03)\,\mu\mathrm{m}$ were measured in the horizontal and vertical plane, respectively. This projected emittance is already significantly reduced, compared to the emittance measured in case of transverse flattop

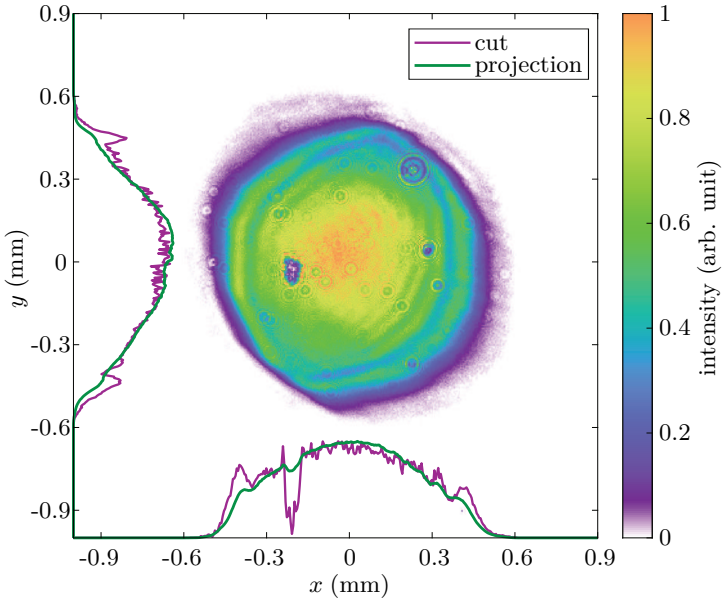

Figure 6.23: Transverse laser distribution of the transversely-truncated Gaussian. The inner part of the profile has a 2d-Gaussian shape, which is clipped at a radius close to 0.5 mm, yielding an overall beam size of $\sigma_x = 0.228\,\text{mm}$ and $\sigma_y = 0.226\,\text{mm}$. The intensity of the laser pulse at the edge where it is clipped is close to 60 %.

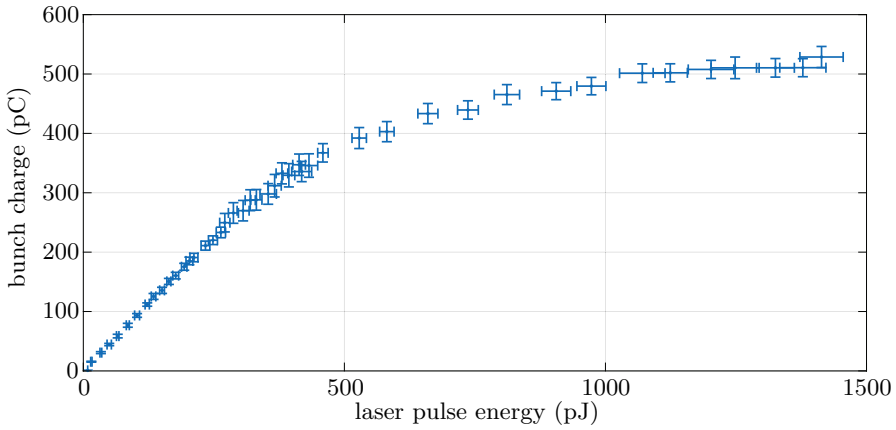

Figure 6.24: Emission curve. The bunch charge growth linearly with the laser pulse energy. With increasing bunch charge space charge forces become dominant, which bend the emission curve, eventually leading to saturation of the bunch charge. The bunch charge in experiment was set to 250 pC. See Ref. [96] for more details.

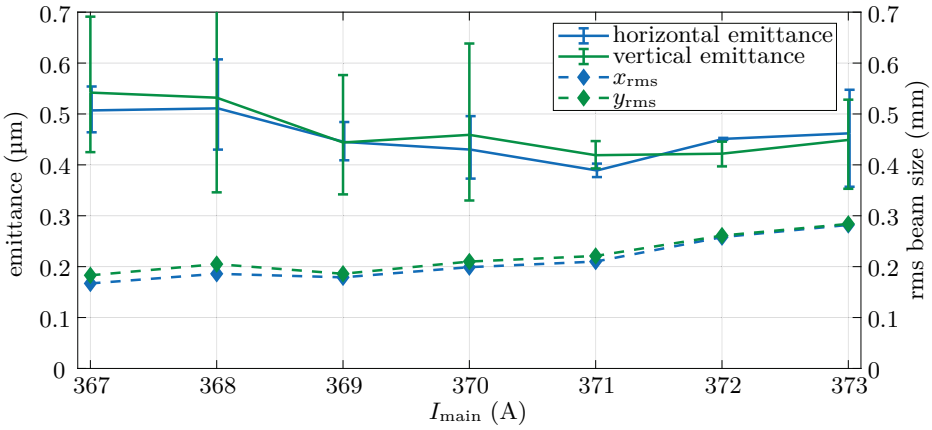

Figure 6.25: Projected rms emittance values and rms beam size in the horizontal and vertical plane at different main solenoid currents I_{main}. The error bars on the emittance values are derived from the scaling factor, as described in Sec. 4.2. The values were taken at a bunch charge of 250 pC, which were emitted from a cathode with a laser pulse with transversely truncated Gaussian shape. The minimal emittance is $\epsilon_{xy} = (0.40 \pm 0.02)$ µm at $I_{\mathrm{main}} = 371$ A.

distributions. The projected, horizontal phase space is shown in Fig. 6.26. The electron beam at the slit position is depicted in Fig. 6.27. The beam size is $\sigma_x = (0.208 \pm 0.001)$ mm and $\sigma_y = (0.205 \pm 0.002)$ mm. These errors are given by the rms uncertainty, derived from ten images, that were taken. Afterwards the optics was prepared for slice emittance measurements. The quadrupole magnets High1.Q09 and High1.Q10 were set to a current of 4.00 A and −4.00 A, at which the quadrupole magnets achieve a strength of 3.21 T/m. This yields the transport matrix elements $R_{11} = 0.35$ and $R_{12} = 3.75$ m in the horizontal plane from the slit station to the observation screen.
The deflected electron beam on the observation screen is given in Fig. 6.28. The electron beam, emitted from a transverse flattop and longitudinal Gaussian shows a big beam size at the centre slices, see Fig. 6.8. The electron beam, created from a temporally flattop-shaped laser pules, shows a rather uniform slice beam size along its longitudinal coordinate. The electron beam from a transversely-truncated Gaussian exhibits a change in beam size along the slices, stronger than the electron beam emitted from a temporal flattop laser pulse, but not as strong as the temporal Gaussian case. The superposition of all beamlets shows a similar trend: The superposition of the beamlets covers a larger screen area than the superposition of beamlets of an electron beam, emitted from a temporally flat laser pulse. Figure 6.29 depicts three of the rf-deflected beamlets. The mid plot shows a beamlet taken, when the slit was cutting out a central part of the beam, while the beamlets on both sides have a position offset of 300 µm.
The slice emittance of this electron beam is given in Fig. 6.30. The electron beam shows a centre slice emittance of $(0.45 \pm 0.05\,(\mathrm{stat.}))$ µm. Between −5 ps and 5 ps the emittance does not change strongly. Further towards the tails the emittance decreases, leading to an emittance of $(0.25^{+0.13}_{-0.09}\,(\mathrm{stat.}))$ µm and $(0.30 \pm 0.06\,(\mathrm{stat.}))$ µm at the tail slices. The blue-dashed line shows the slice emittance of a macro particle bunch, which was generated in ASTRA and tracked to the slit position in EMSY1, i.e. shows the result from a start-to-end simulation. In simulation, an electron bunch length of 6 ps is assumed at the cathode, as the temporal laser shape in experiment was the same as in Sec. 6.1. The transverse laser pulse shape was tweaked to have the same radial charge distribution as the radial laser pulse shape, retrieved from the laser pulse shape shown in Fig. 6.23. Gun cavity and

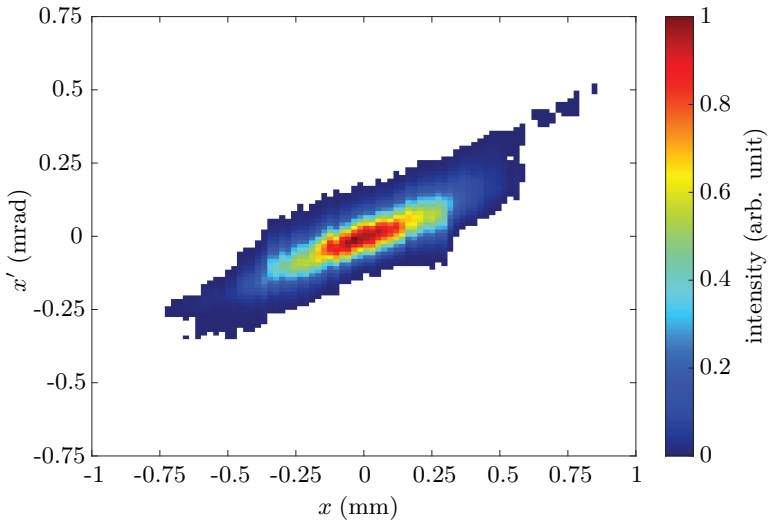

Figure 6.26: Projected, horizontal phase space of the electron beam, emitted from a transversely clipped Gaussian laser pulse shape. The main solenoid current was set to achieve minimal projected emittance, i.e. $I_{\mathrm{main}} = 371\,\mathrm{A}$.

booster cavity were set to on-crest phase in simulation, as they were in experiment. The rf field strength in simulation was set to achieve a beam energy close to the one in experiment. The beam was tracked to the slit station, while assuming different solenoid magnet field strength. The result with the smallest projected emittance is selected. The slice emittance curve is shown in Fig. 6.30 as dashed blue line. The shear parameter was not calibrated in experiment. Therefore the shear parameter assumed in analysis is chosen such that the temporal bunch profile in measurement and simulation match. In the centre the simulated slice emittance is 0.48 µm, i.e. close to the measured value. The simulated emittance curve follows the measured values (within their uncertainty) in the centre, i.e. between −5 ps and 4 ps. Beyond this range the simulation shows peaks in slice emittance, which are not seen in the measurement. This is similar to the case of an electron beam from a temporal Gaussian with a transverse flattop distribution. The simulation showed there peaks in slice emittance as well, which were not seen in measurement, possibly due to low SNR.
The measured and simulated mismatch parameters are shown in red. Here a big deviation is seen: While the measured mismatch parameter is very close to its optimum, i.e. 1 at the centre and rises only to 1.42, it is already much higher in the centre for the simulation curve. The simulation shows a mismatch for most part of the bunch, e.g. 1.35 at the centre. Only at 6.5 ps perfect matching is achieved. Towards the tails of the bunch the mismatch is even larger.
The projected emittance is retrieved from the data when no slicing is applied. A comparison of projected beam properties between the projected emittance measurement tool, i.e. the Fastscan tool, and the SlitScanner tool for slice emittance is listed in Table 6.5. The projected emittance, measured with both tools, shows a big difference: It is 23 % bigger in case of the SlitScanner tool. The horizontal beam size, measured at the slit position shows good agreement. The larger projected phase space width is measured with the Fastscan tool than with the SlitScanner tool, as already in Table 6.3. Subsequently, the calculated Twiss parameters show large discrepancies. The projected phase space, as well as three horizontal slice phase spaces are shown in Fig. 6.31. All slice phase spaces, and consequently the projected phase space, show a dense core. The uncorrelated, angular spread is comparable to the phase spaces shown in Fig. 6.11. The electron beam also has a smaller spatial halo than the electron beam, emitted from a transverse flattop laser pulse

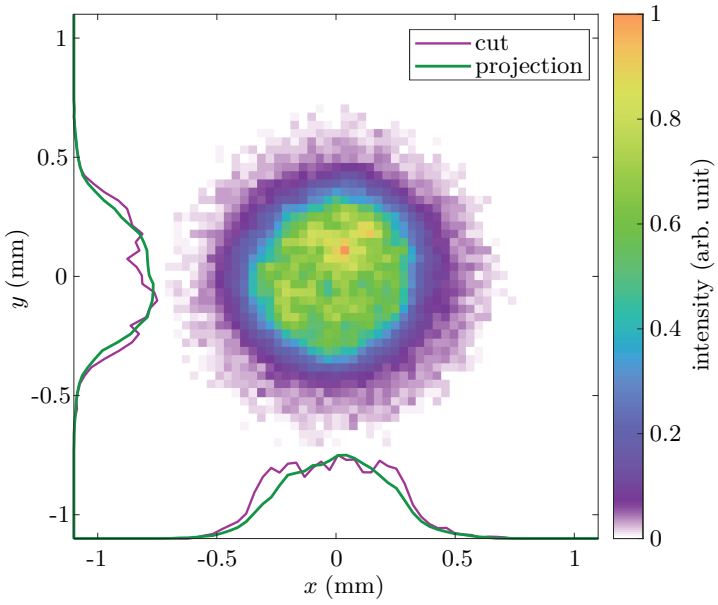

Figure 6.27: Electron beam at the slit position. The beam was emitted from a transversely-truncated laser beam, with a temporal Gaussian pulse shape. The main solenoid magnet was tuned for minimal projected emittance, i.e. 371 A. The beam size is $\sigma_x = (0.208 \pm 0.001)$ mm in the horizontal, and $\sigma_y = (0.205 \pm 0.002)$ mm in the vertical plane, measured before the slice emittance measurement.

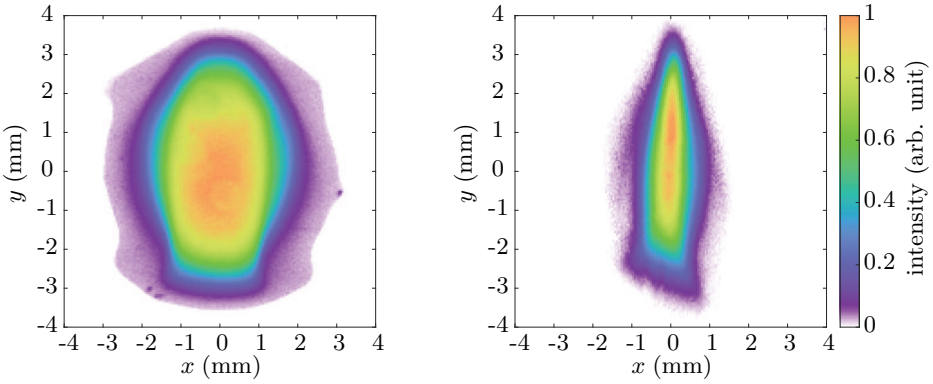

Figure 6.28: Full electron beam at the observation screen PST.Scr1, after deflection with the TDS (left) and superposition of all deflected beamlets on the same screen on the right. The electron beam was emitted from laser pulses with transversely-truncated Gaussian distribution, while the longitudinal pulse shape was Gaussian.

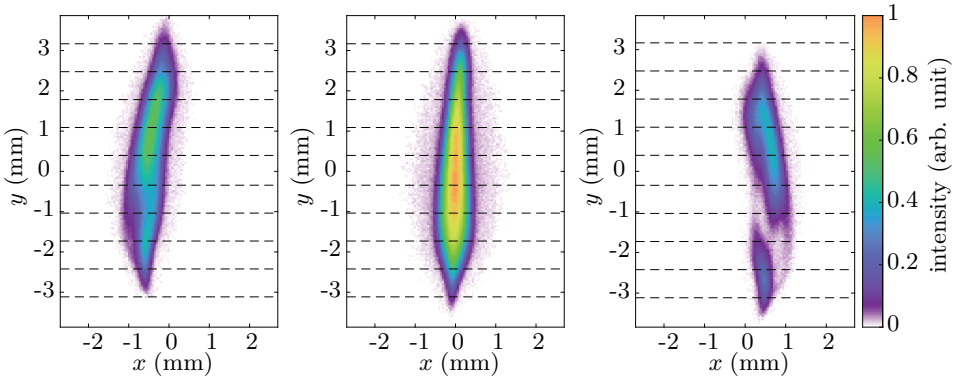

Figure 6.29: Three deflected beamlet images. The electron beam had a bunch charge of 250 pC and was emitted from a transversely-truncated Gaussian laser pulse. The left and right beamlet are taken when the slit was moved by 300 µm off the slit position shown in the centre.

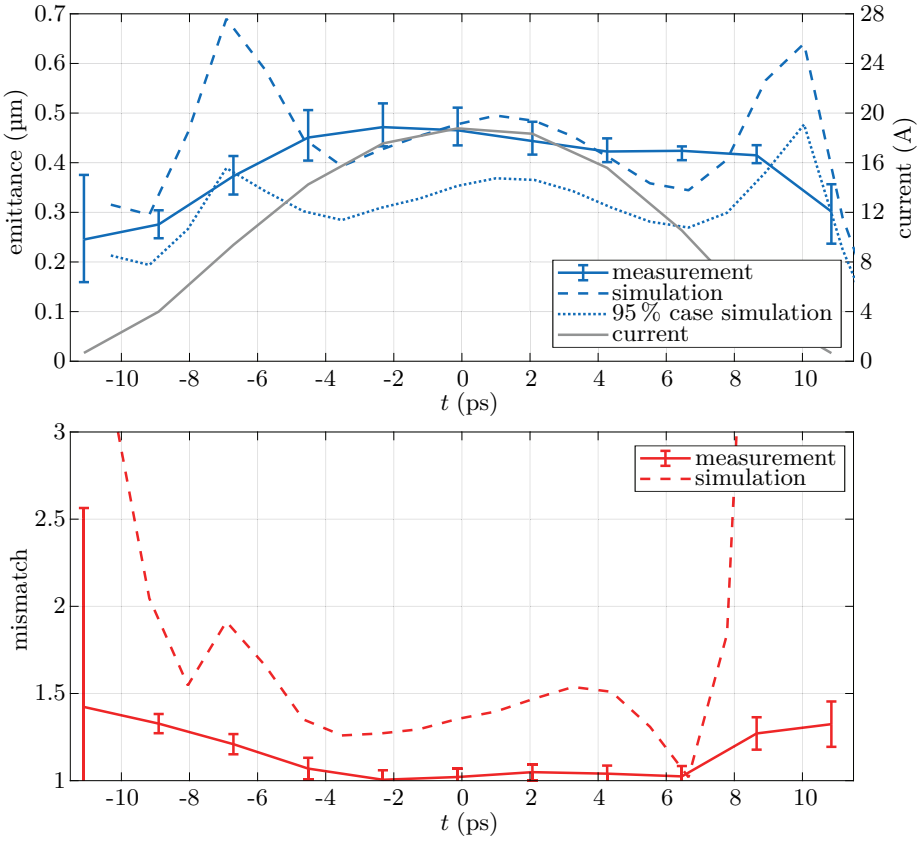

Figure 6.30: Comparison of measured (solid) and simulated (dashed) slice emittance (blue) and mismatch (red) curves of the electron beam, emitted from a laser pulse with a temporal Gaussian shape and transversely-truncated Gaussian shape. Additionally the slice emittance curve from simulation when only considering 95 % of the slice charge is plotted as blue dotted line.

Table 6.5: Comparison of projected, horizontal beam properties measured with the standard projected emittance measurement tool (Fastscan) and the slice emittance measurement scheme (SlitScanner). Both measurements were taken at the slit station EMSY1. The fastscan error in projected emittance is calculated as described in Sec. 4.2. The uncertainties of the properties, measured with SlitScanner are statistical rms errors. For the other values no error is being calculated.

Beam property		unit	Fastscan	SlitScanner
Projected emittance	ϵ_x	µm	0.39 ± 0.01	0.48 ± 0.01
Screen beam size	x_{rms}	mm	0.210	0.208 ± 0.001
Phase space beam size	x_{rms}	mm	0.203	0.188 ± 0.001
Beta function	β_x	m	4.18	2.84 ± 0.05
Alpha function	α_x	-	-1.52	-1.05 ± 0.02

with a temporal Gaussian pulse envelope, as shown in Fig. 6.11. The dense core however has the same width in the spatial domain it spans the range $-0.35\,\mathrm{mm}$ to $+0.35\,\mathrm{mm}$. The decomposition of rms beam moments is listed in Table 6.6. The largest contribution to the projected rms emittance in experiment is given by the slice emittance. It accounts for

$$\frac{\epsilon^2_{\mathrm{slice}}}{\epsilon^2_{\mathrm{Proj}}} = 80\,\% \tag{6.3.1}$$

of the projected emittance. This is similar to the case of the transverse flattop, temporal Gaussian beam, where this fraction was 81 %, see Eq. 6.1.2. In simulation the biggest contribution is given by the mismatch emittance, which contributes by 64 %. The linear and non-linear misalignment emittance determined in simulation is caused by numerical noise, as no symmetry-breaking elements which can cause any misalignment are included in simulation. For a better comparison the rms phase space ellipses are depicted in Fig. 6.32 together with the slice phase space ellipse centroid positions. The slice phase space ellipses in the centre show similarity with each other. At the tails however, the shape is different, and a considerable position offset is observed as well. The charge content of the tail slices is low on the other hand, leading only to a small contribution to the projected emittance. The decomposition of the projected emittance into the temporal emittance contributions for the measurement data and the simulation is listed in Table 6.6. Measurements and simulations show large discrepancies: The projected emittance simulated in ASTRA in 50 % higher than the experimentally measured projected emittance (with the SlitScanner tool). The large projected emittance seen in simulation is caused my a large mismatch between different slices. The simulated mismatch emittance gives the largest contribution to the projected emittance. In the previously shown simulations the projected emittance was dominated by the slice emittance instead. Linear and non-linear misalignment emittance yield values, which are typical (when comparing with Table 6.2 and Table 6.4): The measured linear misalignment emittance is in the order of $\sim 0.12\,\mu\mathrm{m}$, while the simulated linear misalignment emittance and the non-linear misalignment emittance in experiment and simulation vanish.
Table 6.6 also list the charge-weighted emittance contributions, while only the temporal bunch centre in the range between ±FWHM is considered for the calculation. Here the discrepancy is reduced compared to the full beam case, however still remains large. The charge-weighted slice emittance agree in measurement and simulation, while the mismatch emittance differ strongly. It is much larger in simulation in experiment. Overall, this leads in simulation to a projected emittance, which is larger than the measured emittance.

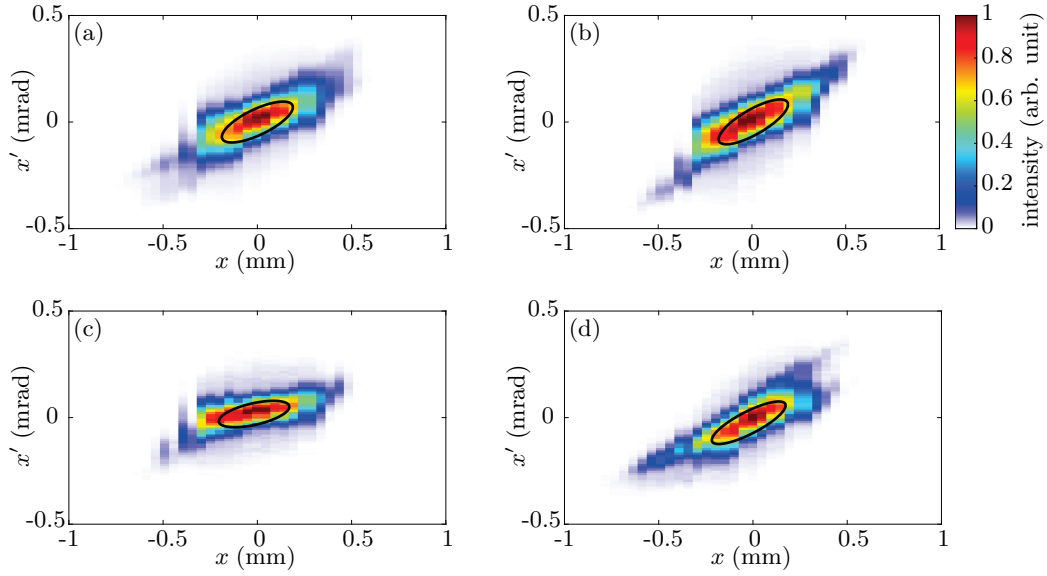

Figure 6.31: Horizontal phase spaces of the electron beam, emitted from a laser pulse with transversely-truncated Gaussian shape and temporally Gaussian shape. The top-left image (a) shows the projected phase space, while the other three sub-figures show slice phase spaces. Image (b) shows the centre slice phase space, located at $t = -0.2\,\mathrm{ps}$, while the phase spaces (c) located at $t = -6.7\,\mathrm{ps}$ and (d) at $t = 6.5\,\mathrm{ps}$ in the bottom row depict phase spaces which are closer to the tails. The rms phase space ellipse is always given in black.

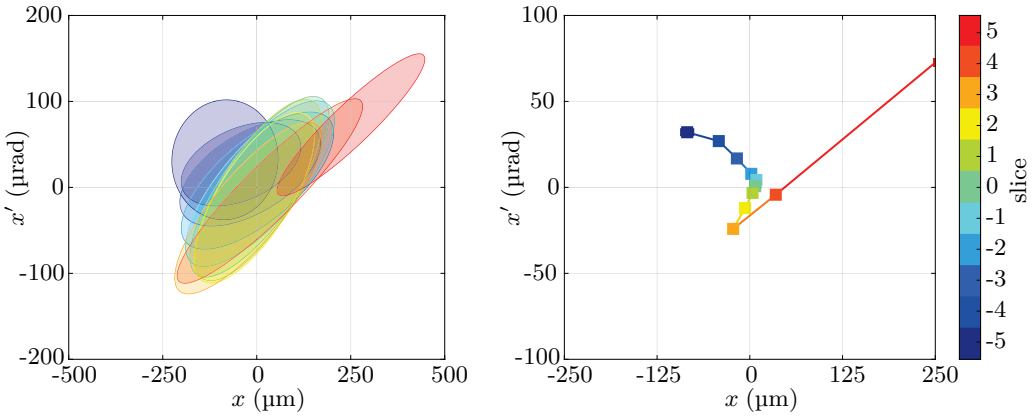

Figure 6.32: Ellipses of the rms phase space (left) and slice phase space centroid positions. The bunch charge of 250 pC was emitted from the cathode with a laser pulse with transversely-truncated Gaussian shape and temporally Gaussian shape.

Table 6.6: Decomposition of the measured and simulated projected rms emittance into slice emittance, mismatch emittance, linear misalignment and non-linear misalignment emittance. The beam had a bunch charge of 250 pC and was emitted using a laser pulse with a temporal Gaussian envelope and a transversely-truncated Gaussian pulse shape. Numerical noise in simulation causes the misalignment emittance in simulation to not be exactly zero.

	Measurement		Simulation	
	full beam	±FWHM/2	full beam	±FWHM/2
Projected emittance	0.48 µm	0.47 µm	0.74 µm	0.60 µm
Slice emittance	0.43 µm	0.45 µm	0.45 µm	0.45 µm
Mismatch emittance	0.16 µm	0.13 µm	0.59 µm	0.40 µm
Linear misalignment emittance	0.12 µm	0.06 µm	0.03 µm	0.01 µm
Non-linear misalign. emittance	0.01 µm	< 0.01 µm	< 0.01 µm	< 0.01 µm

6.4 Comparison of Projected Emittance Contributions

Table 6.7 displays the decomposition of the projected rms emittance of the three experimentally characterised electron bunches, emitted using laser pulses with different pulse shaping. The laser pulse shapes applied have been

- the transverse flattop laser pulse with a temporal Gaussian profile,
- the transverse and temporal flattop laser pulse profile and
- the transversely-truncated Gaussian laser pulse shape with a temporal Gaussian pulse envelope.

For the characterisation the laser pulse energy was set to emit a bunch charge of 250 pC, as this is the typical bunch charge used at Eu-XFEL. Table 6.7 shows, that the slice emittance and mismatch emittance can be reduced by means of pulse shaping. When starting from a temporal Gaussian and transverse flattop laser pulse the emittance can be reduced by shaping the temporal pulse shape to a flattop. As a result of the slice and mismatch emittance reduction due to reduced non-linearities in space charge force the projected rms emittance reduces by $\sim 16\,\%$. The slice emittance and mismatch emittance are further reduced, when the transverse pulse shape is changed to a transversely-truncated Gaussian while keeping a temporal Gaussian pulse shape. This leads to a reduction of the projected rms emittance to 0.48 µm, which is 30 % smaller than the projected rms emittance of the electron beam with a transverse flattop shape after emission.
Linear and non-linear misalignment of slice centroids can also contribute to the projected rms emittance. This however is not improved by laser pulse shaping, but by alignment of laser pulse on cathode and electron bunch trajectory, so that the electron bunch travels centred through electro-magnetic fields. The decompositions shows, that the linear and non-linear misalignment emittance is similar for all laser pulse shape, indicating that the alignment is done reproducibly well for every experiment and the arising emittance is not increasing the projected emittance significantly.
The measurements were also simulated in ASTRA achieving mixed agreement between measurement and simulation results. For the case of the temporal Gaussian bunch profile with a transversely truncated-Gaussian simulation and experimental results are not in compliance. Due to the temporal Gaussian bunch profile only low signal-to-noise ration is achieved in the head and tail of the bunch, which makes this areas prone to measurement

Table 6.7: Comparison of the measured emittance decompositions for the three characterised electron beams. The highest emittance was measured for the beam created with a temporal Gaussian, transverse flattop laser pulse. The emittance reduces, when a temporal flattop laser pulse shape is used and reduces even further, when a transversely-truncated Gaussian distribution is chosen. Both the slice emittance and mismatch emittance reduce, which the misalignment emittance stays the same.

Temporal profile Transverse profile	Gaussian Flattop	Flattop Flattop	Gaussian truncated Gaussian
Projected emittance	0.69 µm	0.58 µm	0.48 µm
Slice emittance	0.62 µm	0.50 µm	0.43 µm
Mismatch emittance	0.28 µm	0.26 µm	0.16 µm
Linear misalignment emittance	0.14 µm	0.11 µm	0.12 µm
Non-linear misalignment emittance	0.01 µm	0.01 µm	0.01 µm

error. Comparison of the beam properties in the longitudinal core reduces differences between simulation and experiment.
A much better agreement is achieved for the case of the electron beam, emitted from the temporal Gaussian laser pulse with transverse flattop profile. Here the charge-weighted properties agree, when only the core is considered. Almost perfect agreement between simulation and measurements of the temporal flattop electron bunch is achieved on the whole range for the charge-weighted slice emittance and mismatch emittance. The slice emittance and mismatch curve agree well, as shown in Fig. 6.20.

7 Conclusions.

Synchrotron radiation facilities and free-electron lasers (FELs) are contemporary tools for the analysis of matter. Achieving high brilliance of the emitted radiation requires a high electron density in the phase space. Low transverse slice emittance is one of the keys to achieve high brightness in a LINAC-driven high-gain X-ray FEL. According to the Liouville theorem, the electron source emittance defines the lower limit of the final linear accelerator brightness, therefore injector optimisation is critical for X-ray FEL light sources. The Photoinjector Test facility at DESY in Zeuthen (PITZ) develops and conditions electron gun cavities for their use at the FELs FLASH and Europen XFEL in Hamburg.
Before this thesis, only the projected beam emittance was measured and optimised experimentally at PITZ, and a routine to measure the slice emittance of a space-charge-dominated beam with high resolution was not available. In this thesis, a scheme to measure the slice emittance with subpicosecond time resolution was developed by adding a transverse deflecting cavity (TDS) to the single-slit scan, which is utilised for projected emittance measurements. This allows characterisation of space-charge-dominated electron beams with high brightness with energies around 20 MeV and beam currents around 50 A. The slit scan technique suffers from low signal-to-noise ratio (SNR), and this was compensated by the long bunch train at PITZ for projected emittance measurements, but the TDS rf pulse length is limited to deflect three electron bunches in a train. Moreover, the TDS inflicts vertical deflection onto the beam, which lowers the horizontal beamlet charge density and therefore the SNR. Lastly, the distance between the slit station and the beamlet observation screen is much larger for slice emittance measurements. While for the projected emittance measurement setup the distance could be optimised more freely, the TDS location constrained the choice of measurement screen during slice emittance measurements. The first screen behind the TDS is used as observation screen. The long distance additionally makes it difficult to achieve a small vertical beta function on the observation screen, which worsens the temporal resolution. Therefore, special attention was put to deal with these issues. A slit with a wider opening is used for slice emittance measurements. While projected emittance is measured with a 10 µm-wide slit, the slice emittance is measured with a 50 µm slit. Scintillator screens made from LYSO are used at the screen stations for slice emittance measurements which have a higher light yield than the standard YAG screens. Furthermore, the optical system for the observation of beamlets was improved by moving the camera closer to the screen which increases the detected light and therefore the SNR improved. Moreover, quadrupole doublet magnets after the slit were exploited to reduce the beamlet size on the observation screen. A smaller vertical focus allows achieving the required time resolution with a reduced vertical streaking and therefore better SNR. A properly reduced transport matrix element R_{12} from the slit mask to the measurement screen leads to a higher charge density and SNR, without losing the angular resolution. In this procedure, the transport matrix for reconstructing the transverse phase space is not a pure drift, but involving two quadrupole magnets. To avoid large systematic errors in transport matrix calculation due to the magnetic magnet model and hysteresis, a beam-based trajectory response measurement is used to measure R_{12} online, and a thin-lens model is used to extract R_{11} from R_{12}, which ensures a reliable phase space reconstruction.
The screen station for the observation of the beamlets might be further improved in the future to increase the sensitivity of the total detection system, and thus, the reliability

of the slice emittance measurement scheme. Alternative types of scintillator screens are being tested with electron beams at PITZ to improve the efficiency without losing spatial resolution or response linearity. This will help to pick the best screen material for a reliable measurement of beam size. Additionally an EMCCD camera is also available at PITZ, which can be considered to further reduce the noise level. Due to its high price and risk from radiation damage, it was not yet used in the studies.
Sources of systematic error were analysed in detail by simulation of the diagnostics scheme using ASTRA [41]. Here the influence from the residual space charge forces in each beamlet were analysed, the influence from different slit width, drift length, focusing strength, and TDS deflection strength were investigated. Additionally, slice emittance measurements with different beam optics and TDS deflection strength were done. Furthermore, the systematic error arising from emittance underestimation due to the finite SNR was analysed by applying intensity cuts to the electron beam obtained from start-to-end simulations with PITZ-typical beam properties and accelerator working point. The simulations show, that for SNRs of ~ 50, which are typical for slice emittance measurements at PITZ, the centre slice emittance is measured with only 4 % systematic error.
The slice emittance diagnostic were used to study effects of spatial and temporal laser pulse shaping on the time-resolved phase space of the European XFEL 250 pC working point [91]. The characterisation shows that flattop temporal pulse shaping leads to an reduction of the transverse emittance. While a central slice emittance of $(0.69\,^{+0.05}_{-0.03}\,(\text{stat.}))$ µm is measured for an electron beam emitted from a laser pulse with temporal Gaussian shape, a centre slice emittance of $(0.50 \pm 0.01\ (\text{stat.}))$ µm is achieved for when using laser pulses with temporal flattop shape. An even larger reduction is achieved when employing transverse pulse shaping, to create a laser pulse with a transversely-truncated Gaussian profile, compared to a transverse flattop laser pulse. With a transversely truncated Gaussian laser pulse a centre slice emittance of $(0.47\,^{+0.05}_{-0.03}\,(\text{stat.}))$ µm is achieved.
The experiments of laser shaping effects on slice emittance are also benchmarked by simulations in ASTRA. A good agreement between measurement and simulation is observed at the centre slices, and a larger discrepancy is seen at the head and tail slices, which might be caused by the reduced SNR. For the transverse and temporal flattop case a good agreement is seen on a large range. For FEL application the slice emittance in the core must be low for good performance. Here, the transversely-truncated Gaussian beam shows the lowest emittance.
Based on the time-resolved transverse phase space measurements the projected rms emittance decomposition according to Ref. [48] is presented. This allows analysis of the projected emittance growth sources which is a powerful electron beam diagnostics for operators of linear accelerators.

A PITZ Lattice

Table A.1 contains the most important elements of the PITZ beamline and their positions.

Table A.1: Overview over the main elements in the PITZ beamline. The emittance measurement system (EMSY) stations are also equipped with screens.

Section	Name	Element	Position (m)
Gun		Photo cathode surface	0.000
Boost	Boost.IGP2	Booster centre	3.588
High1	High1.Q01	Quadrupole magnet	4.790
	High1.St1	Horizontal corrector magnet	4.895
	High1.Q02	Quadrupole magnet	5.005
	EMSY1	Emittance measurement system (slit station)	5.277
	High1.StA1	Vertical corrector magnet	5.427
	High1.Q03	Quadrupole magnet	5.603
	High1.Q04	Quadrupole magnet	5.853
	High1.Scr2	Screen station	6.250
	High1.Q05	Quadrupole magnet	6.648
	High1.Q06	Quadrupole magnet	6.893
	High1.St2	Horizontal corrector magnet	7.040
	EMSY2	Emittance measurement system (slit station)	7.125
	High1.StA2	Vertical corrector magnet	7.298
	High1.St3	Horizontal corrector magnet	8.128
	High1.Q07	Quadrupole magnet	8.180
	High1.Scr4	Screen station	8.410
	High1.Q08	Quadrupole magnet	8.655
	High1.Scr5	Screen station	8.920
	High1.St4	Horizontal corrector magnet	9.823
	High1.Q09	Quadrupole magnet	10.208
	High1.Q10	Quadrupole magnet	10.388
RFD	TDS	TDS centre	10.985
PST	PST.St1	Rotating corrector magnet	11.600
	PST.QM1	Quadrupole magnet	12.088
	PST.Scr1	Screen station	12.278
	PST.St2	Rotating corrector magnet	12.390
	PST.QM2	Quadrupole magnet	12.468
	PST.QM3	Quadrupole magnet	12.848
	PST.Scr2	Screen station	13.038
	PST.St3	Rotating corrector magnet	13.150
	PST.QT1	Quadrupole magnet	13.228
	PST.QT2	Quadrupole magnet	13.608
	PST.Scr3	Screen station	13.798

Continued on next page

Section	Name	Element	Position (m)
PST	PST.St4	Rotating corrector magnet	13.910
	PST.QT3	Quadrupole magnet	13.988
	PST.QT4	Quadrupole magnet	14.368
	PST.Scr4	Screen station	14.558
	PST.St5	Rotating corrector magnet	14.670
	PST.QT5	Quadrupole magnet	14.748
	PST.St6	Rotating corrector magnet	14.981
	PST.QT6	Quadrupole magnet	15.128
	PST.Scr5	Screen station	15.318
High2	EMSY3	Emittance measurement system (slit station)	16.303
	High2.St1		16.453
	High2.Q1	Quadrupole magnet	16.635
	High2.Q2	Quadrupole magnet	16.735
	High2.St2		16.832
	Disp3.D1	Dipole magnet	17.614
	High2.Scr2	Screen station	18.262
Disp3		end of beamline arc Disp3.D1	0.000
	Disp3.Scr1		0.699
	Disp3.D2		2.226
		end of beamline arc Disp3.D2	0.000
	Disp3.Q1		0.330
	Disp3.Scr2		1.382
	Dump	Beam dump	21.943

Bibliography

[1] F. R. Elder et al., *Radiation from Electrons in a Synchrotron*, Phys. Rev. **71**, 829, 10.1103/PhysRev.71.829.5, (1947).

[2] K. Wille, *The Physics of Particle Accelerators*, Oxford University Press (2000).

[3] U. Bergmann et al., *Science and Technology of Future Light Sources: A White Paper*, (2008).

[4] J. Feikes et al., *Sub-picosecond Electron Bunches in the BESSY Storage Ring*, Proc. of the European Particle Accelerator Conference, Lucerne, Switzerland, https://accelconf.web.cern.ch/e04/PAPERS/WEPLT051.PDF, (2004).

[5] A. A. Zholents and M. S. Zolotorev, *Femtosecond X-Ray Pulses of Synchrotron Radiation*, Phys. Rev. Lett. **76**, 912, 10.1103/PhysRevLett.76.912, (1996).

[6] J. Feikes, P. Kuske and G. Wüstfeld, *Towards sub-picosecond Electron Bunches: Upgrading Ideas for BESSY II*, Proc. of the European Particle Accelerator Conference, Edinburgh, Scotland, http://accelconf.web.cern.ch/e06/PAPERS/MOPCH053.PDF, (2006).

[7] A. Zholents et al., *Generation of subpicosecond X-ray pulses using RF orbit deflection*, NIM A **425**, 1, 10.1016/S0168-9002(98)01372-2, (1999).

[8] S. Pandey et al., *Time-resolved serial femtosecond crystallography at the European XFEL*, Nat. Methods **17**, 10.1038/s41592-019-0628-z, (2020).

[9] P. Vagovic et al., *Megahertz x-ray microscopy at x-ray free-electron laser and synchrotron sources*, Optica **6**, 9, 10.1364/OPTICA.6.001106, (2019).

[10] N. Berrah et al., *Femtosecond-resolved observation of the fragmentation of buckminsterfullerene following X-ray multiphoton ionization*, Nat. Physics **15**, 10.1038/s41567-019-0665-7, (2019).

[11] E. T. Karamatskos et al., *Molecular movie of ultrafast coherent rotational dynamics of OCS*, Nature Commun. **10**, 10.1038/s41467-019-11122-y, (2019).

[12] Z.-H. Loh et al., *Observation of the fastest chemical processes in the radiolysis of water*, Science **367**, 6474, 10.1126/science.aaz4740, (2020).

[13] J. M. J. Madey, *Stimulated Emission of Bremsstrahlung in a Periodic Magnetic Field*, Journal of Applied Physics **42**, 1906, 10.1063/1.1660466, (1971).

[14] D. A. G. Deacon et al., *First Operation of a Free-Electron Laser*, Phys. Rev. Lett. **38**, 892, 10.1103/PhysRevLett.38.892, (1977).

[15] J. Andruszkow et al., *First Observation of Self-Amplified Spontaneous Emission in a Free-Electron Laser at 109 nm Wavelength*, Phys. Rev. Lett. **85**, 3825, 10.1103/PhysRevLett.85.3825, (2000).

[16] P. Emma et al., *First lasing and operation of an ångstrom-wavelength free-electron laser*, Nature Photonics **4**, 10.1038/nphoton.2010.176, (2010).

[17] H. Weise and W. Decking, *Commissioning and First Lasing of the European XFEL*, Proc. of the International Free Electron Laser Conference, Santa Fe, NM, USA, 10.18429/JACoW-FEL2017-MOC03, (2017).

[18] European X-FEL Website, https://www.xfel.eu/facility/overview/facts_amp_figures/index_eng.html, 26.11.2019.

[19] P. Schmüser et al., *Free-Electron Lasers in the Ultraviolet and X-Ray Regime*, Springer International Publishing, (2014).

[20] L. Serafini and J. B. Rosenzweig, *Envelope analysis of intense relativistic quasilaminar beams in rf photoinjectors: A theory of emittance compensation*, Phys. Rev. E **55**, 6, 10.1103/PhysRevE.55.7565, (1997).

[21] Z. Huang and K.-J. Kim, *Review of x-ray free-electron laser theory*, Phys. Rev. ST Accel. Beams **10**, 034801, 10.1103/PhysRevSTAB.10.034801, (2007).

[22] F. Stephan et al., *Photo Injector Test Facility under Construction at DESY Zeuthen*, Proc. of the International Free Electron Laser Conference, Durham, USA, (2000).

[23] V. Miltchev, *Investigations on the transverse phase space at a photo injector for minimized emittance*, Ph.D. thesis, Humboldt-Universität zu Berlin, 10.3204/DESY-THESIS-2006-025, (2006).

[24] M. Hänel, *Experimental Investigations on the Influence of the Photocathode Laser Pulse Parameters on the Electron Bunch Quality in an RF - Photoelectron Source*, Ph.D. thesis, Universität Hamburg, 10.3204/DESY-THESIS-2010-027, (2010).

[25] M. Krasilnikov et al., *Experimentally minimized beam emittance from an L-band photoinjector*, Phys. Rev. ST Accel. Beams **15**, 100701, 10.1103/PhysRevSTAB.15.100701, (2012).

[26] L. Staykov, *Characterization of the transverse phase space at the photo-injector test facility in DESY, Zeuthen*, Universität Hamburg, Dissertation, https://bib-pubdb1.desy.de/record/85111, (2008).

[27] G. Asova, *Tomography of the Electron Beam Transverse Phase Space at PITZ*, Ph.D. thesis, Bulgarian Academy of Sciences - Institute for Nuclear Research and Nuclear Energy, Sofia, 10.3204/DESY-THESIS-2013-040, (2012).

[28] G. Vashchenko, *Transverse phase space studies with the new CDS booster cavity at PITZ*, Ph.D. thesis, Universität Hamburg, 10.3204/DESY-THESIS-2013-043, (2013).

[29] G. Kourkafas, *Incorporating space charge in the transverse phase-space matching and tomography at PITZ*, Ph.D. thesis, Universität Hamburg, 10.3204/DESY-THESIS-2015-044, (2015).

[30] H. Huck et al., *Progress on the PITZ TDS*, Proc. of the International Beam Instrumentation Conference, Barcelona, Spain, 10.18429/JACoW-IBIC2016-WEPG47, (2016).

[31] C. Vaccarezza et al., *Slice Emittance Measurements at SPARC Photoinjector with a RF Deflector*, Proc. of the European Particle Accelerator Conference, Genoa, Italy, http://accelconf.web.cern.ch/e08/papers/tupc105.pdf, (2008).

[32] M. Röhrs et al., *Time-resolved electron beam phase space tomography at a soft x-ray free-electron laser*, Phys. Rev. ST Accel. Beams **12**, 050704, 10.1103/PhysRevSTAB.12.050704, (2009).

[33] G. Penco et al., *Time-Sliced Emittance and Energy Spread Measurements at FERMI@ELETTRA*, Proc. of the International Free Electron Laser Conference, Nara, Japan, https://accelconf.web.cern.ch/FEL2012/papers/wepd20.pdf, (2012).

[34] M. Yan et al., *Comparison of Quadrupole Scan and Multi-Screen Method for the Measurement of Projected and Slice Emittance at the SwissFEL Injector Test Facility*, Proc. of the International Free Electron Laser Conference, Basel, Switzerland, https://bib-pubdb1.desy.de/record/171803, (2014).

[35] J. H. Lee et al., *Slice Emittance Measurement using RF Deflecting Cavity at PAL-XFEL ITF*, Proc. of the International Free Electron Laser Conference, Basel, Switzerland, https://epaper.kek.jp/FEL2014/papers/thp013.pdf, (2014).

[36] J. Wychowaniak, C. Gerth and M. Yan, *Design of TDS-based Multi-Screen Electron Beam Diagnostics for the European XFEL*, Proc. of the International Free Electron Laser Conference, Basel, Switzerland, https://accelconf.web.cern.ch/FEL2014/papers/thp075.pdf, (2014).

[37] M. Yan, *Online diagnostics of time-resolved electron beam properties with femtosecond resolution for X-ray FELs*, Ph.D. thesis, Universität Hamburg, https://bib-pubdb1.desy.de/record/300658, (2015).

[38] Y. Ivanisenko, *Investigation of Slice Emittance Using an Energy-chirped Electron Beam in a Dispersive Section for Photo Injector Characterization at PITZ*, Ph.D. thesis, Universität Hamburg, https://bib-pubdb1.desy.de/record/96101, (2012).

[39] H. Huck et al., *First Results of Commissioning of the PITZ Transverse Deflecting Structure*, Proc. of International Free Electron Laser Conference, Daejeon, Korea, 10.18429/JACoW-FEL2015-MOP039, (2015).

[40] D. Malyutin, *Time resolved transverse and longitudinal phase space measurements at the high brightness photo injector PITZ*, Ph.D. thesis, Universität Hamburg, 10.3204/DESY-THESIS-2014-021, (2014).

[41] ASTRA Website, http://www.desy.de/~mpyflo/, 27.11.2019.

[42] H. Wiedemann, *Particle Accelerator Physics*, Springer (2015).

[43] K. Floettmann, *Some basic features of the beam emittance*, Phys. Rev. ST Accel. Beams **6**, 034202, 10.1103/PhysRevSTAB.6.034202, (2003).

[44] M. Ferrario, M. Migliorati and L. Palumbo, *Space Charge Effects*, contribution to the CAS - CERN Accelerator School: Advanced Accelerator Physics Course, Trondheim, Norway, 10.5170/CERN-2014-009.331, (2013).

[45] A. Ferran Pousa, *Novel Concepts and Theoretical Studies for High-Quality Plasma-Based Accelerators*, Ph.D. thesis, Universität Hamburg, 10.3204/PUBDB-2020-04106, (2020).

[46] K. Floettmann, *Emittance compensation in split photoinjectors*, Phys. Rev. Accel. Beams **20**, 013401, 10.1103/PhysRevAccelBeams.20.013401, (2017).

[47] J. B. Rosenzweig, S. Anderson and L. Serafini, *Space charge dominated envelope dynamics of asymmetric beams in RF photoinjectors*, Proc. of the Particle Accelerator Conference **2**, 10.1109/PAC.1997.751076, (1997).

[48] C. Mitchell, *A General Slice Moment Decomposition of RMS Beam Emittance*, https://arxiv.org/abs/1509.04765, (2015).

[49] J. D. Good, *Experimental Characterization of the Photocathode Laser System for Advanced 3D Pulse Shaping at PITZ*, Ph.D. thesis, Universität Hamburg, 10.3204/PUBDB-2020-02829, (2020).

[50] A. Cianchi, *High brightness electron beam emittance evolution measurements in an rf photoinjector*, Phys. Rev. ST Accel. Beams **11**, 032801, 10.1103/PhysRevSTAB.11.032801, (2008).

[51] G. Z. Georgiev and M. Krasilnikov, *Virtual Pepper-Pot Technique for 4D Phase Space Measurements*, Proc. of the International Beam Instrumentation Conference, Malmö, Sweden, 10.18429/JACoW-IBIC2019-WEPP029, (2019).

[52] F. Löhl et al., *Measurements of the transverse emittance at the FLASH injector at DESY*, Phys. Rev. ST Accel. Beams **9**, 092802, 10.1103/PhysRevSTAB.9.092802, (2006).

[53] E. Prat and M. Aiba, *Four-dimensional transverse beam matrix measurement using the multiple-quadrupole scan technique*, Phys. Rev. ST Accel. Beams **17**, 052801, 10.1103/PhysRevSTAB.17.052801, (2014).

[54] C. Koschitzki et al., *Status of Chirped Pulse Laser Shaping for the PITZ Photoinjector*, Proc. of the Free Electron Laser Conference, Hamburg, Germany, 10.18429/JACoW-FEL2019-WEP050, (2019).

[55] Y. L. Chen, M. Krasilnikov and F. Stephan, *The Cooling Effect of Beam Self-Fields on the Photocathode Surface in High Gradient RF Injectors*, Proc. of International Particle Accelerator Conference, Melbourne (Australia), 10.1088/1742-6596/1350/1/012121, (2019).

[56] G. Shu et al., *Multiphysics Analysis of a CW VHF Gun for European XFEL*, Proc. of the Free Electron Laser Conference, Hamburg, Germany, 10.18429/JACoW-FEL2019-WEP055, (2019).

[57] M. Gross et al., *Observation of the Self-Modulation Instability via Time-Resolved Measurements*, Phys. Rev. Lett. **120**, 144802, 10.1103/PhysRevLett.120.144802, (2018).

[58] G. Loisch et al., *Observation of High Transformer Ratio Plasma Wakefield Acceleration*, Phys. Rev. Lett. **121**, 064801, 10.1103/PhysRevLett.121.064801, (2018).

[59] H. Qian et al., *Investigation of High Repetition Rate Femtosecond Electron Diffraction at PITZ*, Proc. of the International Particle Accelerator Conference, Copenhagen, Denmark, 10.18429/JACoW-IPAC2017-THPAB017, (2017).

[60] P. Boonpornprasert, *Investigations on the Capabilities of THz Production at the PITZ Facility*, Dissertation, Universität Hamburg, 10.3204/PUBDB-2020-00563, (2020).

[61] PITZ Website, http://pitz.desy.de/research_and_development/pitz_beamline/, 21.01.2018.

[62] I. Will, G. Koss and I. Templin, *The upgraded photocathode laser of the TESLA Test Facility*, NIM A **541**, 3, 10.1016/j.nima.2004.12.007, (2005).

[63] I. Will and G. Klemz, *Generation of flat-top picosecond pulses by coherent pulse stacking in a multicrystal birefringent filter*, Opt. Express **16**, 19, 10.1364/OE.16.014922, (2008).

[64] J. Bähr et al., *Upgrades of the Laser Beam-Line at PITZ*, Proc. of the International Free Electron Laser Conference, Stanford, USA, http://accelconf.web.cern.ch/f05/PAPERS/MOPP034.PDF, (2005).

[65] M. Gross et al., *Emittance Reduction of RF Photoinjector Generated Electron Beams by Transverse Laser Beam Shaping*, Journal of Physics: Conference Series, **1350**, 012046, 10.1088/1742-6596/1350/1/012046, (2019).

[66] F. Stephan et al., *Detailed characterization of electron sources yielding first demonstration of European X-ray Free-Electron Laser beam quality*, Phys. Rev. ST Accel. Beams **13** 020704, 10.1103/PhysRevSTAB.13.020704, (2010).

[67] Website JAI, https://www.jai.com/, 06.05.2021.

[68] Website Light Conversion, https://lightcon.com/product/pharos-femtosecond-lasers/, 30.07.2021.

[69] S. Y. Mironov et al., *Shaping of cylindrical and 3D ellipsoidal beams for electron photoinjector laser drivers*, Appl. Opt. **55**, 7, 10.1364/AO.55.001630, (2016).

[70] G. Loisch, *Demonstrating High Transformer Ratio Beam-Driven Plasma Wakefield Acceleration*, Dissertation, Universität Hamburg, 10.3204/PUBDB-2019-03713, (2019).

[71] I. Isaev, *Stability and Performance Studies of the PITZ Photoelectron Gun*, Dissertation, Universität Hamburg, 10.3204/PUBDB-2018-01119, (2018).

[72] V. Paramonov et al., *Design Parameters of the Normal Conducting Booster Cavity for the PITZ-2 Test Stand*, Proc. of the Linear Accelerator Conference, Lübeck, Germany, https://accelconf.web.cern.ch/l04/PAPERS/MOP77.PDF, (2004).

[73] V. Paramonov et al., *The PITZ CDS Booster Cavity RF Tuning and Start of Conditioning*, Proc. of the Linear Accelerator Conference, Tsukuba, Japan, https://accelconf.web.cern.ch/LINAC2010/papers/mop081.pdf, (2010).

[74] Danfysik Website, https://www.danfysik.com/, 15.04.2020.

[75] V. Miltchev, *Construction and commissioning of a Transverse Emittance Measurement System for the Photoinjector Test facility at DESY Zeuthen*, master thesis, Humboldt-Universität zu Berlin, (2002).

[76] B. Walasek-Höhne et al., *Screens for high precision measurements*, Proc. of the International Beam Instrumentation Conference, Malmö, Sweden, 10.18429/JACOW-IBIC2019-TUBO01, (2019).

[77] R. Niemczyk et al., *Comparison of YAG Screens and LYSO Screens at PITZ*, Proc. of the International Beam Instrumentation Conference, Shanghai, China, 10.18429/JACoW-IBIC2018-WEPB04, (2018).

[78] Website Crytur, https://www.crytur.cz/, 15.04.2020.

[79] Website Omega Piezo Technologies, http://www.omegapiezo.com/crystal-scintillators/, 15.04.2020.

[80] Website Allied Vision, https://www.alliedvision.com/en/products/cameras.html, 15.04.2020.

[81] O. H. Altenmueller, R. R. Larsen and G. A. Loew, *Investigations of Traveling-Wave Separators for the Stanford Two-Mile Linear Accelerator*, Review of Scientific Instruments **35**, 438, 10.1063/1.1718840, (1964).

[82] P. Emma, J. Frisch and P. Krejcik, *A Transverse RF Deflecting Structure for-Bunch Length and Phase Space Diagnostics*, LCLS-TN-00-12, Stanford, USA, https://www-ssrl.slac.stanford.edu/lcls/technotes/lcls-tn-00-12.pdf, (2000).

[83] M. Cornacchia and P. Emma, *Transverse to longitudinal emittance exchange*, Phys. Rev. ST Accel. Beams **5**, 084001, 10.1103/PhysRevSTAB.5.084001, (2002).

[84] K. Hosoyama et al., *Development of the KEK-B Superconducting Crab Cavity*, Proc. of the European Particle Accelerator Conference, https://accelconf.web.cern.ch/e08/papers/thxm02.pdf, (2008).

[85] B. Hall et al., *Design and testing of a four rod crab cavity for High Luminosity LHC*, Phys. Rev. Accel. Beams **20**, 012001, 10.1103/PhysRevAccelBeams.20.012001, (2017).

[86] L. Kravchuk et al., *Layout of the PITZ Transverse Deflecting System for Longitudinal Phase Space and Slice Emittance Measurements*, Proc. of the International Linear Accelerator Conference, Tsukuba, Japan, https://bib-pubdb1.desy.de/record/91526, (2010).

[87] W. K. H. Panofsky and W. A. Wenzel, *Some Considerations Concerning the Transverse Deflection of Charged Particles in Radio-Frequency Fields*, Review of Scientific Instruments **27**, 11, 10.1063/1.1715427, (1956).

[88] K. Floettmann and V. V. Paramonov, *Beam dynamics in transverse deflecting rf structures*, Phys. Rev. ST Accel. Beams **17**, 024001, 10.1103/PhysRevSTAB.17.024001, (2014).

[89] S. G. Anderson et al., *Space-charge effects in high brightness electron beam emittance measurements*, Phys. Rev. ST Accel. Beams **5**, 014201, 10.1103/PhysRevSTAB.5.014201, (2002).

[90] H. Huck, private communication, (2015).

[91] D. Nölle, *Commissioning of the European XFEL*, Proc. of the Linear Accelerator Conference, Beijing, China, 10.18429/JACoW-LINAC2018-FR2A02, (2018).

[92] *An Introduction To Error Propagation*, http://srl.informatik.uni-freiburg.de/papers/arrasTR98.pdf, 28.02.2019.

[93] W. Decking et al., *A MHz-Repetition-Rate Hard X-Ray Free-Electron Laser Driven by a Superconducting Linear Accelerator*, Nature photonics **14**, 6, 10.1038/s41566-020-0607-z (2020).

[94] M. Krasilnikov et al., *Beam-Based Procedures for RF Guns*, Proc. of the Particle Accelerator Conference, Knoxville, Tennessee, https://accelconf.web.cern.ch/p05/PAPERS/WPAP005.PDF, (2005).

[95] M. Krasilnikov et al., *Investigations on Electron Beam Imperfections at PITZ*, Proc. of the Linear Accelerator Conference, East Lansing, MI, USA, 10.18429/JACoW-LINAC2016-MOPLR013, (2016).

[96] Y. Chen et al., *Budgeting the emittance of photoemitted electron beams in a space-charge affected emission regime for free-electron laser applications*, AIP Advances **10**, 035017, 10.1063/1.5129532, (2020).

Acknowledgements

I would like to take the opportunity to thank all the people I had the pleasure to work with during the course of this thesis.

First of all I want to thank my supervisor, Houjun, for his stamina during the many long discussions we had. I particularly appreciated his many good ideas, and am grateful for his close supervision, which allowed me to analyse scientific questions in great depth.

To write a good thesis, a student needs support for extensive interactions with the broader scientific community. I am grateful that my group leader, Frank, was most generous in sending me to many conferences and schools. More importantly, he always had an open ear for my ideas, which I was always encouraged to give in discussions.

Also I want to thank my professor, Wolfgang, for the many honest exchanges that we had. He made sure that the project is both feasible and on track, while also reminding me to be relaxed while doing my research. It was always a pleasure to talk to him.

I want to thank my subgroup leader Mikhail for the many beam dynamics discussions we had. His vast knowledge of accelerator science, and his openness to debate, proved to be of great help during my time at PITZ.

I also want to thank group members Matthias and Anne, for tirelessly working to create and maintain a smooth accelerator environment. I also want to thank them for being the calm anchors during arguments in group meetings at PITZ.

When I began my thesis at PITZ, the preliminary work of my former colleague Holger proved to be an invaluable starting point for my PhD research. I am eternally grateful for his input in my early days at PITZ.

PITZ is not the only accelerator at DESY, and discussions about bunch profile and slice emittance measurements at Eu-XFEL and FLASH helped me to fit my research into the broader DESY-wide picture. I am happy that I could discuss this topic with many knowledgeable people, including Hamburg colleagues Bolko, Matthias, Pau and Florian.

Laser pulse shaping became a key component of my dissertation. Of course there could be no laser pulse shaping without a working laser, and for this reason I am indebted to Matthias, James and Christian for maintaining and developing the lasers which made the measurements possible. I know this wasn't the easiest task in the world!

For providing wisdom and assistance in coding, I would like to thank Osip, James and Grygorii. Their guidance improved the speed and quality of my coding immeasurably.

Increasing the reliability of the slice emittance measurement procedure required a software to perform trajectory response measurements. Luckily I never had to write this code myself, because Osip already wrote excellent software. I want to thank him for all the time this saved me in my research.

When working on shift at PITZ, I often needed the support from technical groups at PITZ. Without fail, this support was always forthcoming in a respectful and friendly manner. I found them to be patient, eminently reasonable and felt we developed a relationship based on trust. Working together was always enjoyable.

During my research I enjoyed working with my colleagues in the PITZ group. I want to thank those colleagues I am glad to also call friends, and especially thank Osip, Gregor, Namra and Tobias for casual discussion on many topics, both in and outside the field of accelerator science.

Beyond the PITZ group members I am grateful for the broader community at DESY Zeuthen, and the warm atmosphere they create. This begins with friendly exchanges with the door guards at the Campus entrance (or even on the S Bahn platform/train to Zeuthen), spans all of the people I would see on Campus, all the way up to friendly chats with Director Christian Stegmann. I enjoyed my time in Zeuthen immensely, and was happy to also find several friends among DESYaners in other groups with whom I shared conversations, beers and many adventures! I find myself unable to acknowledge each of them in the way they deserved, but want to highlight Robert and Xavier in particular, who have been most excellent friends of mine during this time.

Finally I also want to thank my family, especially my mother Aurelia and my brother Lukas, but also my aunt Asia and everyone else. Though they were often physically distant, they always remained emotionally close to me. I often found a place to escape from research for a few days. I am very happy to have you all!

Raffael Niemczyk

Eidesstattliche Versicherung/Declaration on oath

Hiermit versichere ich an Eides statt, die vorliegende Dissertationsschrift selbst verfasst und keine anderen als die angegebenen Hilfsmittel und Quellen benutzt zu haben.

Die eingereichte schriftliche Fassung entspricht der auf dem elektronischen Speichermedium.

Die Dissertation wurde in der vorgelegten oder einer ähnlichen Form nicht schon einmal in einem früheren Promotionsverfahren angenommen oder als ungenügend beurteilt.

Hamburg, den 04. August 2021

Raffael Niemczyk